ANALYSIS AND COMPENSATION OF IMPERFECTION EFFECTS IN PIEZOELECTRIC VIBRATORY GYROSCOPES

by

Philip Wayne Loveday

Dissertation submitted to the Faculty of the
Virginia Polytechnic Institute and State University
in partial fulfillment of the requirements for the degree of

DOCTOR OF PHILOSOPHY
in
Mechanical Engineering

APPROVED:

_____

Dr C. A. Rogers, Chairman

_____ _____

Dr D. J. Inman Dr M. Ahmadian

_____ _____

Dr H. H. Robertshaw Dr D. J. Leo

February 1999
Blacksburg, Virginia
Keywords: gyroscope, vibratory, piezoelectric, control, imperfections

Analysis And Compensation Of Imperfection Effects In Piezoelectric Vibratory Gyroscopes

Philip Wayne Loveday

(ABSTRACT)

Vibratory gyroscopes are inertial sensors, used to measure rotation rates in a number of applications. The performance of these sensors is limited by imperfections that occur during manufacture of the resonators. The effects of resonator imperfections, in piezoelectric vibratory gyroscopes, were studied.

Hamilton's principle and the Rayleigh-Ritz method provided an effective approach for modeling the coupled electromechanical dynamics of piezoelectric resonators. This method produced accurate results when applied to an imperfect piezoelectric vibrating cylinder gyroscope. The effects of elastic boundary conditions, on the dynamics of rotating thin-walled cylinders, were analyzed by an exact solution of the Flügge shell theory equations of motion. A range of stiffnesses in which the cylinder dynamics was sensitive to boundary stiffness variations was established. The support structure, of a cylinder used in a vibratory gyroscope, should be designed to have stiffness outside of this range. Variations in the piezoelectric material properties were investigated. A figure-of-merit was proposed which could be used to select an existing piezoceramic material or to optimize a new composition for use in vibratory gyroscopes.

The effects of displacement and velocity feedback on the resonator dynamics were analyzed. It was shown that displacement feedback could be used to eliminate the natural frequency errors, that occur during manufacture, of a typical piezoelectric vibrating cylinder gyroscope. The problem of designing the control system to reduce the effects of resonator imperfections was investigated. Averaged equations of motion, for a general resonator, were presented. These equations provided useful insight into the dynamics of the imperfect resonator and were used to motivate the control system functions. Two

control schemes were investigated numerically and experimentally. It was shown that it is possible to completely suppress the first-order effects of resonator mass/stiffness imperfections. Damping imperfections, are not compensated by the control system and are believed to be the major source of residual error. Experiments performed on a piezoelectric vibrating cylinder gyroscope showed an order of magnitude improvement, in the zero-rate offset variation over a temperature range of 60°C, when the control systems were implemented.

ACKNOWLEDGMENTS

I wish to thank the members of my advisory committee for the interest they showed in this research. In particular, the guidance provided by Dr Craig A. Rogers greatly enhanced this learning experience. I appreciate his continued involvement even after his departure from Virginia Tech. I am grateful to Dr Daniel J. Inman and Beth Howell for making the arrangements for my dissertation defense.

I acknowledge the financial support provided by the CSIR, South Africa which made it possible for me to study in the USA. The support of my collegues at Sensor Systems was greatly appreciated. In particular I must thank Dr Michail Y. Shatalov for the many stimulating technical discussions and Dr Frederik A. Koch for his informal mentorship and encouragement during my Ph.D. studies.

I thank my parents for their support during my undergraduate studies and for always encouraging me to study further. Finally, I would like to thank Dalene for her patience and understanding during the past four years. I appreciate your love and the sacrifices you have made so that I could undertake this step in my education.

TABLE OF CONTENTS

NOMENCLATURE

Chapters 2,4 and 6

$\mathbf{B}_f$	Generalized coordinate conversion matrix for forces.
$\mathbf{B}_q$	Generalized coordinate conversion matrix for charges at electrodes.
$\mathbf{c}^E$	Piezoceramic elasticity matrix at constant electrical field.
$\mathbf{C}_P$	Piezoceramic capacitance matrix.
D	Electrical displacement vector (charge/area).
e	Matrix of piezoelectric constants (stress/electrical field).
E	Electrical field vector (volts/meter).
f	Vector of applied forces.
f_{max}	Frequency of maximum admittance.
f_{min}	Frequency of minimum admittance.
F(x), H(x)	Cantilever beam functions.
G	Gyroscopic matrix.
$\mathbf{G_d}$	Matrix of displacement feedback gains.
$\mathbf{G_v}$	Matrix of velocity feedback gains.
h	Wall thickness of cylinder.
h_c	Thickness of piezoceramic elements.
k_{eff}	Effective electromechanical coupling coefficient.
$\mathbf{K}_S$, $\mathbf{K}_P$	Structure and piezoceramic stiffness matrices.
$\mathbf{L}_u$	Elastic differential operator.
$\mathbf{L}_\varphi$	Electrical differential operator.
$\mathbf{M}_S$, $\mathbf{M}_P$	Structure and piezoceramic mass matrices.
N	Matrix of differentiated distribution functions.
q	Vector of charges applied at the electrodes.
r(t)	Vector of mechanical generalized coordinates.

$\mathbf{R}_E$	Electrical field rotation matrix.
$\mathbf{R}_S$	Strain rotation matrix.
S	Strain vector.
T	Kinetic energy.
T	Stress vector.
u(x)	Vector of mechanical displacements.
u, v, w	Displacements in the axial, tangential and radial directions.
U	Strain energy.
v(t)	Vector of electrical generalized coordinates.
V_S, V_P	Volume of structure and piezoceramic.
W	Work function.
W_e	Electrical energy.
W_m	Magnetic energy.
$\boldsymbol{\Theta}$	Electromechanical coupling matrix.
ρ_S,ρ_P	Structure and piezoceramic densities.
φ(x)	Scalar electrical potential.
$\boldsymbol{\varepsilon}^S$	Matrix of dielectric constants at constant strain.

Chapter 3

a	Mean radius of cylinder.
A_1 , ... , A_8	Amplitude ratios defined in Appendix B.
C_1 , ... , C_8	Displacement coefficients.
E	Young's modulus.
h	Cylinder wall thickness.
$k_u^0,\ k_v^0,\ k_w^0,\ k_{w'}^0$	Axial, tangential, radial and rotational boundary stiffnesses at x=0.
$k_u^L,\ k_v^L,\ k_w^L,\ k_{w'}^L$	Axial, tangential, radial and rotational boundary stiffnesses at x=L.

$k_u^*,\ k_v^*,\ k_w^*,\ k_{w'}^*$	Nondimensionalised axial, tangential, radial and rotational boundary stiffnesses.
L	Cylinder length.
m	Axial mode number.
n	Number of circumferential waves.
S	Potential energy of the cylinder and boundaries.
t	Time.
T	Kinetic energy of the cylinder.
u, v, w	Components of displacement in the axial, tangential and radial directions.
$U_0,\ V_0,\ W_0$	Axial, tangential and radial displacement amplitudes.
x, φ	Axial and angular coordinates.
α	Axial wave number.
β	Dimensionless parameter, $\beta = h^2/12a^2$.
Δ	Frequency factor, $\Delta = \omega a\sqrt{\rho(1-\nu^2)/E}$.
ν	Poisson's ratio.
ρ	Mass density .
ω	Circular frequency.
Ω	Rate of angular rotation of cylinder.

Chapter 5

k	Bryan factor.
n	Number of circumferential waves.
ν	Operating frequency.
x	Displacement of the $\cos(2\theta)$ vibrating pattern.
y	Displacement of the $\sin(2\theta)$ vibrating pattern.
f_x	Force applied to the $\cos(2\theta)$ vibrating pattern.
f_y	Force applied to the $\sin(2\theta)$ vibrating pattern.

Ω	Applied angular rotation rate.
ω_1	First natural frequency.
ω_2	Second natural frequency.
$\omega^2 = \frac{\omega_1^2 + \omega_2^2}{2}$	Mean natural frequency squared.
$\omega\Delta\omega = \frac{\omega_1^2 - \omega_2^2}{2}$	Measure of difference in natural frequencies.
θ_ω	Angle to the first natural mode.
τ_1 , τ_2	Two principle time constants.
$\frac{1}{\tau} = \frac{1}{2}(\frac{1}{\tau_1} + \frac{1}{\tau_2})$	Mean damping factor.
$\Delta(\frac{1}{\tau}) = \frac{1}{2}(\frac{1}{\tau_1} - \frac{1}{\tau_2})$	Difference in damping factors.
θ_τ	Angle to the first principal damping axis.

LIST OF TABLES

LIST OF FIGURES

Chapter One

Introduction

Vibratory gyroscopes are inertial instruments used to measure angular rotation rate. Similar to conventional spinning-mass gyroscopes, these modern gyroscopes are based on the Coriolis effect, which arises in a rotating frame of reference. The major difference between the two types is that instead of the spinning wheel used in a conventional gyroscope the momentum of a vibrating elastic body is used in a vibratory gyroscope. The solid-state nature of vibratory gyroscopes makes various unique features possible. Because there are no motors or bearings, these sensors can be designed to be extremely rugged and have effectively infinite service life without the need for maintenance. Other advantages include very short start-up times (less than one second), low power consumption, small size and low cost.

Although one company has produced an inertial grade vibratory gyroscope, which competes with the most advanced ring laser gyroscopes [1], applications requiring lower performance have generally been targeted by vibratory gyroscope developers. Early efforts were motivated by military applications. These included missile guidance and stabilization, gun, camera and antenna stabilization, smart munitions including gun-fired munitions and GPS augmented navigation. More recently, potential markets in the automotive and consumer-goods industries have attracted significant efforts for purely commercial applications. Commercial applications which have already used vibratory gyroscopes include automobile navigation and ride stabilization, hand-held video camera stabilization and underwater vehicle stabilization and navigation. As the technology develops and vibratory gyroscopes become smaller, cheaper and perform better, many more applications will become possible.

1.1 Principles of Operation of Vibratory Gyroscopes

In this section the operation of an ideal vibratory gyroscope, operating in the rate

mode is described. The effects of imperfections are introduced in section 1.3.

In vibratory gyroscopes an elastic body, or resonator, is forced to vibrate in a flexible mode. When the resonator is rotated about the sensitive axis, the vibration pattern changes and this change is used as a measure of the applied rotation rate. More specifically, the resonator is excited to resonate in a particular mode of vibration. When a rotation rate is applied, Coriolis forces couple energy from the primary mode of vibration into a secondary mode. This transfer of energy provides a measure of the applied rotation rate.

Resonators of various geometries have been presented in the literature. These geometries are described in section 1.2. Broadly speaking, the resonators may be divided into two classes depending on the modes of vibration that are used during operation as a gyroscope. In the first class of resonators the Coriolis coupling between two dissimilar vibration modes of different natural frequency, is measured. The resonators forming the second class have two orthogonal vibration modes which have the same shape and identical natural frequencies, in the absence of imperfections.

The vibrating cylinder gyroscope, which is treated extensively in this dissertation, falls into the second class. In this class the bandwidth of the gyroscope is related to the time it takes for the secondary mode to reach steady-state conditions after a step input rotation rate. This time is dependent on the damping of the secondary mode which is usually low, resulting in a gyroscope with a low bandwidth of typically 5 to 10 Hz. To increase the bandwidth, to a more useful 40 to 50 Hz, it is necessary to actively control the secondary mode of vibration. Fig. 1.1 shows the modes used in the vibrating cylinder gyroscope and the control functions required to operate the resonator as a gyroscope. The primary mode ($\cos 2\theta$) has antinodes at 0°, 90°, 180° and 270° therefore these locations are chosen for the attachment of sensing and actuation piezoceramic elements. The secondary mode ($\sin 2\theta$) has the same form as the primary mode, but is rotated by 45° with respect to the primary mode. The secondary mode has antinodes at 45°, 135°, 225° and 315° at which piezoceramic elements are attached. The opposite piezoceramics are electrically connected in pairs. The primary mode control excites the primary mode at 90° (and 270°) and senses the response signal at 0° (and 180°). The function of the

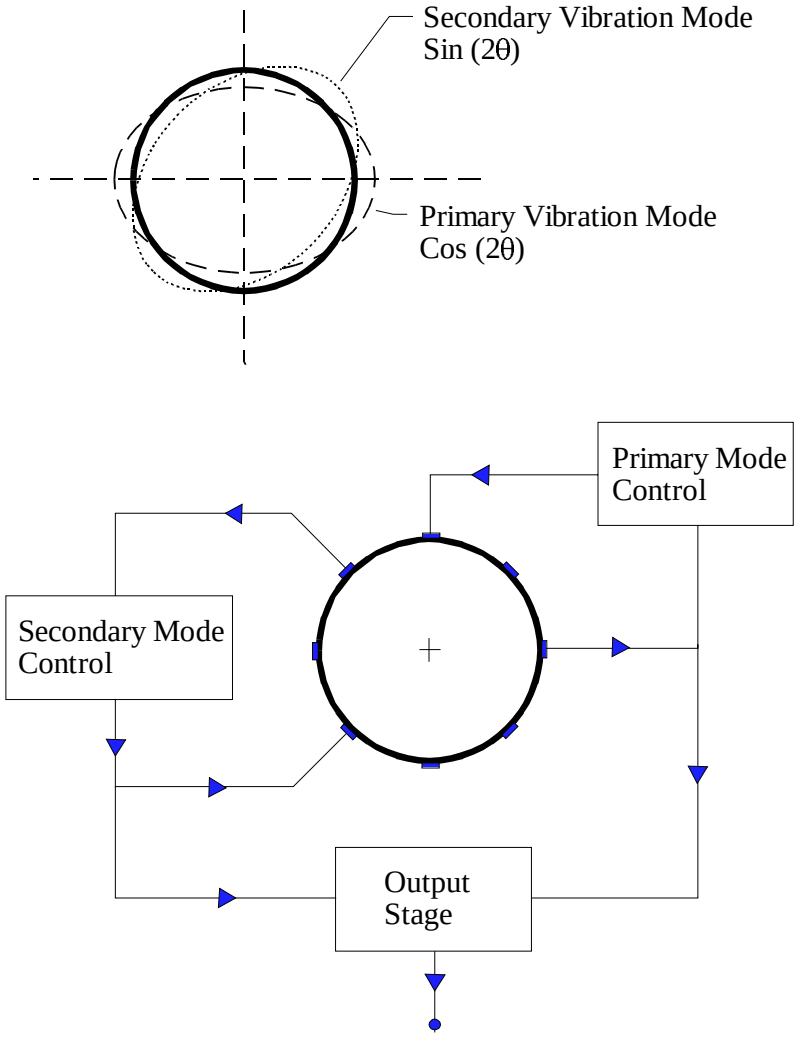

Figure 1.1 Natural mode shapes and control system functions used in an ideal vibrating cylinder gyroscope.

primary mode control is to excite the resonator at resonance and to produce a constant amplitude of vibration. The secondary mode control is used to increase the bandwidth of the gyroscope. Some designs which do not use secondary mode control have been developed for applications requiring small bandwidths. The output stage demodulates the signal in the secondary mode control loop and produces a dc signal proportional to the applied rotation rate.

Various transduction methods have been applied to excite and sense the resonator vibrations. These methods include electromagnetism, electrostatics and piezoelectricity. Only piezoelectric actuation and sensing is considered in this dissertation.

As a vibratory gyroscope incorporates sensing and actuation linked by control functions, it may be regarded as a "smart sensor". It is not surprising therefore, that much of the knowledge applied in the field of "smart material systems and structures" should also be relevant in this research and vice versa.

1.2 Review of Vibratory Gyroscope Designs

The following review is intended to introduce the reader to the major developments in the field of vibratory gyroscopes. The designs which have had a major impact on the field, in the author's opinion, are briefly described. This review is not intended to be an exhaustive account of all the published literature but focuses rather on practical developments. The designs are reviewed in order of increasing geometric complexity rather than in historical order.

In 1851, Foucault demonstrated that a pendulum could be used to measure the rotation of the earth [2]. Foucault's pendulum was essentially the first example of a vibratory gyroscope and for this reason it is often cited in the vibratory gyroscope literature.

Quick [3] presented an analysis of a vibrating string angular motion sensor. The string was fixed at one end and was excited in the first lateral mode by parametric excitation applied along the string axis. As in the Foucault pendulum, this design was a rotation angle sensor rather than an angular rate sensor. Stability conditions were derived and the effects of important imperfections, elastic and damping asymmetry, were analyzed.

Unfortunately no actual device details or experimental results were presented.

Two very low-cost designs based on vibrating beams have been produced in Japan. Murata's "Gyrostar" is based on a steel beam with triangular cross-section which is actuated and sensed by attached piezoceramic elements [4]. The Tokin design uses a piezoceramic cylindrical beam [5]. In both designs the beams vibrate in the first flexural mode of a free-free beam and are supported at the nodes. These devices do not use feedback control of the secondary mode.

Designs based on pendulums, vibrating strings or cantilever beams are sensitive to linear accelerations. A simple balanced resonator can be formed by using a tuning-fork in which the tines are forced to vibrate equally but in opposite directions. An early tuning-fork design was described by Hunt and Hobbs [6]. In this design the Coriolis forces caused a torsional oscillation of the stem of the tuning-fork, which was measured to indicate the applied rotation rate. Feedback control of the torsional oscillation was used to improve the response time of the gyroscope. Their design was large and expensive to manufacture, but it did produce a zero-rate offset stability of better than 1 degree/h albeit at constant temperature.

A micromachined tuning-fork gyroscope was successfully produced by Systron Donner. The "Gyrochip" uses a single-crystal piezoelectric quartz resonator that incorporates a torsion stem with a tuning-fork at each end. One tuning fork is excited so that the tines vibrate towards and away from each other. When an angular rotation rate is applied about the axis parallel to the tines, Coriolis forces produce a torsional moment in the stem. The second tuning-fork responds to this twisting of the stem and the out-of-plane deflection of the tines provides a measure of the rotation rate. The two modes of vibration used in this design have different natural frequencies and no feedback control of the secondary mode is used. A micromachined design which uses only one tuning-fork without a torsion stem was investigated by Söderkvist [7].

The effect of rotation on the vibration of thin-walled cylinders or bells was first analyzed by Bryan in 1890 [8]. Researchers at General Motors Corporation made use of this effect when they started development of a gyroscope based on a thin-walled hemispherical resonator in the 1960's [9,10]. The hemispherical resonator gyroscope

(HRG), comprises a fused-quartz hemispherical resonator which is actuated and sensed electrostatically. A series of patents have been filed describing a number of improvements on the original idea. The original patents covered operation as an angular rate sensor. Later patents by Loper and Lynch [11,12] described the operation as a rate integrating sensor. In this mode the vibrating pattern is allowed to precess freely around the circumference of the resonator. This "whole angle operation" had the unique advantage that the device would continue to integrate the applied rotation during short electrical power interruptions that could follow nuclear explosions. More recently, changing between operation as a rate integrating sensor and operation as a rate sensor during a mission has been described [13]. Devices based on resonators with Q-factors of 10^7 have achieved inertial grade performance and compete with modern ring laser gyroscopes. The HRG is clearly the most technologically advanced and impressive vibratory gyroscope developed. Unfortunately, apart from the patents, there is not a great deal of in-depth technical information available. This is probably due to the requirements of military secrecy. Some of the main features of the HRG design are described by Loper and Lynch [14].

It appears that much of the knowledge developed during the development of the HRG was not applied by other researchers developing low cost designs because these designs were rate sensors while the whole angle operation of the HRG was described in the literature. The HRG proved that high performance is attainable with vibratory gyroscopes. It appears that much of this technology will find application in commercial markets through the development of a micromachined ring gyroscope being developed by Delco [15]. This design makes use of many of the ideas developed for the HRG but because it is micromachined it is small and can be mass produced at low cost.

Another device which stems from the work of Bryan is the vibrating cylinder gyroscope. A design which used a steel thin-walled cylinder, closed at one end, with discrete piezoceramic actuation and sensing elements was developed by Marconi (later GEC-Marconi Avionics) [16]. Initially this design was aimed at military applications in missiles and smart munitions. The ruggedness of the sensor was proven in shock tests up to 25,000 g. The unique features of vibratory gyroscopes opened the way for commercial

applications and this gyroscope was used in the active suspension system of the Formula 1 Team Lotus racing cars during 1987. Today this gyroscope is used as the yaw rate sensor in the "Vehicle Dynamics Control System" manufactured by Robert Bosch GmbH and is in mass production [17].

Instead of attaching piezoceramic elements to a steel cylinder it is possible to make the cylinder from piezoceramic material. The feasibility of such a device was analyzed by Burdess [18]. British Aerospace (Systems & Equipment) Limited (BASE) developed and produced the Vibrating Structure Gyroscope (VSG) based on such a resonator [19]. BASE has developed two newer designs based on rings. The first uses a steel ring and electromagnetic excitation and capacitive sensing while the second uses a micromachined ring with electromagnetic sensing and actuation.

Today the potential of micromachining technology is being applied in the development of low cost designs by various universities and companies [20]. Strong interest in micromachined designs is reflected by the number of presentations on these designs at the recent Stuttgart and St. Petersburg conferences. A number of the companies that were producing macromachined vibratory gyroscopes have started developing or producing micromachined designs. Delco, who produced the HRG are now developing the micromachined vibrating ring gyroscope [21]. Bosch who are producing a vibrating cylinder gyroscope are currently developing a micromachined design based on two oscillating masses [22]. BASE, who have produced piezoceramic cylinder vibratory gyroscopes and a steel ring vibratory gyroscope are now producing a micromachined ring design. Murata have graduated from the macromachined beam to a micromachined mass supported by four thin beams using electrostatic actuation and capacitive sensing [23]. Draper Labs have done extensive development of a $1mm^2$ micromachined tuning fork design which has two perforated masses (tines) which vibrate in the plane. Coriolis forces cause an out-of-plane rocking motion which is sensed capacitively [24]. Researchers at Berkley have demonstrated single and two axis micromachined designs. The two axis design is based on a disk forced to oscillate rotationally about its axis. When rotations are applied in the plane of the disk, Coriolis forces cause the disk to tilt. This provides a measure of the two components of applied rotation [25,26]. These devices have been

integrated with micromachined accelerometers to demonstrate very small inertial measurement units [20].

1.3 Effects of Imperfections

The operation of vibratory gyroscopes as described earlier, did not consider the effects of imperfections. Imperfections, which are always present during the manufacture of vibratory gyroscope resonators, limit the performance of vibratory gyroscopes. Manufacturing imperfections cause departures from the ideal mass, stiffness and damping distributions and therefore effect the resonator dynamics. The effects of imperfections on the resonator dynamics are readily observable. Especially in resonators designed to have identical natural frequencies. These resonators show splitting of natural frequencies, location of the two mode shapes and different damping factors associated with each mode. A method of characterizing the resonator was described by Shatalov et al. [27].

After the manufacture of a resonator, it is common practice to test it and then to mechanically balance the structure to reduce the effects of imperfections. This balancing procedure generally involves the removal or addition of mass, aiming to minimize the splitting of natural frequencies and to align the natural modes with the sensor and actuator positions. This balancing procedure is time consuming, and is usually performed at only one constant temperature. The resonators also often operate in a vacuum but are balanced at atmospheric pressure. The changes that occur in the dynamics of the resonator due to temperature changes and aging with time, make it pointless to balance the structure to extreme accuracies. It is therefore more desirable to design the resonator and control system to be as insensitive as possible to variations in the properties of the resonator.

The effects of imperfections when the resonator is operated as an angle sensor have been investigated by various researchers. In this mode of operation the vibrating pattern is allowed to precess and the angle of precession provides a measure of the angle of applied rotation. Because of damping in the resonator, it is necessary to supply energy to sustain the vibration amplitude without affecting the position of the vibration pattern. These studies will be briefly reviewed before operation in the rate mode is described.

The use of a vibrating string as a rotation angle sensor was examined by Quick [3].

In this sensor, the string was excited parametrically by a force applied along the string axis. The precession of the plane of the string vibration, relative to the case, provided the measure of the applied rotation angle. Effects of anisoelasticity (elastic asymmetry) and damping asymmetry were considered. Anisoelasticity was shown to produce an orbital vibration instead of oscillation in a plane. Nonlinear restoring forces then cause the orbit to precess causing angle measurement errors. Anisoelasticity was shown to be the dominant source of drift. The result of damping asymmetry is that the vibration plane will drift towards the axis of lowest damping.

Friedland and Hutton [28] generalized the results of Quick. The motion of a point on the resonator was described as an ellipse in the Cartesian plane formed by the two generalized coordinates associated with the two modes of vibration. When the resonator is rotated, at low rotation rates, the motion of the point can be approximated by a rotating ellipse. In order to eliminate the effects of anisoelasticity it is necessary to force the elliptical motion into a straight line. The effect of damping asymmetry was shown to be inseparable from an input rotation rate. The result is that the major axis of the ellipse rotates to align with the axis of minimum damping.

Loper and Lynch [14] described the operation and major drift mechanisms in the HRG. In the HRG, parametric excitation is used to provide energy to maintain the amplitude of vibration without affecting the position of the vibrating pattern. The control system included "quadrature control" which used an "electrical spring" to suppress the effects of anisoelasticity. The HRG used electrostatic sensing and actuation and the "electrical spring" was formed by applying a dc voltage across selected electrode gaps. The electrostatic force is proportional to the square of the gap distance. Therefore a decrease in the gap size results in an increase in the electrostatic force and vice versa. Because the variations in the gap size during operation are very small, the effect of the electrostatic field may be represented (to first order) as a negative linear spring. The dc voltage was continuously adjusted and in effect it forced the ellipse described by Friedland and Hutton to be a straight line. It is perhaps more intuitive to think of the spring being adjusted to maintain the alignment of one natural mode of vibration with the position of the vibrating pattern. In this way the hemisphere is always vibrating in only one natural

mode, even though the vibration is allowed to rotate around the circumference of the hemisphere. Asymmetric damping, which is one of the major sources of drift in the HRG, was described by two normal damping axes. The vibrating pattern tends to drift towards the axis of minimum damping, resulting in a case-oriented drift. The quadrature control does not completely eliminate the quadrature signal at the nodes of the main vibration pattern. The residual quadrature signal is at the second natural frequency and causes a "residual quadrature-vibration drift". This drift is compensated by using electrical springs to make the natural frequencies of the two modes equal. The value of the springs as a function of the vibration pattern angle is determined during a calibration procedure.

The use of the resonator as a rotation rate sensing element is more popular, especially for low cost devices. In this mode of operation the vibration pattern does not precess freely around the resonator and energy is supplied along one axis only. The effects of imperfections on the performance of vibratory gyroscopes operating in the rate mode, has received only limited attention in the literature.

The problem of a point mass imperfection in vibrating cylinder gyroscopes, was treated by Fox [29]. Fox showed that a point mass causes a split in natural frequencies and also locates the two natural mode shapes. The response to externally applied linear vibrations and off-input axis rotations was analyzed. The responses calculated are for the open loop case, where the secondary vibration mode is not controlled. In a later paper [30], Fox demonstrated that manufacturing imperfections such as wall thickness variations and various discrete features can be represented by an "equivalent point mass" if we consider the operational modes of vibration only. The general thickness variation was represented as a Fourier series and it was shown that the fourth harmonic of thickness variation needs to be considered when operating in the n=2 vibration modes. The fact that general imperfections can be represented as an "equivalent point mass" means that the effects of imperfections on natural frequency split and the location of the mode shapes, can be eliminated by introducing a second point mass during the balancing process. A method of experimental characterization of vibratory gyroscope resonators was presented by Shatalov et al. [27]. The method could identify the position and magnitude of a point mass required to balance a resonator.

A more general theory of errors was presented by Shatalov and Loveday [31]. Effects of thickness, density, elastic property and damping property variations combined with linear vibrations and off-input axis rotations were analyzed. The various forces present were classified and an expression for the open-loop drift was presented.

These analyses focused on the resonator dynamics and did not consider the effects of imperfections in the closed loop system or the design of the control system to reduce the effects of resonator imperfections.

1.4 Research Objectives

The specific objectives of this research on the effects of imperfections in piezoelectric gyroscopes were:

- To develop an approach for the modeling of piezoelectric resonators which accurately describes the electromechanical coupling. Apply the method to a piezoelectric vibrating cylinder gyroscope including various imperfections.
- To analyze the effects of elastic boundary conditions on the dynamics of thin-walled cylinders used as vibratory gyroscope resonators.
- To determine the effects of feedback control on the resonator dynamics with the intention of using feedback control to minimize the effects of imperfections.
- To investigate the role of control system design in suppressing the effects of resonator imperfections and thus improving performance.
- To examine the effects of piezoelectric property variations on the performance of vibratory gyroscopes.

1.5 Dissertation Layout

Chapter 1 presents a brief introduction to vibratory gyroscopes. The principles of operation are described and various applications are listed. A number of the major developments in the field are described and the literature on the analysis of the effects of imperfections in these devices is reviewed.

Chapters 2 and 3 focus on the modeling of the resonators used in vibratory gyroscopes. Modeling the coupled electromechanical behavior of piezoelectric resonators

is addressed in chapter 2, while the effects of elastic boundary conditions on the dynamics of rotating thin-walled cylinders is analyzed in chapter 3. The models described in these two chapters are used through out the rest of the dissertation.

The effects of feedback control on the resonator dynamics is investigated in chapter 4. The more general problem of designing the control systems used in vibratory gyroscopes to reduce the effects of imperfections is treated in chapter 5. The control functions are motivated by inspection of the equations of motion in averaged variables and methods for the analysis of the closed loop system are illustrated.

The effects of piezoelectric property variations on the closed loop performance of vibratory gyroscopes is analyzed in chapter 6, and rules for the selection or optimization of piezoelectric materials are established.

In each chapter an attempt has been made to present the general theory first, and then to demonstrate the theory by applying it to the piezoelectric vibrating cylinder gyroscope. Where possible experimental results have been used to verify the theoretical predictions. Each of the objectives listed above is treated in a separate chapter. Conclusions are included in each chapter and a general summary of these conclusions is presented in chapter 7.

Chapter Two

Piezoelectric Resonator Modeling

2.1 Introduction

The design and analysis of a vibratory gyroscope begins with a model of the resonator dynamics. In the case of the piezoelectric resonator this model is required to capture the dynamics of the resonator, the electromechanical coupling and the capacitive nature of the piezoelectric ceramics. To be able to study the effects of imperfections it is necessary to include typical manufacturing errors such as misplacement of the piezoceramic elements.

The model of the resonator can be used to optimize the dimensions of the design to achieve a required natural frequency, or to maximize the actuator authority or strain measurement sensitivity of the piezoceramic elements. If imperfections are included, a sensitivity analysis can be performed to determine the manufacturing tolerances which need to be achieved. An understanding of the effects of imperfections is required when selecting the form of compensation algorithm to be used in an inertial navigation system based on vibratory gyroscopes. Finally a good model of the resonator is required for the design of the control system.

In this chapter the derivation of a system of equations of motion for a electro-elastic body is presented. The method is applied to a piezoelectric cylinder gyroscope resonator, including imperfections. Comparison of the theoretical predictions with experimental results was performed to verify the accuracy of the model. The presentation of the research here is similar to that published by Loveday [32].

2.2 Modeling a Coupled Electro-Elastic Structure

The derivation of coupled equations of motion of an elastic structure including piezoceramic elements has been comprehensively documented by Hagood, Chung and von Flotow [33] and Hagood and Anderson [34]. Only a general outline of the procedure

which is based on Hamilton's principle and the Rayleigh - Ritz method, is presented here. The aspects which are particular to the cylindrical geometry being modeled are described in greater detail in section 2.3.

The procedure starts with Hamilton's principle for coupled electromechanical systems:

$$\int_{t_1}^{t_2}[\partial(T-U+W_e+W_m)+\partial W]dt \;=\; 0 \tag{2.1}$$

The constitutive equations for the piezoelectric material may be written:

$$\begin{bmatrix} \boldsymbol{D} \\ \boldsymbol{T} \end{bmatrix} = \begin{bmatrix} \boldsymbol{R_E}^T \boldsymbol{\varepsilon}^S \boldsymbol{R_E} & \boldsymbol{R_E}^T \boldsymbol{e} \boldsymbol{R_S} \\ -\boldsymbol{R_S}^T \boldsymbol{e_t} \boldsymbol{R_E} & \boldsymbol{R_S}^T \boldsymbol{c}^E \boldsymbol{R_S} \end{bmatrix} \begin{bmatrix} \boldsymbol{E} \\ \boldsymbol{S} \end{bmatrix} \tag{2.2}$$

The strain-displacement and field-potential relations may be written in the form:

$$\boldsymbol{S} \;=\; \boldsymbol{L}_U \; \boldsymbol{u}(x) \quad \textit{and} \quad \boldsymbol{E} \;=\; \boldsymbol{L}_\varphi \varphi(x) \tag{2.3}$$

The differential operator, $\boldsymbol{L}_U$ is particular to the elasticity problem being considered and is given in the following section for the cylindrical shell being modeled. In the Rayleigh-Ritz method, the displacement and potential distributions are represented by a combination of assumed distributions each multiplied by a generalized coordinate.

$$\boldsymbol{u}(x,t) \;=\; \boldsymbol{\Psi_r}(x)\boldsymbol{r}(t) \;=\; [\psi_{r_1}(x) \;\cdots\; \psi_{r_n}(x)] \begin{bmatrix} r_1(t) \\ \vdots \\ r_n(t) \end{bmatrix} \tag{2.4a}$$

$$\varphi(x,t) \;=\; \boldsymbol{\Psi_v}(x)\boldsymbol{v}(t) \;=\; [\psi_{v_1}(x) \;\cdots\; \psi_{v_m}(x)] \begin{bmatrix} v_1(t) \\ \vdots \\ v_m(t) \end{bmatrix} \tag{2.4b}$$

Strain and electric field basis functions were defined:

$$\boldsymbol{S}(x,t) = \boldsymbol{N}_r(x)\boldsymbol{r}(t) \qquad \boldsymbol{E}(x,t) = \boldsymbol{N}_v(x)\boldsymbol{v}(t) \tag{2.5}$$

where,

$$\boldsymbol{N}_r(x) = \boldsymbol{L}_u\boldsymbol{\Psi}_r(x) \qquad \boldsymbol{N}_v(x) = \boldsymbol{L}_\varphi\boldsymbol{\Psi}_v(x) \tag{2.6}$$

After substituting these equations into Hamilton's principle and taking variations, the following system of equations in the generalized coordinates is obtained,

$$(\boldsymbol{M}_s+\boldsymbol{M}_p)\ddot{\boldsymbol{r}} + (\boldsymbol{K}_s+\boldsymbol{K}_p)\boldsymbol{r} - \boldsymbol{\Theta}\boldsymbol{v} = \boldsymbol{B}_f\,\boldsymbol{f} \tag{2.7a}$$

$$\boldsymbol{\Theta}^T\boldsymbol{r} + \boldsymbol{C}_p\boldsymbol{v} = \boldsymbol{B}_q\,\boldsymbol{q} \tag{2.7b}$$

where the mass and stiffness matrices for the structure and the piezoceramic are,

$$\boldsymbol{M}_s = \int_{V_s} \boldsymbol{\Psi}_r^T(x)\rho_s(x)\boldsymbol{\Psi}_r(x)dV \qquad \boldsymbol{M}_p = \int_{V_p} \boldsymbol{\Psi}_r^T(x)\rho_p(x)\boldsymbol{\Psi}_r(x)dV \tag{2.8}$$

$$\boldsymbol{K}_s = \int_{V_s} \boldsymbol{N}_r^T\boldsymbol{c}_s\boldsymbol{N}_r dV \qquad \boldsymbol{K}_p = \int_{V_p} \boldsymbol{N}_r^T\boldsymbol{R}_S^T\boldsymbol{c}^E\boldsymbol{R}_S\boldsymbol{N}_r dV \tag{2.9}$$

and the capacitance matrix ($\boldsymbol{C}_p$), the piezoelectric coupling matrix ($\boldsymbol{\Theta}$) and the mechanical and electrical forcing matrices are defined as:

$$\boldsymbol{C}_p = \int_{V_p} \boldsymbol{N}_v^T\boldsymbol{R}_E^T\boldsymbol{\varepsilon}^S\boldsymbol{R}_E\boldsymbol{N}_v dV \tag{2.10}$$

$$\boldsymbol{\Theta} = \int_{V_p} \boldsymbol{N}_v^T\boldsymbol{R}_S^T\boldsymbol{e}_t\boldsymbol{R}_E\boldsymbol{N}_v dV \tag{2.11}$$

$$\boldsymbol{B_f} = \begin{bmatrix} \psi_{r_1}{}^T(x_{f_1}) & \cdots & \psi_{r_1}{}^T(x_{f_{nf}}) \\ \vdots & & \vdots \\ \psi_{r_n}{}^T(x_{f_1}) & \cdots & \psi_{r_n}{}^T(x_{f_{nf}}) \end{bmatrix} \tag{2.12}$$

$$\boldsymbol{B_q} = \begin{bmatrix} \psi_{v_1}{}^T(x_{q_1}) & \cdots & \psi_{v_1}{}^T(x_{q_{nf}}) \\ \vdots & & \vdots \\ \psi_{v_n}{}^T(x_{q_1}) & \cdots & \psi_{v_n}{}^T(x_{q_{nf}}) \end{bmatrix} \tag{2.13}$$

Equation 2.7 describes the dynamics of the coupled electro-elastic structure. Equation 2.7a is referred to as the actuator equation while 2.7b is referred to a the sensor equation [33].

2.3 Application to the Vibrating Cylinder Gyroscope Resonator

The geometry and the coordinate system utilized in this model is shown in Fig. 2.1. The two aspects of the procedure which are particular to the cylindrical geometry are the selection of appropriate strain-displacement relations and the selection of suitable assumed displacement and potential functions.

A number of different strain-displacement equations are presented in the literature (see Leissa, [35]). The equations that are used in this chapter are those due to Love and Timoshenko. The strain-displacement equations [36] are written in matrix form in equation 2.14. This equation defines the differential operator, $\boldsymbol{L}_U$, used in equation 2.3.

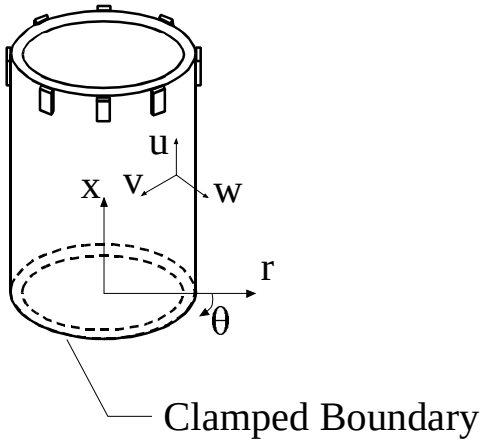

Figure 2.1 Vibrating cylinder gyroscope geometry and coordinate system utilized in the resonator model.

$$\begin{bmatrix} \varepsilon_x' \\ \varepsilon_\theta' \\ \varepsilon_z' \\ \varepsilon_{\theta z}' \\ \varepsilon_{xz}' \\ \varepsilon_{x\theta}' \end{bmatrix} = \begin{bmatrix} \frac{\partial}{\partial x} & 0 & -z\frac{\partial^2}{\partial x^2} \\ 0 & (\frac{1}{a}+\frac{z}{a^2})\frac{\partial}{\partial\theta} & \frac{1}{a}-\frac{z}{a^2}\frac{\partial^2}{\partial\theta^2} \\ 0 & 0 & 0 \\ 0 & 0 & 0 \\ 0 & 0 & 0 \\ \frac{1}{a}\frac{\partial}{\partial\theta} & (1+2\frac{z}{a})\frac{\partial}{\partial x} & -2\frac{z}{a}\frac{\partial^2}{\partial x\partial\theta} \end{bmatrix} \begin{bmatrix} u \\ v \\ w \end{bmatrix} \tag{2.14}$$

In equation 2.14, z is the distance from the mid surface of the shell, measured positive outwards.

Fox [29] used the Rayleigh-Ritz method with the Lagrange equations to obtain equations of motion of a cylinder closed at one end and open at the other. The assumed displacements used, were based on a combination of a circumferential wave and the cantilever beam functions. According to Warburton [36], the natural frequencies predicted by this method agree reasonably accurately with solutions that satisfy the shell theory equations and all the boundary conditions. The assumed displacement distributions used here are essentially two assumed modes of vibration, one rotated by 45° with respect to the other, and may be written as follows:

$$\begin{aligned} u(x,\theta) &= U_1 H(x)\cos 2\theta + U_2 H(x)\sin 2\theta \\ v(x,\theta) &= V_1 F(x)\sin 2\theta + V_2 F(x)\cos 2\theta \\ w(x,\theta) &= W_1 F(x)\cos 2\theta + W_2 F(x)\sin 2\theta \end{aligned} \tag{2.15}$$

where U_1, U_2, V_1, V_2, W_1 and W_2 are generalized coordinates and $F(x)$ and $H(x)$ are the cantilever beam functions:

$$F(x) = \cosh \lambda_1 x - \cos \lambda_1 x - \sigma_1(\sinh \lambda_1 x - \sin \lambda_1 x)$$
$$H(x) = \frac{1}{\lambda_1}\frac{dF}{dx} = \sinh \lambda_1 x - \sin \lambda_1 x - \sigma_1(\cosh \lambda_1 x + \cos \lambda_1 x) \tag{2.16}$$

For the case of a cantilever beam $\lambda_1 l = 1.8751$ and $\sigma_1 = 0.7340955$ [37].

The electrical potential is assumed to vary only in the radial direction, through the thickness of the ceramics. A linear variation in electrical potential for each of the eight ceramic elements may be represented as follows:

$$\varphi_i(z,t) = (\frac{z - h/2}{h_c})\nu_i(t) \qquad (i = 1 \text{ to } 8) \tag{2.17}$$

The electrical potential at the inner radius of the ceramic element is zero and the generalized coordinate $\nu_i(t)$ represents the electrical potential at the outer radius of the ceramic.

The equations of motion are obtained by substitution of the equations in this section into the equations of the previous section. The equations of motion of the coupled system may be written in the following form:

$$\begin{bmatrix} \boldsymbol{M}_{s_1}+\boldsymbol{M}_{p_1} & \boldsymbol{M}_{coup} \\ \boldsymbol{M}_{coup} & \boldsymbol{M}_{s_2}+\boldsymbol{M}_{p_2} \end{bmatrix} \begin{bmatrix} \ddot{U}_1 \\ \ddot{V}_1 \\ \ddot{W}_1 \\ \ddot{U}_2 \\ \ddot{V}_2 \\ \ddot{W}_2 \end{bmatrix} + \begin{bmatrix} \boldsymbol{K}_{s_1}+\boldsymbol{K}_{p_1} & \boldsymbol{K}_{coup} & -\boldsymbol{\Theta}_1 \\ \boldsymbol{K}_{coup} & \boldsymbol{K}_{s_2}+\boldsymbol{K}_{p_2} & -\boldsymbol{\Theta}_2 \\ -\boldsymbol{\Theta}_1^T & -\boldsymbol{\Theta}_2^T & -\boldsymbol{C}_p \end{bmatrix} \begin{bmatrix} U_1 \\ V_1 \\ W_1 \\ U_2 \\ V_2 \\ W_2 \\ \nu_1 \\ \vdots \\ \nu_8 \end{bmatrix} = \begin{bmatrix} \boldsymbol{B}_{f_1}\boldsymbol{f} \\ \boldsymbol{B}_{f_2}\boldsymbol{f} \\ -\boldsymbol{B}_q\boldsymbol{q} \end{bmatrix} \tag{2.18}$$

In this chapter only the non-rotating cylinder is treated. In chapter 5 the control system is analyzed. This requires the inclusion of Coriolis effects in the form of a gyroscopic matrix. The derivation of the gyroscopic matrix , the mass matrix and a single term of the stiffness matrix is outlined in appendix A.

Mechanical coupling between the assumed modes of vibration occurs when there is a mechanical imperfection such as a point mass or a misplaced ceramic element. In the ideal case the mechanical coupling matrices are zero and the natural modes of the system correspond to the assumed modes. When imperfections are present the natural modes of the system are linear combinations of the assumed modes. These equations of motion were used to obtain the results presented in section 2.4.

2.4 Results

The dimensions used in the model are shown in Fig. 2.2. The experimental devices differ in certain details from the model. In practice, the ceramic elements are not curved, but are rectangular blocks which are soldered onto flat spots machined on the cylinder. The perfectly clamped boundary condition assumed in the model is obviously not achievable in practice and thin wires are glued to the sides of the cylinder to make electrical contact with the ceramics.

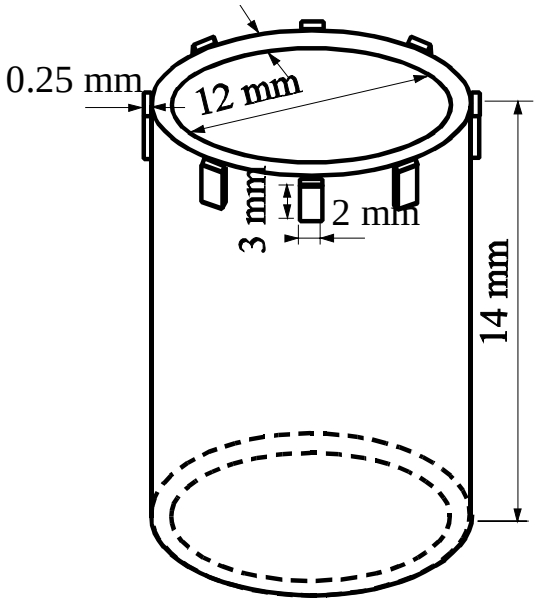

Figure 2.2 Physical dimensions used in the resonator model.

2.4.1 Ideal Device

The natural frequency predicted by the model was 19.845 kHz. This is significantly higher than the experimental results which vary between 14 kHz and 16 kHz. The main reasons for this error are believed to be flexibility in the "clamped" boundary condition, which is investigated in chapter 3, and the decrease in stiffness caused by machining the flat spots on the cylinder. The error in natural frequency does not severely limit the usefulness of the model. The ratio of the generalized coordinates describes the mode shape of the structure. The ratio U_1: V_1: W_1 was calculated to be -0.155:-0.493:1 which represents a ratio in the maximum displacements of -0.114:-0.493:1. It was necessary to include damping in the model so that frequency response functions could be calculated for direct comparison with experimental results. This damping was included as an imaginary stiffness component. Measured frequency responses indicated a Q-factor of 2400 and this value was used to calculate the imaginary component of the stiffness matrix. The measurement was performed in a partial vacuum (pressure less than 1 Pa) and therefore acoustic radiation losses were negligible.

The calculated and measured electrical admittance of one ceramic element, with the other seven elements open circuited, is shown in Fig. 2.3. The resonance appears to be more pronounced in the measured admittance than in the calculated admittance even though the two curves have the same Q factor. An effective coupling coefficient for piezoelectric transducers based on the maximum and minimum admittance frequencies can be defined as follows [38]:

$$k_{eff}^2 = \frac{f_{\max}^2 - f_{\min}^2}{f_{\max}^2} \tag{2.19}$$

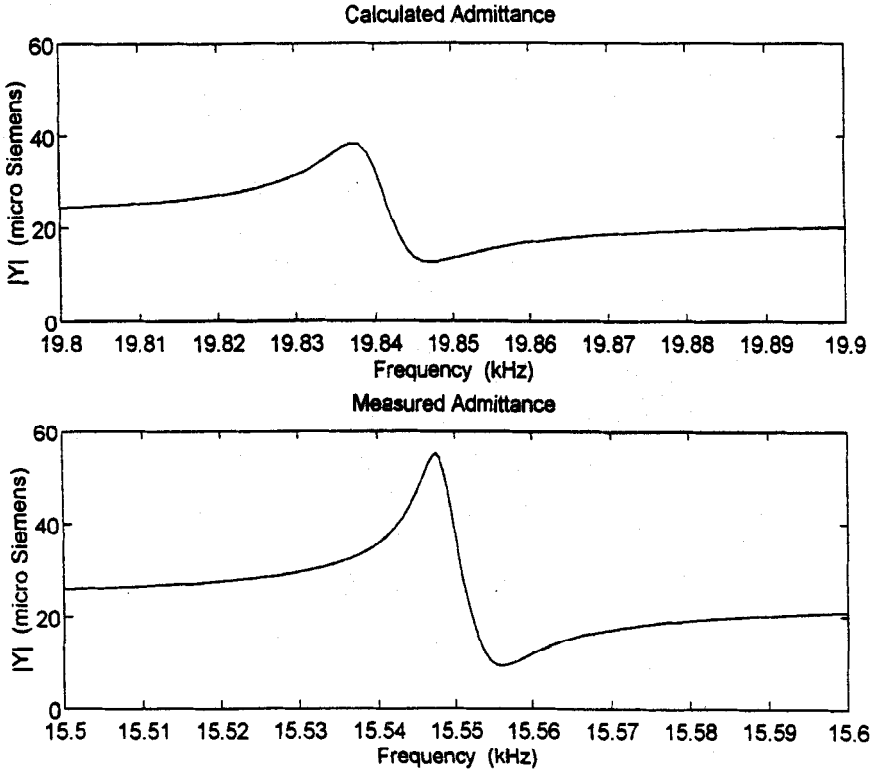

Figure 2.3 Comparison of calculated and measured electrical admittance of one piezoceramic element.

Applying equation 2.19 to the calculated and measured data produces effective coupling factors of 0.0317 and 0.0321 respectively. This indicates that the model correctly simulates the electromechanical coupling in the structure.

In the operation of the device, the two opposite ceramics (180° apart) are commonly used as actuators and the pair of ceramic elements 90° away are used as sensors. The voltage frequency response corresponding to this situation is easily calculated and measured. These results are shown in Fig. 2.4. The correlation between the calculated and measured maximum amplitudes is well within the range of experimental variation from one device to the next. The calculated maximum radial displacement for a one Volt excitation was 0.5 μm. It is interesting to note that even at this small amplitude some nonlinear softening behavior was observed in the measured response.

2.4.2 Imperfect Device

The first imperfection considered was a point mass defect. A point mass situated at the lip of the cylinder at an angle of $\theta = 0$ was included in the model. The effect of the added mass was to decrease the natural frequencies of the two modes. The one natural frequency is decreased more than the other, resulting in a separation of natural frequencies which is undesirable for the operation of the device. Because the added mass is very small compared to the mass of the structure, the changes in frequency are approximately linearly dependent on the magnitude of mass addition. It was found that the natural frequency separation is approximately 19 Hz per 1 mg of mass addition. In this case, the natural mode shapes correspond to the two assumed displacement distributions described by U1,V1,W1 and U2,V2,W2 respectively. If the point mass is located at an angle θ where the product of $\cos(2\theta)$ and $\sin(2\theta)$ is non zero then coupling between the two assumed displacement functions occurs in the mass matrix. This coupling causes the resultant mode shapes to be a linear combination of the two assumed displacement functions. The important result here is that the location of the point mass defect determines the position of the two natural mode shapes. A nodal point, of radial motion, of the higher frequency mode and an anti-nodal point of the lower frequency mode will coincide with the point mass location. For example, a 1 mg point mass located at $\theta = 15^{o}$ resulted in a frequency

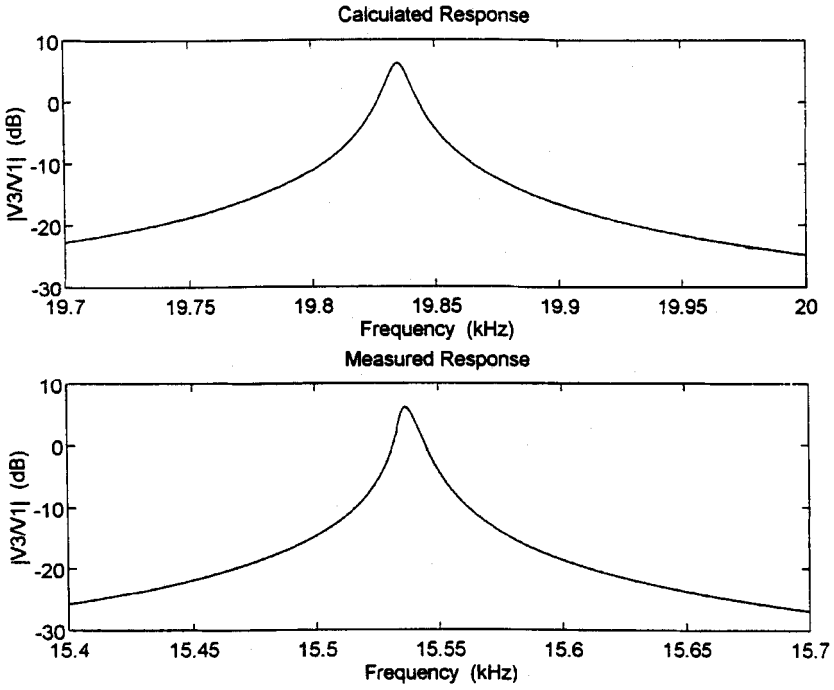

Figure 2.4 Calculated and measured voltage response functions illustrating the accuracy of the amplitude prediction.

difference of 19 Hz and produced natural modes with generalized displacements of [U1,V1,W1,U2,V2,W2] = [0.119;0.380;-0.769;0.069;-0.219;-0.444] and [0.069;0.219;-0.444;-0.119;0.380;0.769].

To verify this effect experimentally a point mass of 1.55 mg was added to a device at an angle of approximately $\theta = 22.5^{o}$. The device had previously been fine-tuned, by mechanical balancing, to have a natural frequency separation of less than 0.5 Hz. Voltage frequency responses were measured before and after the mass addition. These responses were measured by exciting one pair of ceramic elements and measuring the response at the pair of ceramic elements located at 90^{o} and at the pair at 45^{o}. The mass addition was included in the model and responses analogous to the measured responses were calculated. The measured and calculated responses are shown in Figs. 2.5 and 2.6 respectively.

These measurements were conducted in air and the measured Q factor of 1600 was used in the model. The results clearly show the separation of natural frequencies and the location of the natural mode shapes not coinciding with the ceramic locations. The calculated responses are slightly larger than the experimental responses but it must be remembered that the point mass is not the only imperfection present in the experimental device. The presence of other imperfections is evident in the 45^{o} response of the device before the point mass was added. In a perfect device this response would only be due to the presence of other modes and would not show these resonances. The model does not include the effects of other modes so the 45^{o} response, predicted for the perfect device, was zero and was not plotted.

The second imperfection considered is the misplacement of a single ceramic element. This imperfection may be thought of as a combination of point mass addition and removal, point stiffness addition and removal and an error in the angle of forcing or sensing. The effect of this imperfection on the natural frequency separation between the two modes was found to be 2.76 Hz per 1^{o} of misplacement for small placement errors. In this case even a very small location error causes the mode shapes to be orientated so that a node and an anti-node are located at 22.5^{o}.

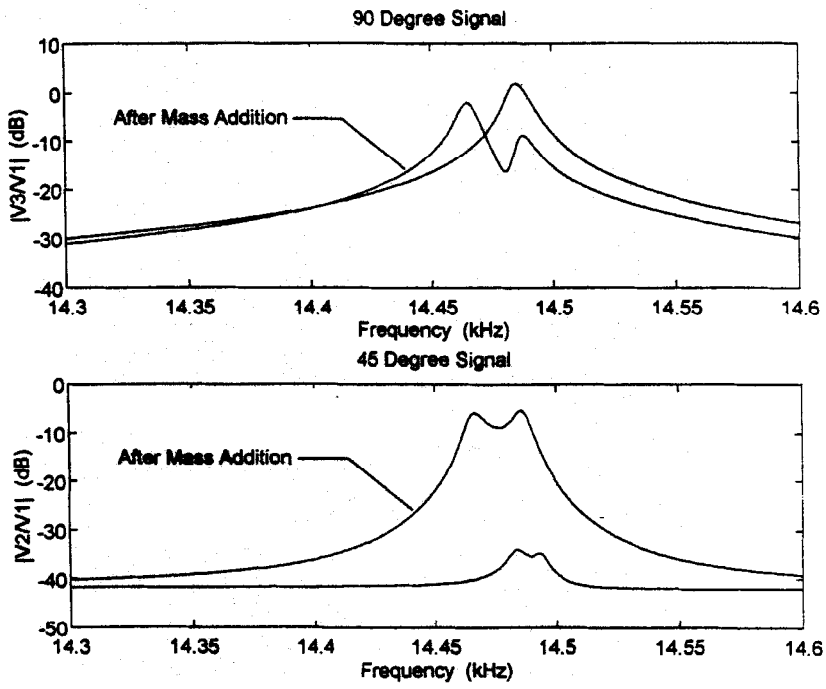

Figure 2.5 Splitting of resonant frequencies caused by the point mass addition - measured voltage response functions.

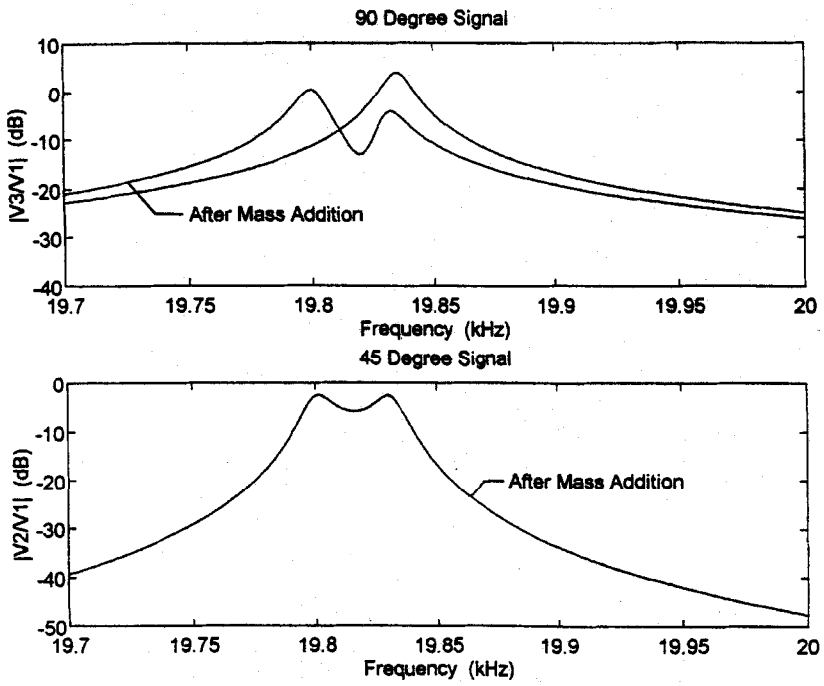

Figure 2.6 Predicted splitting of resonant frequencies caused by the point mass addition - calculated voltage response functions.

2.5 Conclusions

The application of Hamilton's principle and the Rayleigh-Ritz method provided an effective approach for modeling the dynamics of piezoelectric resonators. A coupled electromechanical model of a piezoelectric vibrating cylinder gyroscope resonator was developed. Ceramic location errors and point mass defects were included in the model to simulate typical imperfections in these structures. Comparisons with experimental results indicate that the model could be used to predict the mass modifications required to reduce the effect of imperfections on production devices. The sensitivities to manufacturing imperfections such as piezoceramic misplacement can be determined from this model, and used to specify manufacturing tolerances. The model is suitable for use during design of the control system.

Chapter Three

Elastic Boundary Conditions

3.1 Introduction

A resonator used in a vibratory gyroscope requires a robust means of support which does not interfere with the vibration of the resonator. The requirements that the resonator be accurately aligned with the housing, rugged and lightly damped, places demands on the design of the supporting structure. It is desirable that as little energy as possible be transmitted from the resonator through the support because this represents a damping loss. It is also necessary that changes in the gyroscope housing are not transmitted via the support to the resonator where these changes may cause performance degradation. Although electrostatic suspension of a ring resonator was patented by Stiles [39] this has not been successfully implemented in a product. A vibration node represents an ideal location for mechanically mounting the resonator and this has been attempted in beam resonators. Cylinder and hemisphere resonators are generally mounted on a stem. Models of cylindrical resonators usually assume that the closed end of the cylinder is rigid, and a clamped boundary condition is applied. In the previous chapter it was found that such a model produced a significant error in resonant frequency prediction. In this chapter the free vibration of an elastically supported cylinder is studied. The effect of the boundary stiffnesses on the natural frequency and the sensitivity to rotation are investigated as these effects are of importance during resonator design. The research reported here is essentially the same as that published by Loveday and Rogers [40].

3.2 Vibration of Rotating Thin Cylinders

The vibration of thin elastic shells has been studied by many researchers. The results of many of these studies have been summarised by Leissa [35] and Blevins [41]. The literature contains numerous analyses of thin cylindrical shells with ideal boundary conditions classed for example, as clamped, free, simply supported with axial constraint

and simply supported without axial constraint. In reality, the perfect clamped boundary condition cannot be achieved as there will always be some flexibility in the support. The effects of this flexibility are investigated in this chapter.

The effect of rotation on the vibration of a cylinder was first analysed by Bryan [8] in 1890. Bryan showed that rotation causes the nodes of a standing wave pattern to rotate relative to the cylinder. The vibrating pattern lags behind the rotation of the cylinder. This effect, which is referred to as the Bryan effect, is used today in a class of angular rotation rate sensors which are based on vibrating cylinders [16,18,29,32]. The influence of boundary conditions on the natural frequencies and sensitivity to rotation is important in the design of these sensors.

Three methods are generally applied to the analysis of thin, cylindrical shell vibration. An exact solution of waves propagating in infinite, hollow cylinders, based on the three-dimensional theory of elasticity, was described by Armenàkas et al. [42]. This solution is also valid for simply supported shells and serves as a benchmark against which results from analyses based on shell theories can be evaluated. Approximate analyses based on various shell theories have been performed using the Rayleigh-Ritz method [35,41]. An exact solution of the Flügge shell theory equations of motion has been performed by various authors [43-46] in which different ideal boundary conditions were analysed. The solutions achieved by this approach are accurate within the limits of the shell theory used.

In this work the general analysis procedure presented by Warburton [44] is adopted and extended to include elastic boundary conditions and rotation of the cylindrical shell. The elastic boundary conditions are represented by distributed springs along the edges of the cylinder. By varying the stiffness coefficients of these springs it is possible to represent any of the ideal boundary conditions and also to investigate the effect of departures from the ideal conditions. Using this method, the effect of elastic boundary conditions on the free vibrations of cylindrical shells can be quantified.

3.3 Theoretical Formulation

The derivation presented here follows that of Warburton [44], but includes the elastic supports in the potential energy and the rotation rate in the kinetic energy. The effect of centrifugal forces producing a deformed equilibrium position with stresses which contribute to the potential energy has been neglected. Analysis of high rotation rates requires the calculation of the stresses in the equilibrium position which is beyond the scope of the present paper. Centrifugal forces arising from the kinetic energy, which are proportional to the square of the rotation rate, have therefore also been neglected. The analysis is therefore only valid for rotation rates well below the natural frequencies of interest.

3.3.1 Kinetic and Potential Energy Expressions

The kinetic energy of the rotating cylinder may be written as follows:

$$T = \frac{\rho h a}{2}\int_0^{2\pi}\int_0^{L}\left(\frac{\partial u}{\partial t}\right)^2+\left(\frac{\partial v}{\partial t}-\Omega(a+w)\right)^2+\left(\frac{\partial w}{\partial t}+\Omega v\right)^2 dx\,d\phi \qquad (3.1)$$

The potential energy of the system is the sum of the strain energy of the cylindrical shell and the strain energy stored in the elastic boundaries. Flügge shell theory was used. Therefore four distributed springs are required to represent the elastic boundary conditions at each end of the cylinder as shown in Fig. 3.1.

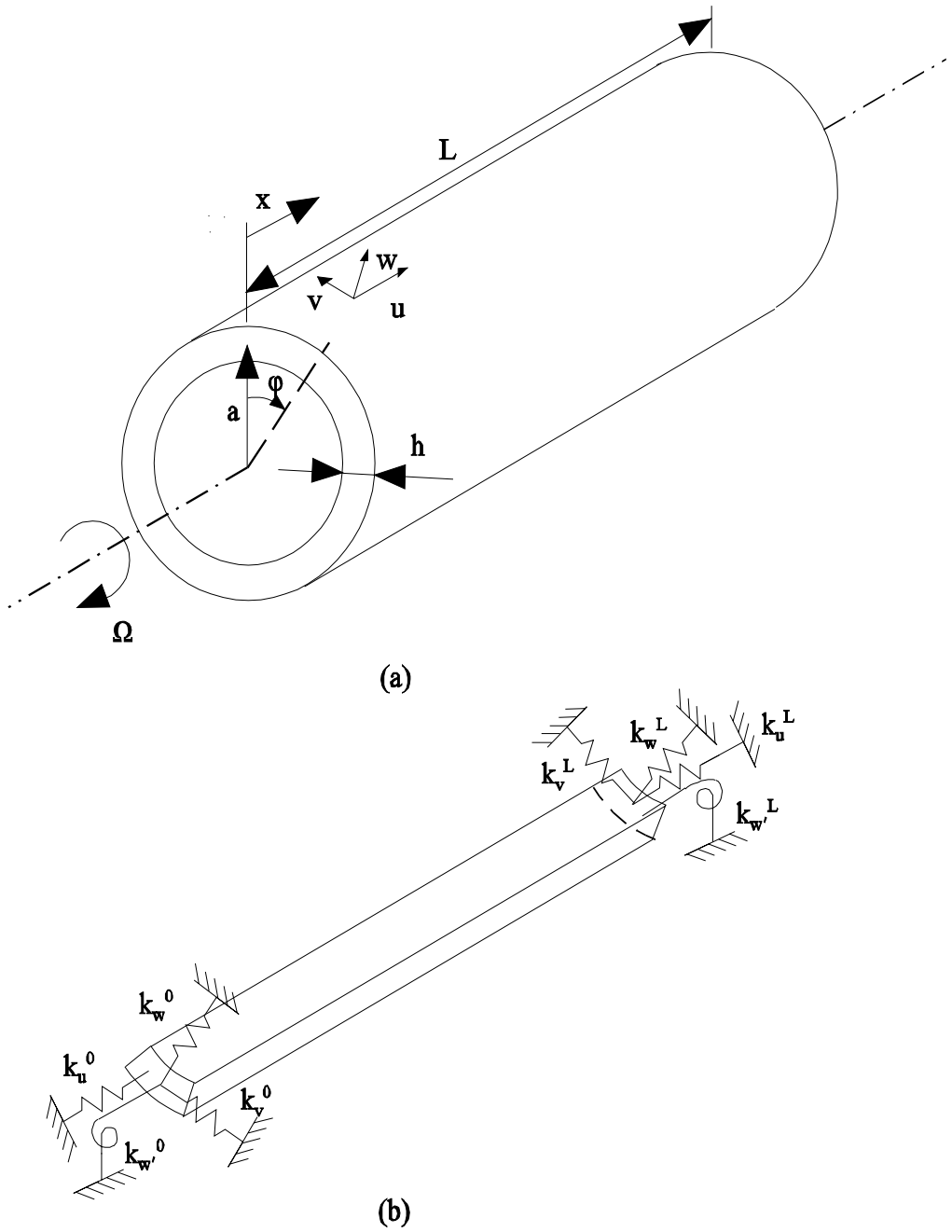

Figure 3.1 (a) Definition of coordinates and dimensions.
(b) Elastic boundary conditions shown on a segment of the cylinder.

The potential energy of the cylinder and elastic boundary conditions may be written as follows (note that the radial displacement is defined as positive outwards while in [44] it was positive inwards):

$$
\begin{aligned}
S = \frac{Eah}{2(1-\nu^2)}\int_0^{2\pi}\int_0^{L}\Bigg[&\left(\frac{\partial u}{\partial x}\right)^2+\frac{1}{a^2}\left(\frac{\partial v}{\partial \phi}\right)^2+\frac{w^2}{a^2}+\frac{2w}{a^2}\frac{\partial v}{\partial \phi}+\frac{2\nu}{a}\frac{\partial u}{\partial x}\frac{\partial v}{\partial \phi}\\
&+\frac{2\nu}{a}\frac{\partial u}{\partial x}w+\frac{1}{2a^2}(1-\nu)\left(\frac{\partial u}{\partial \phi}\right)^2+\frac{1}{2}(1-\nu)\left(\frac{\partial v}{\partial x}\right)^2+\frac{1}{a}(1-\nu)\frac{\partial u}{\partial \phi}\frac{\partial v}{\partial x}\\
&+\beta\Bigg\{a^2\left(\frac{\partial^2 w}{\partial x^2}\right)^2+\frac{1}{a^2}\left(\frac{\partial^2 w}{\partial \phi^2}\right)^2+\frac{w^2}{a^2}+\frac{2w}{a^2}\frac{\partial^2 w}{\partial \phi^2}+2\nu\frac{\partial^2 w}{\partial x^2}\frac{\partial^2 w}{\partial \phi^2}\\
&+2(1-\nu)\left(\frac{\partial^2 w}{\partial x\partial \phi}\right)^2+\frac{1}{2a^2}(1-\nu)\left(\frac{\partial u}{\partial \phi}\right)^2+\frac{1}{a}(1-\nu)\frac{\partial u}{\partial \phi}\frac{\partial^2 w}{\partial x\partial \phi}\\
&-2a\frac{\partial u}{\partial x}\frac{\partial^2 w}{\partial x^2}+\frac{3}{2}(1-\nu)\left(\frac{\partial v}{\partial x}\right)^2-2\nu\frac{\partial v}{\partial \phi}\frac{\partial^2 w}{\partial x^2}-3(1-\nu)\frac{\partial v}{\partial x}\frac{\partial^2 w}{\partial x\partial \phi}\Bigg\}\Bigg]d\phi dx\\
&+\frac{1}{2}a\int_0^{2\pi}\left[k_u^0 u^2+k_v^0 v^2+k_w^0 w^2+k_{w'}^0\left(\frac{\partial w}{\partial x}\right)^2\right]_{x=0}\\
&+\left[k_u^L u^2+k_v^L v^2+k_w^L w^2+k_{w'}^L\left(\frac{\partial w}{\partial x}\right)^2\right]_{x=L}d\phi
\end{aligned}
\tag{3.2}
$$

3.3.2 Equations of Motion and Boundary Conditions

The following equations of motion and boundary conditions were derived by application of Hamilton's principle using the above expressions for the potential and kinetic energies. Terms proportional to the square of the rotation rate were omitted while the Coriolis forces were retained. The equations of motion in the axial, tangential and radial directions are presented in equation 3.3.

$$a\frac{\partial^2 u}{\partial x^2}+\frac{(1-\nu)}{2a}\frac{\partial^2 u}{\partial \phi^2}+\frac{(1+\nu)}{2}\frac{\partial^2 v}{\partial x\partial \phi}+\nu\frac{\partial w}{\partial x}$$
$$+\frac{h^2}{12a^2}\left[\frac{(1-\nu)}{2a}\frac{\partial^2 u}{\partial \phi^2}-a^2\frac{\partial^3 w}{\partial x^3}+\frac{(1-\nu)}{2}\frac{\partial^3 w}{\partial x\partial^2 \phi}\right]=\frac{\rho a(1-\nu^2)}{E}\left[\frac{\partial^2 u}{\partial t^2}\right];$$

$$\frac{(1+\nu)}{2}\frac{\partial^2 u}{\partial x\partial \phi}+\frac{1}{a}\frac{\partial^2 v}{\partial \phi^2}+\frac{a(1-\nu)}{2}\frac{\partial^2 v}{\partial x^2}+\frac{1}{a}\frac{\partial w}{\partial \phi}$$
$$+\frac{h^2}{12a^2}\left[\frac{3a(1-\nu)}{2}\frac{\partial^2 v}{\partial x^2}-\frac{a(3-\nu)}{2}\frac{\partial^3 w}{\partial x^2\partial \phi}\right]=\frac{\rho a(1-\nu^2)}{E}\left[\frac{\partial^2 v}{\partial t^2}-2\Omega\frac{\partial w}{\partial t}\right];\qquad(3.3)$$

$$\nu\frac{\partial u}{\partial x}+\frac{1}{a}\frac{\partial v}{\partial \phi}+\frac{1}{a}w+\frac{h^2}{12a^2}\left[\frac{(1-\nu)}{2}\frac{\partial^3 u}{\partial x\partial \phi^2}-a^2\frac{\partial^3 u}{\partial x^3}-\frac{a(3-\nu)}{2}\frac{\partial^3 v}{\partial x^2\partial \phi}+a^3\frac{\partial^4 w}{\partial x^4}\right.$$
$$\left.+2a\frac{\partial^4 w}{\partial x^2\partial^2 \phi}+\frac{1}{a}\frac{\partial^4 w}{\partial \phi^4}+\frac{2}{a}\frac{\partial^2 w}{\partial \phi^2}+\frac{1}{a}w\right]=\frac{\rho a(1-\nu^2)}{E}\left[\frac{\partial^2 w}{\partial t^2}+2\Omega\frac{\partial v}{\partial t}\right]$$

At $x = 0$ the boundary conditions are:

$$\frac{Eh}{(1-\nu^2)}\left[\frac{\partial u}{\partial x}+\frac{\nu}{a}\left(\frac{\partial v}{\partial \phi}+w\right)-\beta a\frac{\partial^2 w}{\partial x^2}\right]-k_u^0 u=0;$$

$$\frac{Eh}{2(1+\nu)}\left[\frac{\partial v}{\partial x}+\frac{1}{a}\frac{\partial u}{\partial \phi}+3\beta\left(\frac{\partial v}{\partial x}-\frac{\partial^2 w}{\partial x\partial \phi}\right)\right]-k_v^0 v=0;$$

$$\frac{Eh^3}{12(1-\nu^2)}\left[\frac{\partial^3 w}{\partial x^3}-\frac{1}{a}\frac{\partial^2 u}{\partial x^2}+\frac{(1-\nu)}{2a^3}\frac{\partial^2 u}{\partial \phi^2}+\frac{(2-\nu)}{a^2}\frac{\partial^3 w}{\partial x\partial \phi^2}-\frac{(3-\nu)}{2a^3}\frac{\partial^2 v}{\partial x\partial \phi}\right]+k_w^0 w=0;\qquad(3.4a)$$

$$\frac{Eh^3}{12(1-\nu^2)}\left[-\frac{\partial^2 w}{\partial x^2}-\frac{\nu}{a^2}\frac{\partial^2 w}{\partial \phi^2}+\frac{1}{a}\frac{\partial u}{\partial x}+\frac{\nu}{a^2}\frac{\partial v}{\partial \phi}\right]+k_{w/}^0\frac{\partial w}{\partial x}=0$$

At $x = L$ the boundary conditions are:

$$\frac{Eh}{(1-\nu^2)}\left[\frac{\partial u}{\partial x}+\frac{\nu}{a}\left(\frac{\partial v}{\partial \phi}+w\right)-\beta a\frac{\partial^2 w}{\partial x^2}\right]+k_u^L u = 0;$$

$$\frac{Eh}{2(1+\nu)}\left[\frac{\partial v}{\partial x}+\frac{1}{a}\frac{\partial u}{\partial \phi}+3\beta\left(\frac{\partial v}{\partial x}-\frac{\partial^2 w}{\partial x \partial \phi}\right)\right]+k_v^L v = 0;$$

$$\frac{Eh^3}{12(1-\nu^2)}\left[\frac{\partial^3 w}{\partial x^3}-\frac{1}{a}\frac{\partial^2 u}{\partial x^2}+\frac{1}{2a^3}(1-\nu)\frac{\partial^2 u}{\partial \phi^2}+\frac{(2-\nu)}{a^2}\frac{\partial^3 w}{\partial x \partial \phi^2}-\frac{(3-\nu)}{2a^3}\frac{\partial^2 v}{\partial x \partial \phi}\right]-k_w^L w = 0 \quad (3.4b)$$

$$\frac{Eh^3}{12(1-\nu^2)}\left[-\frac{\partial^2 w}{\partial x^2}-\frac{\nu}{a^2}\frac{\partial^2 w}{\partial \phi^2}+\frac{1}{a}\frac{\partial u}{\partial x}+\frac{\nu}{a^2}\frac{\partial v}{\partial \phi}\right]-k_{w'}^L\frac{\partial w}{\partial x} = 0$$

The boundary conditions at the ends of the cylinder provide the conditions for force equilibrium. The boundary conditions at each end of the cylinder are identical except for the sign difference in the distributed spring forces. Note that in the second boundary condition at each end of the cylinder there is a factor 3 in the term dependent on β. This factor was not present in [44] as the actual shear force instead of the effective shear force, was used in that work [45]. This difference has only a small influence on the resulting natural frequencies.

3.3.3 Solution of the Equations of Motion

The general solution, used by Warburton, represents a standing wave and is applicable for the non-rotating cylinder. For the rotating cylinder it is necessary to use the more general travelling wave solution listed in equation 3.5.

$$
\begin{aligned}
u &= U_0 e^{\alpha x/a}\cos(n\phi+\omega t)\\
v &= V_0 e^{\alpha x/a}\sin(n\phi+\omega t)\\
w &= W_0 e^{\alpha x/a}\cos(n\phi+\omega t)
\end{aligned}
\tag{3.5}
$$

Substitution of this general solution into the equations of motion (equation 3.3) yields the following system of equations:

$$
\begin{aligned}
&\left[\alpha^2-\frac{(1-\nu)}{2}n^2-\frac{(1-\nu)}{2}n^2\beta+\Delta^2\right]U_0+\left[\frac{(1+\nu)}{2}\alpha n\right]V_0\\
&\quad+\left[\nu\alpha+\beta\left\{-\alpha^3-\frac{(1-\nu)}{2}\alpha n^2\right\}\right]W_0 = 0;\\
&\left[-\frac{(1+\nu)}{2}\alpha n\right]U_0+\left[-n^2+\frac{(1-\nu)}{2}\alpha^2+\beta\frac{3(1-\nu)}{2}\alpha^2+\Delta^2\right]V_0\\
&\quad+\left[-n+\beta\frac{(3-\nu)}{2}\alpha^2 n-\frac{2\Omega}{\omega}\Delta^2\right]W_0 = 0;\\
&\left[\nu\alpha+\beta\left\{(-\alpha^3-\frac{(1-\nu)}{2}\alpha n^2\right\}\right]U_0+\left[n-\beta\frac{(3-\nu)}{2}\alpha^2 n-\frac{2\Omega}{\omega}\Delta^2\right]V_0\\
&\quad+\left[1+\beta\left\{\alpha^4-2\alpha^2n^2+n^4-2n^2+1\right\}+\Delta^2\right]W_0 = 0
\end{aligned}
\tag{3.6}
$$

where, the frequency factor, $\Delta = \omega a\sqrt{\rho(1-\nu^2)/E}$.

Nontrivial solutions of this system of equations are found by equating the determinant to zero. For a given cylinder, if the frequency factor (Δ), the rotation rate (Ω), and the number of circumferential waves (n) are specified, the determinant can be written as a quartic in α^2. In the calculation of the determinant the square and higher powers of β were neglected. The roots of this equation yield the values of α that satisfy the equations of motion and are the admissible axial wave numbers.

The frequency factor for the infinite cylinder is given by $\Delta_R^2 = \beta\frac{n^2(n^2-1)^2}{n^2+1}$.

At frequencies greater than the natural frequency of an infinite cylinder the roots have the form $\pm\alpha_1,\ \pm i\gamma_2,\ \pm(p \pm iq)$, where $\alpha_1,\ \gamma_2,\ p$ and q are real and positive [44]. Once the roots have been determined it is possible to use equation 3.6 to calculate the amplitude ratios as was done in [44]. The equations required for this procedure, including the gyroscopic terms, are included in Appendix B. The displacement functions can then be written as follows:

$$\begin{aligned} W(x) &= C_1\cosh\frac{\alpha_1 x}{a} + C_2\sinh\frac{\alpha_1 x}{a} + C_3\cos\frac{\gamma_2 x}{a} + C_4\sin\frac{\gamma_2 x}{a} \\ &\quad + e^{px/a}\left(C_5\cos\frac{qx}{a} + C_6\sin\frac{qx}{a}\right) + e^{-px/a}\left(C_7\cos\frac{qx}{a} + C_8\sin\frac{qx}{a}\right) \end{aligned} \tag{3.7a}$$

$$\begin{aligned} V(x) &= A_1C_1\cosh\frac{\alpha_1 x}{a} + A_1C_2\sinh\frac{\alpha_1 x}{a} + A_3C_3\cos\frac{\gamma_2 x}{a} + A_3C_4\sin\frac{\gamma_2 x}{a} \\ &\quad + e^{px/a}\left[(A_5C_5 + A_6C_6)\cos\frac{qx}{a} + (A_5C_6 - A_6C_5)\sin\frac{qx}{a}\right] \\ &\quad + e^{-px/a}\left[(A_5C_7 - A_6C_8)\cos\frac{qx}{a} + (A_5C_8 + A_6C_7)\sin\frac{qx}{a}\right] \end{aligned} \tag{3.7b}$$

$$\begin{aligned} U(x) &= A_2C_2\cosh\frac{\alpha_1 x}{a} + A_2C_1\sinh\frac{\alpha_1 x}{a} + A_4C_4\cos\frac{\gamma_2 x}{a} - A_4C_3\sin\frac{\gamma_2 x}{a} \\ &\quad + e^{px/a}\left[(A_7C_5 + A_8C_6)\cos\frac{qx}{a} + (A_7C_6 - A_8C_5)\sin\frac{qx}{a}\right] \\ &\quad + e^{-px/a}\left[(-A_7C_7 + A_8C_8)\cos\frac{qx}{a} + (-A_7C_8 - A_8C_7)\sin\frac{qx}{a}\right] \end{aligned} \tag{3.7c}$$

where the amplitude ratios (A_1 , ... , A_8) are real constants, defined in Appendix B, and the unknown coefficients (C_1 , ... , C_8) depend on the boundary conditions.

Substitution of the displacement functions (equation 3.7) into the boundary conditions (equation 3.4) produces a homogeneous system of equations in the unknown displacement coefficients (C_1 , ... , C_8). This system of equations may be written in matrix form and the determinant of the matrix must once again be zero for nontrivial solutions. For this determinant to be zero the correct frequency must be chosen at the beginning of the procedure and it is necessary to iteratively search for the frequencies which produce nontrivial solutions. These frequencies correspond to the natural frequencies of the cylinder for the selected number of circumferential waves. The index m is commonly used to number the axial modes starting from the lowest frequency mode (m = 1). During each iteration, the roots of the characteristic equation given by the determinant of equation 3.6 and the amplitude ratios defined in Appendix B, have to be computed.

3.3.4 The Influence of Rotation

If the cylinder is not rotating and a travelling wave solution with frequency ω is found there will also be a solution with frequency - ω because the travelling wave can travel in either direction around the cylinder. When a rotation rate is applied, the positive and negative travelling waves no longer have the same magnitude of frequency. For low rotation rates the two travelling wave solutions have almost identical amplitude ratios and may be combined and represented as a "standing wave" which rotates relative to the cylinder [47]. The rotation rate of the "standing wave" may be related to the positive and negative frequencies (ω_p and ω_q) by considering the combination of the two travelling waves as follows [47]:

$$\cos(n\varphi+\omega_p t)+\cos(n\varphi+\omega_q t) \;=\; 2\cos[n(\varphi+\frac{1}{2}(\omega_p+\omega_q)t/n)]\cos\frac{1}{2}(\omega_p-\omega_q)t \qquad (3.8)$$

This equation shows that the two travelling waves may be represented as a "standing wave" with frequency $\frac{1}{2}(\omega_p-\omega_q)$ which rotates relative to the cylinder at a

rate of $\frac{1}{2}(\omega_p+\omega_q)/n$. The ratio of this precession of the "standing wave" (relative to the cylinder) to the angular rotation rate applied to the cylinder is called the Bryan Factor and gives a measure of the sensitivity of the mode of vibration of the cylinder to rotation. The Bryan Factor is defined as follows:

$$BF = \frac{1}{2n\Omega}(\omega_p+\omega_q) \tag{3.9}$$

Bryan showed that for rings and infinite cylinders performing inextensional oscillations this factor is equal to $2/(n^2+1)$. Therefore the vibrating pattern will lag the applied rotation rate, Ω by 0.4Ω, 0.2Ω and 0.118Ω for n=2,3 and 4 respectively. The decrease in Bryan Factor with increasing number of circumferential waves is one reason that the n=2 mode is generally selected for use in vibratory gyroscopes.

For the low rotation rates being considered it is possible to calculate the Bryan Factor from the displacement functions of the non - rotating cylinder as follows [31]:

$$BF = \frac{2}{n}\frac{\int_0^L v(x)w(x)dx}{\int_0^L u(x)^2+v(x)^2+w(x)^2dx} \tag{3.10}$$

For low rotation rates, equations 3.9 and 3.10 give the same result.

3.4 Results

To verify the analysis, various non-rotating cylinders with idealised boundary conditions were analysed and compared to published results. These results, for a selection of geometries and circumferential wave numbers, are listed in table 3.1. The results for the clamped-free boundary conditions agree with the results presented in [45]. This indicates that the numerical implementation of the algorithm is correct. The comparison with results from the exact solution of the three dimensional elasticity problem [42] shows the accuracy of the method, based on Flügge shell theory, for calculating natural

frequencies of simply supported cylinders without axial constraint. It is noted that the accuracy of the method decreases as the thickness-to-radius ratio increases, and also as the number of waves around the circumference increases.

The influence of boundary stiffnesses on the natural frequencies for the case of two circumferential waves was investigated as this vibration mode is generally used in vibrating cylinder gyroscopes. Firstly, a cylinder supported at both ends with two circumferential waves, was considered. The boundary stiffness in one direction was then varied at both ends while the other stiffnesses had high values representing rigid boundaries. The natural frequency was calculated for each combination of boundary stiffnesses. For example, the value of k_u (the axial stiffness) was varied at both ends of the cylinder, while the other stiffnesses were set to a large constant value. Secondly, a cylinder supported at one end and free at the other end was considered. At the free end the spring constants were set to zero while at the supported end one spring constant was varied while the others were kept high. The spring constants may be non-dimensionalized as follows:

$$k_u^* = \frac{k_u}{Eh/L} \qquad k_v^* = \frac{k_v}{Eh/L} \qquad k_w^* = \frac{k_w}{Eh/L} \qquad k_{w'}^* = \frac{k_{w'}}{Eh^3/L}$$

The results of the analysis of the cylinder with equal boundary conditions at either end are shown in Fig. 3.2. In the figure the variation of the frequency factor with boundary stiffness for the case of two waves around the circumference is illustrated. It is seen that the tangential stiffness has a large effect on the natural frequency. The radial and radial bending stiffnesses have a smaller influence, while reducing the axial stiffness has a negligible effect. The case of a cylinder supported at one end and free at the other is illustrated in Fig. 3.3. Here it is found that the axial stiffness has an extremely large influence on natural frequency while the other stiffnesses have a smaller influence. Removing the axial constraint reduced the natural frequency of this mode by 75 %. In all cases increasing the boundary stiffnesses increased the natural frequency as expected.

The influence of boundary stiffness on Bryan Factor is presented in Fig. 3.4 for the cylinder supported at both ends and in Fig. 3.5 for the cylinder supported only at one end. It is evident that the tangential stiffness tends to decrease the Bryan Factor significantly

in the cylinder supported at both ends and to a lesser extent in the cylinder supported at one end. The axial restraint increased the Bryan Factor of the cylinder supported at one end but decreased the Bryan Factor of the cylinder supported at both ends. In general the Bryan Factor is greater and is also less sensitive to boundary stiffness variations when the cylinder is supported at only one end. The Bryan Factor of the short cylinder (L/a = 1) clamped at one end was found to be 0.3556 which is only 11 % lower than the Bryan Factor of a ring or infinite cylinder.

Table 3.1 Verification of calculated results by comparison with published results

L/a	h/a	n	m	Boundary Conditions	$\Delta_{literature}$	Δ
1.14	0.05	2	1	Clamped - Free	0.308 [45]	0.308
1.37	0.05	4	1	Clamped - Free	0.245 [45]	0.245
1	0.05	4	1	Simply Supported- Simply Supported	0.492 [42]	0.496
1	0.1	4	1	Simply Supported- Simply Supported	0.752 [42]	0.779
1	0.05	2	1	Simply Supported- Simply Supported	0.675 [42]	0.677
1	0.1	2	1	Simply Supported- Simply Supported	0.738 [42]	0.747

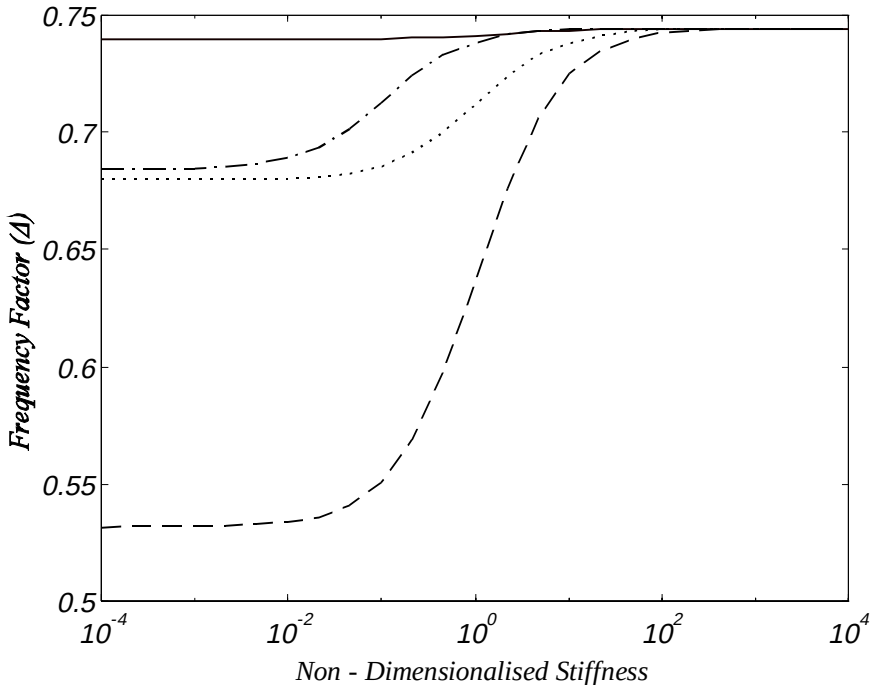

Figure 3.2 Influence of boundary stiffness on the frequency factor of a steel cylinder supported at both ends showing that the tangential stiffness had the strongest influence. ——, varying k_u^*; – – –, varying k_v^*; – · – · –, varying k_w^*; · · · ·, varying $k_{w,x}^*$. (L/a = 1, h/a = 0.05, a = 6.25 mm, n=2)

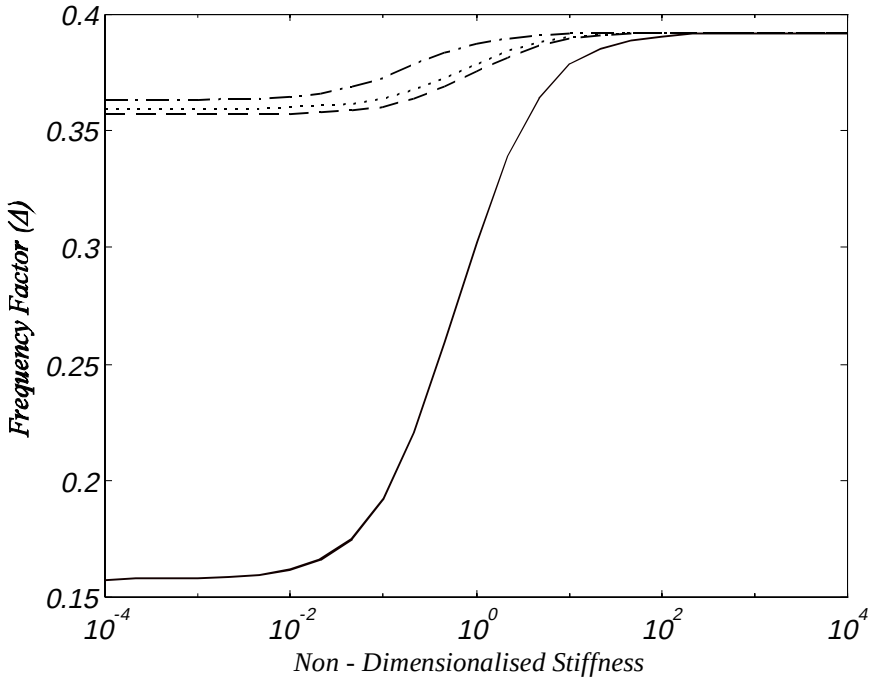

Figure 3.3 Influence of boundary stiffness on the frequency factor of a steel cylinder supported at one end showing that the axial stiffness had the strongest influence. ––––, varying k_u^*; – – –, varying k_v^*; – · – · –, varying k_w^*; · · · · , varying k_w^*. (L/a = 1, h/a = 0.1, a = 6.25 mm, n=2)

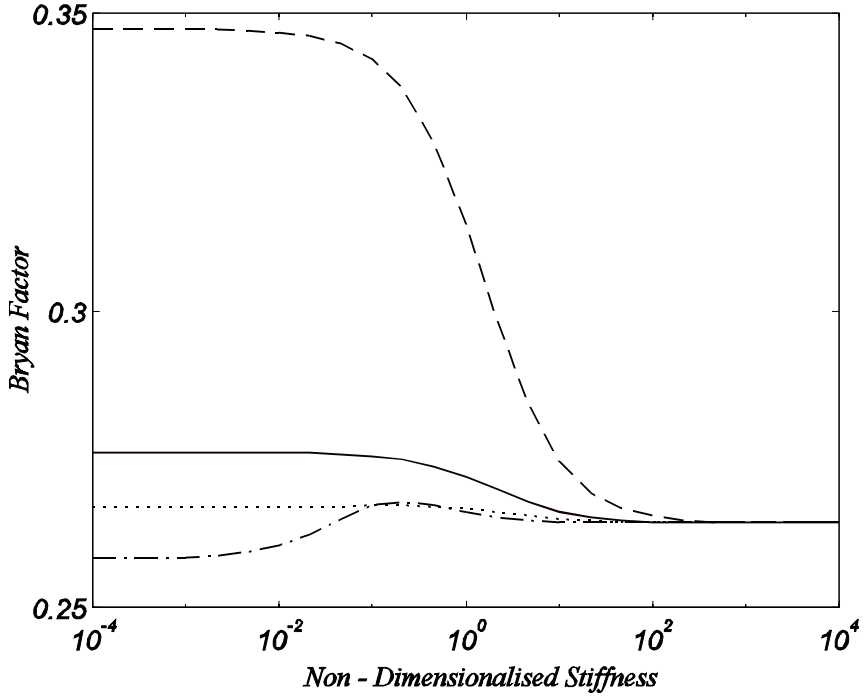

Figure 3.4 The significant influence of boundary stiffness on Bryan Factor of a steel cylinder supported at both ends. ——, varying k_u^*; – – –, varying k_v^*; – · – · –, varying k_w^*; · · · · , varying k_w^*. (L/a = 1, h/a = 0.05, a = 6.25 mm, n = 2)

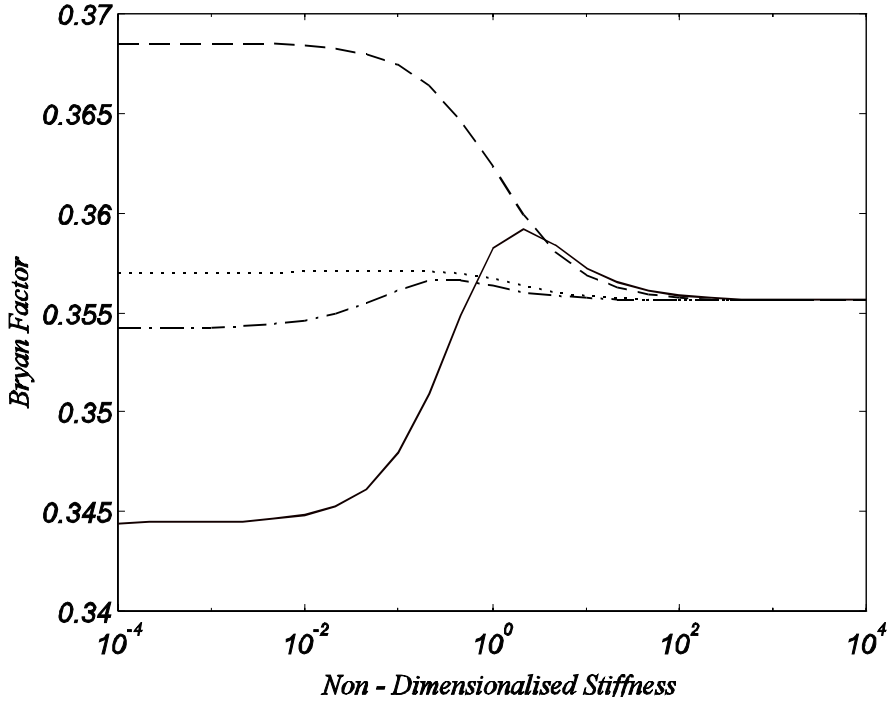

Figure 3.5 The relatively small influence of boundary stiffness on Bryan Factor of a steel cylinder supported at one end. ----, varying k_u^*; – – –, varying k_v^*; – · – · –, varying k_w^*; · · · · , varying $k_{w'}^*$. (L/a = 1, h/a = 0.1, a = 6.25 mm, n = 2)

Equation 10 shows that the Bryan Factor is dependent on the product of the tangential and radial displacements integrated over the length of the cylinder. It appears that restraining the tangential motion of the ends of the cylinder (for the n=2 case) tends to reduce the tangential motion and therefore reduces the Bryan Factor. The axial displacement reduces the Bryan Factor and it is expected that the Bryan Factor of finite cylinders will be less than that of rings or infinite cylinders, performing inextensional vibrations, where the axial displacement is zero.

Finally, the case of n=4 was analysed following the same procedure as was used in the n=2 investigation. Although this mode is not generally used in vibratory gyroscopes it was studied to determine if the trends for the n=2 case are repeated. The results of this analysis are shown in Figs. 3.6 to 3.9. It was found that in the cylinder supported at both ends the radial and the radial bending stiffnesses had the largest influence on the natural frequency while in the cylinder supported at only one end the radial stiffness had the largest influence followed by the axial and rotational stiffnesses. The Bryan Factor was decreased by the axial restraint when both ends and when one end was supported. The Bryan Factor was not influenced by the tangential stiffness when one end was supported as it was in the n=2 case. The Bryan factor was close to that of a ring (0.118) for both cases and was not greatly reduced by supporting both ends as it was in the n=2 case.

The different trends observed in the results for n=2 and n=4 make it impossible to make general statements about the effects of the various boundary stiffnesses on the frequency factors and Bryan Factors. It is therefore necessary to examine each mode of interest and to draw conclusions for each mode separately.

It was observed that the changes in natural frequency and Bryan Factor occur when the non-dimensionalized stiffness is between 10^{-2} and 10^{2}. This indicates that it is only necessary to consider the boundaries as elastic when they have stiffnesses within this range. If the boundaries have stiffnesses outside this range it is possible to treat the boundary stiffnesses as either zero or infinite as is done in the idealised boundary conditions.

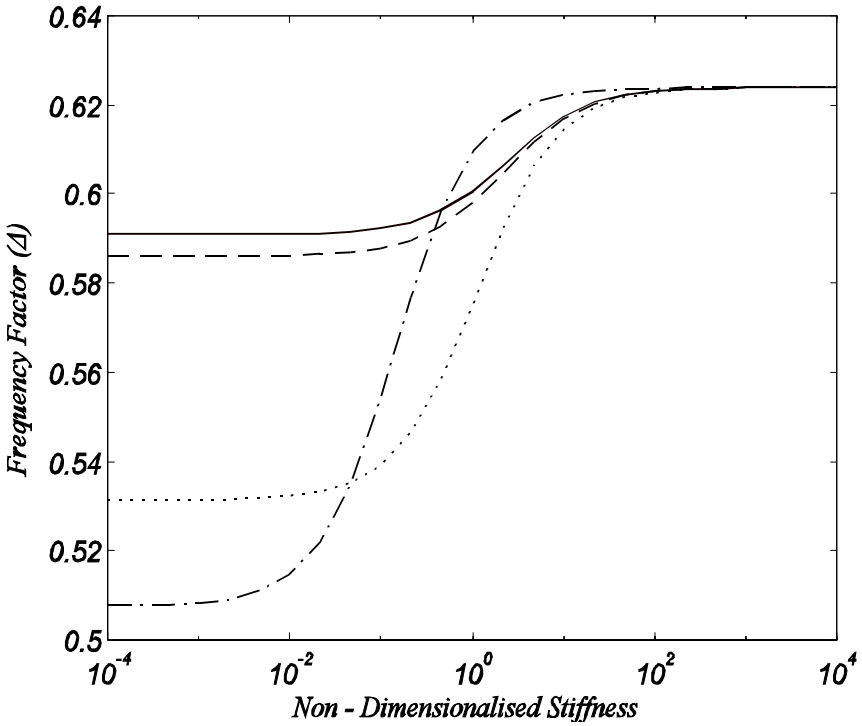

Figure 3.6 Influence of boundary stiffness on frequency factor of a steel cylinder supported at both ends. ——, varying k_u^*; – – –, varying k_v^*; – · – · –, varying k_w^*; · · · ·, varying $k_{w'}^*$. (L/a = 1, h/a = 0.05, a = 6.25 mm, n = 4)

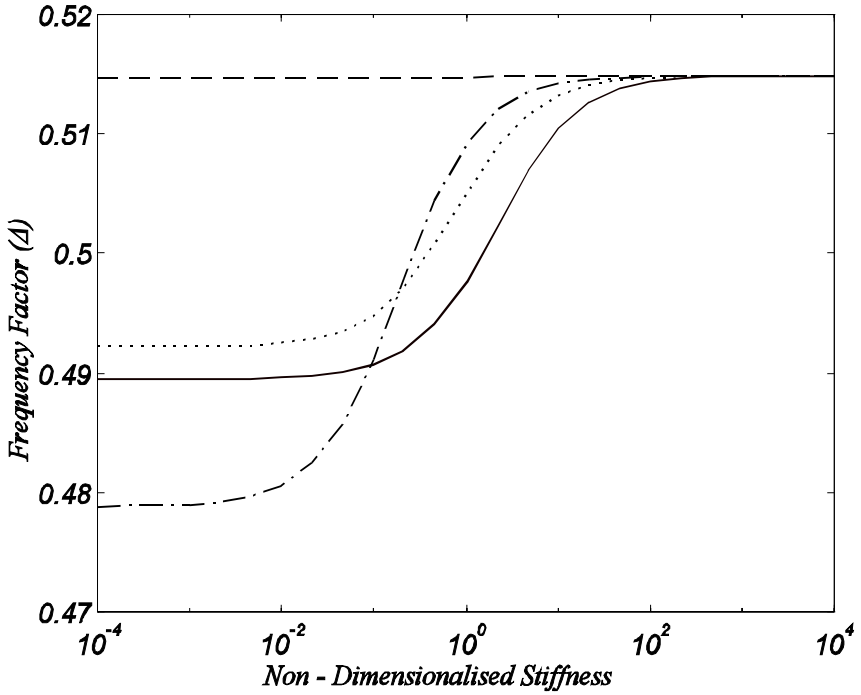

Figure 3.7 Influence of boundary stiffness on frequency factor of a steel cylinder supported at one end. ——, varying k_u^*; – – –, varying k_v^*; – · – · –, varying k_w^*; · · · ·, varying $k_{w'}^*$. (L/a = 1, h/a = 0.1, a = 6.25 mm, n = 4)

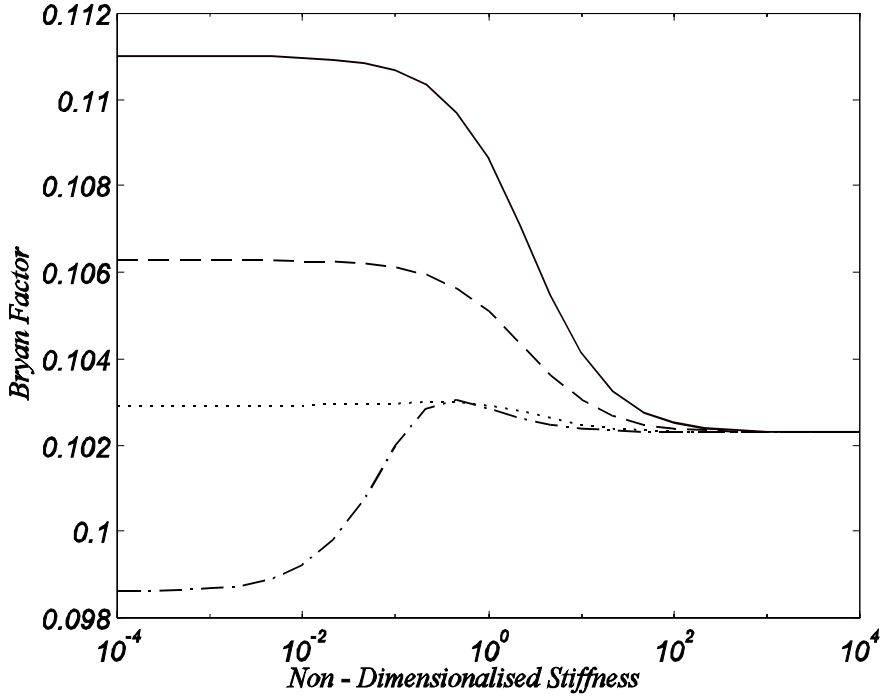

Figure 3.8 Influence of boundary stiffness on Bryan Factor of a steel cylinder supported at both ends. ——, varying k_u^*; – – –, varying k_v^*; – · – · –, varying k_w^*; · · · ·, varying $k_w'^*$. (L/a = 1, h/a = 0.05, a = 6.25 mm, n = 4)

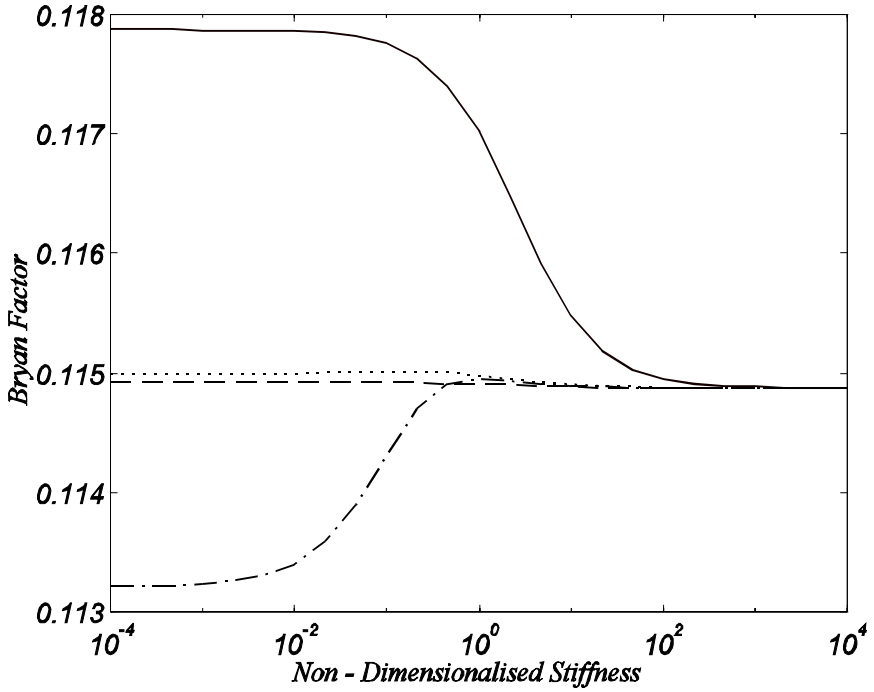

Figure 3.9 Influence of boundary stiffness on Bryan Factor of a steel cylinder supported at one end. ——, varying k_u^*; – – –, varying k_v^*; – · – · –, varying k_w^*; · · · ·, varying $k_{w'}^*$. (L/a = 1, h/a = 0.1, a = 6.25 mm, n = 4)

A cylinder which is to be used in a vibratory gyroscope, is required to have a constant Bryan Factor in the presence of temperature changes. It is therefore desirable to design the cylinder and supporting means to ensure that the boundary stiffnesses are out of the sensitive range.

3.5 Conclusions

The free vibrations of elastically supported cylinders including gyroscopic effects may be calculated by the exact solution of the Flügge shell theory equations of motion. The accuracy of Flügge shell theory was confirmed for a non-rotating cylinder with simply supported boundary conditions, by comparison with an exact solution of the three-dimensional elasticity problem.

Departures from ideal clamped boundary conditions were investigated for a cylinder supported at both ends, and for a cylinder supported at one end only. The results for the lowest frequency n=2 vibration mode are applicable to the design of vibrating cylinder gyroscopes. The natural frequency of this mode was most sensitive to changes in the tangential stiffness of the boundaries when both ends were supported, and to changes in the axial stiffness of the boundary when only one end was supported. The Bryan Factor was decreased by increasing the tangential stiffness of the boundaries. In general the Bryan Factor is higher, and is also less sensitive to boundary stiffness variations when only one end is supported.

The results for the lowest frequency n=4 vibration mode indicate that these trends do not apply to all vibration modes. This makes it necessary to analyse all the modes of interest in a particular cylinder with elastic boundary conditions.

If the non-dimensionalized stiffnesses of the boundaries are in the range 10^{-2} to 10^{2} it is necessary to consider the boundaries to be elastic. Stiffnesses out of this range may be considered to be zero (free) or infinite (rigid). If the boundary conditions are designed to have stiffnesses out of this range the free vibration of the cylinder will be practically insensitive to small variations in the boundary stiffnesses.

Chapter Four

Feedback Control Effects on Resonator Dynamics

4.1 Introduction

In this chapter the use of feedback control to modify the dynamics of piezoelectric resonators is discussed. This research was published in September 1998 [48].

Mechanical imperfections occur during the manufacture of the resonators used in vibratory gyroscopes. These imperfections cause the two vibration modes to have slightly different natural frequencies and determine the location of the mode shapes with respect to the structure. The effect of these imperfections is usually minimized by a mechanical balancing procedure. This balancing procedure generally involves the removal or addition of small amounts of mass from certain locations on the resonator so that the difference between the two natural frequencies is reduced. This process is time consuming, expensive, and is very difficult to perform on small micromachined designs. As this process is performed once at a single temperature, changes in the dynamics of the resonator over time or with temperature will not be accounted for. Also some of these resonators operate in a partial vacuum but are balanced at atmospheric pressures. The evacuation process can effect the dynamics of the resonator causing an increase in the difference between the natural frequencies.

A novel method of adapting the resonator dynamics was used in the HRG [14] and later also applied in the micromachined ring gyroscope [49]. Electrostatic actuation and sensing was used in these resonators, and "electrical springs" were produced by applying DC voltages across the electrode gaps. The electrostatic force is proportional to the square of the gap distance, therefore a decrease in the gap size results in an increase in the electrostatic force and vice versa. Because the variations in gap size during operation are very small, the effect of the electrostatic field may be represented (to first order) as a negative linear spring. By adjusting the value of the DC voltage across the gap, the spring constant may be varied. These electrical springs were adjusted to minimize the effects of

manufacturing imperfections in the resonator structure.

It has been demonstrated in the literature that the natural frequencies of cantilever beam type structures containing piezoelectric actuators may be adjusted by feedback techniques [50,51]. In this chapter it is demonstrated that in the case of a gyroscope resonator with piezoelectric sensing and actuation, an "electrical spring" can be formed by using displacement feedback and an "electrical damper" can be formed by applying velocity feedback. The electrical springs can therefore be used to decrease the effect of manufacturing imperfections on the performance of a piezoelectric vibratory gyroscope. Large feedback gains would result in large signal amplitudes which are impractical. It is therefore desirable to be able to predict the gains required. A method of calculating the magnitude of the feedback gains required is presented. This method is applied to a cylindrical resonator with discrete piezoelectric actuator and sensor elements and the theoretical predictions are verified by measurement.

4.2 Analysis of the Effects of Feedback Control

In chapter 2 it was demonstrated that the equations of motion for a resonator, excited by piezoelectric actuators and sensed by piezoelectric sensors, may be derived by application of Hamilton's principle to the coupled electromechanical system and discretization by the Rayleigh-Ritz method. The set of equations, derived in this manner, has the form:

$$\begin{aligned} \boldsymbol{M}\ddot{\boldsymbol{r}} + \boldsymbol{K}\boldsymbol{r} - \boldsymbol{\Theta}\boldsymbol{v} &= \boldsymbol{B}_f \boldsymbol{f} \\ \boldsymbol{\Theta}^T\boldsymbol{r} + \boldsymbol{C}_p\mathbf{v} &= \boldsymbol{B}_q\boldsymbol{q} \end{aligned} \tag{4.1}$$

These two equations are referred to as the actuator equation and the sensor equation [32]. The sensor equation may be partitioned to separate the voltages at the actuation electrodes from the voltages at the sensing electrodes as follows:

$$\begin{bmatrix}\boldsymbol{\Theta}_d & \boldsymbol{\Theta}_s\end{bmatrix}^T\{\boldsymbol{r}\} + \begin{bmatrix}\boldsymbol{C}_{pdd} & \boldsymbol{C}_{pds} \\ \boldsymbol{C}_{psd} & \boldsymbol{C}_{pss}\end{bmatrix}\begin{Bmatrix}\mathbf{v}_d \\ \mathbf{v}_s\end{Bmatrix} = \boldsymbol{B}_q\begin{Bmatrix}\boldsymbol{q}_d \\ \mathbf{0}\end{Bmatrix} \tag{4.2}$$

This equation can be rearranged to give the sensed voltage as a function of the displacement and the applied voltage.

$$\mathbf{v}_s = -\boldsymbol{C}_{pss}^{-1}[\boldsymbol{\Theta}_s^T\boldsymbol{r} + \boldsymbol{C}_{psd}\mathbf{v}_d] \tag{4.3}$$

If we feed a combination of the sensed voltages back to the actuator ceramics this can be regarded as displacement feedback and can be represented as follows:

$$\begin{aligned}\mathbf{v}_d &= \boldsymbol{G}_d\mathbf{v}_s \\ &= -\boldsymbol{G}_d\boldsymbol{C}_{pss}^{-1}\boldsymbol{\Theta}_s^T\boldsymbol{r} - \boldsymbol{G}_d\boldsymbol{C}_{pss}^{-1}\boldsymbol{C}_{psd}\mathbf{v}_d \\ &= -[\boldsymbol{I} + \boldsymbol{G}_d\boldsymbol{C}_{pss}^{-1}\boldsymbol{C}_{psd}]^{-1}\boldsymbol{G}_d\boldsymbol{C}_{pss}^{-1}\boldsymbol{\Theta}_s^T\boldsymbol{r}\end{aligned} \tag{4.4}$$

where, $\boldsymbol{I}$ is the identity matrix and $\boldsymbol{G}_d$ is a matrix of displacement feedback gains. The sensed voltage can then be written as:

$$\mathbf{v}_s = -\boldsymbol{C}_{pss}^{-1}[\boldsymbol{\Theta}_s^T - \boldsymbol{C}_{psd}[\boldsymbol{I} + \boldsymbol{G}_d\boldsymbol{C}_{pss}^{-1}\boldsymbol{C}_{psd}]^{-1}\boldsymbol{G}_d\boldsymbol{C}_{pss}^{-1}\boldsymbol{\Theta}_s^T]\boldsymbol{r} \tag{4.5}$$

Substituting the actuation and sensing voltages from equations 4.4 and 4.5 into the actuator equation yields the undamped equations of motion for the system including displacement feedback:

$$\boldsymbol{M}\ddot{\boldsymbol{r}} + \boldsymbol{K}^*\boldsymbol{r} = \mathbf{0} \tag{4.6}$$

where

$$\begin{aligned}\boldsymbol{K}^* = \boldsymbol{K} &+ \boldsymbol{\Theta}_d[\boldsymbol{I} + \boldsymbol{G}_d\boldsymbol{C}_{pss}^{-1}\boldsymbol{C}_{psd}]^{-1}\boldsymbol{G}_d\boldsymbol{C}_{pss}^{-1}\boldsymbol{\Theta}_s^T \\ &+ \boldsymbol{\Theta}_s\boldsymbol{C}_{pss}^{-1}[\boldsymbol{\Theta}_s^T - \boldsymbol{C}_{psd}[\boldsymbol{I} + \boldsymbol{G}_d\boldsymbol{C}_{pss}^{-1}\boldsymbol{C}_{psd}]^{-1}\boldsymbol{G}_d\boldsymbol{C}_{pss}^{-1}\boldsymbol{\Theta}_s^T]\end{aligned} \tag{4.7}$$

Equation 4.7 shows that the effective stiffness of the system can be altered by feeding back signals which are proportional to the displacement of the structure. An "electrical spring" has therefore been constructed by using feedback control.

If there is no capacitive coupling between the actuation and sensing ceramic electrodes ($\boldsymbol{C}_{psd} = \mathbf{0}$) the equations of motion simplify to:

$$\boldsymbol{M}\ddot{\boldsymbol{r}} + [\boldsymbol{K} + \boldsymbol{\Theta}_d \boldsymbol{G}_d \boldsymbol{C}_{pss}^{-1} \boldsymbol{\Theta}_s^T + \boldsymbol{\Theta}_s \boldsymbol{C}_{pss}^{-1} \boldsymbol{\Theta}_s^T]\boldsymbol{r} = \mathbf{0} \tag{4.8}$$

Equation 4.8 shows that leaving the sensing ceramics with open circuit (or high impedance) boundary conditions and feeding back signals from the sensing ceramics to the actuation ceramics, both contribute to the effective stiffness of the structure. Calculating the eigenvalues of this system for different feedback gains, provides a method of determining the influence of the displacement feedback gains on the natural frequencies of the resonator.

If velocity feedback is included, the voltage applied to the actuation ceramics may be expressed as:

$$\mathbf{v}_d = \boldsymbol{G}_d \mathbf{v}_s + \boldsymbol{G}_v \dot{\mathbf{v}} \tag{4.9}$$

where $\boldsymbol{G}_v$ is a matrix of velocity feedback gains.

Including an arbitrary viscous damping matrix ($\boldsymbol{C}$) and again omitting capacitive coupling between the sensing and actuation ceramics yields the following equations of motion:

$$\boldsymbol{M}\ddot{\boldsymbol{r}} + [\boldsymbol{C} + \boldsymbol{\Theta}_d \boldsymbol{G}_v \boldsymbol{C}_{pss}^{-1} \boldsymbol{\Theta}_s^T]\dot{\boldsymbol{r}} + [\boldsymbol{K} + \boldsymbol{\Theta}_d \boldsymbol{G}_d \boldsymbol{C}_{pss}^{-1} \boldsymbol{\Theta}_s^T + \boldsymbol{\Theta}_s \boldsymbol{C}_{pss}^{-1} \boldsymbol{\Theta}_s^T]\boldsymbol{r} = \mathbf{0} \tag{4.10}$$

From this equation it is seen that the effect of velocity feedback is to modify the damping characteristics of the system. It is therefore possible to construct an “electrical damper” by feeding back a signal proportional to the velocity of the structure. The natural frequencies and damping factors of this system may be calculated by transforming the equations of motion to state space and then calculating the eigenvalues.

4.3 Experimental Procedure

The feasibility of using feedback techniques to modify the dynamics of a piezoelectric vibratory gyroscope resonator was tested for the case of a vibrating cylinder resonator. This particular resonator comprises a thin-walled, steel cylinder, closed at one end, with eight discrete piezoelectric ceramics (PZT5A) bonded near the open end. The resonator is shown schematically in Fig. 2.1 and dimensions are given in Fig. 2.2.

The radial displacement patterns of the two operational modes of vibration are shown in Fig. 1.1 as viewed from the open end of the cylinder. During operation the primary mode is excited to oscillate at the resonant frequency (approximately 14500 Hz) at a constant amplitude. When a rotation is applied about the axis of the cylinder, energy is coupled from the primary mode into the secondary mode and the vibrating pattern appears to shift relative to the cylinder. The vibration of the secondary mode may be suppressed by actively damping the structure in order to increase the bandwidth of the gyroscope. In a perfect resonator the primary and secondary mode would have identical natural frequencies. Imperfections which occur during manufacture however, cause a difference in natural frequency, and also locate the mode shapes relative to the structure [29].

The experimental set-up selected to demonstrate the use of feedback to modify the dynamics of the resonator is shown in Fig. 4.1. A HP 3562A dynamic signal analyzer was used to measure the frequency response of the resonator by applying random noise excitation and measuring the response over a 100 Hz frequency range. The resonant frequency and the Q factor of the primary mode of vibration were then extracted from the measured frequency response function. The feedback gain and phase were varied so that displacement and velocity feedback could be investigated.

4.4 Results and Discussion

The procedure for obtaining the coupled equations of motion for the vibrating cylinder resonator was applied to the resonator as described in chapter 2. In chapter 2 the resonator cylinder was assumed to have a clamped boundary condition at the closed end

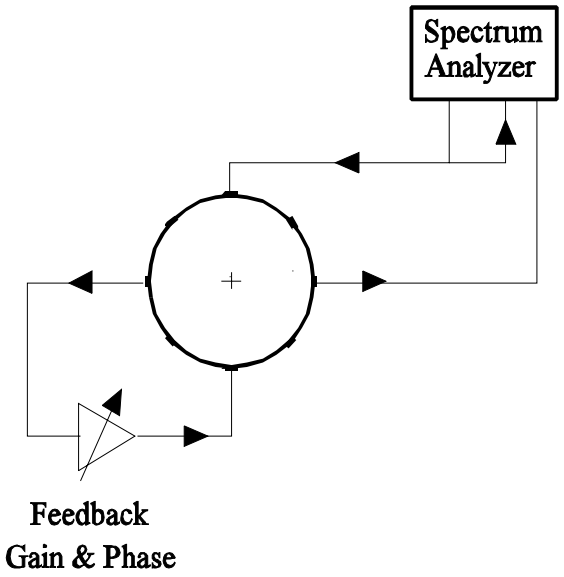

Figure 4.1 Experimental set-up used to measure the effect of feedback control on the resonator dynamics.

of the cylinder. This assumption resulted in the model over-predicting the natural frequencies. The model was extended to include flexibility in this boundary condition, as described in chapter 3, thus making it possible to adjust the boundary condition until the correct natural frequencies are obtained.

The piezoelectric ceramics were soldered to the cylinder at a temperature of approximately 335 ^{o}C and then polarized at a temperature of 120 ^{o}C. The value of the piezoelectric coefficient (e_{31}) for the ceramics in this condition is not certain, so the response of the resonator at a frequency of 1 kHz was used to calibrate this parameter. It was found that decreasing this constant, by 15% from the catalogue value of -5.4 Coulomb/m^2 , gave good agreement at 1 kHz. The experiment described in section 4.3 was simulated using the theory presented in section 4.2. The predicted and measured effect of displacement feedback on the resonant frequency of the primary mode is shown in Fig. 4.2. The results indicate that by varying the feedback gain from -2 to 2, a change in the resonant frequency of approximately 10 Hz can be produced. This change in frequency is larger than the difference in frequency caused by manufacturing imperfections.

The slope of the curve is dependent on the square of the piezoelectric coupling coefficient of the piezoelectric ceramic material as this coefficient influences the magnitude of the sensed voltage (through matrix Θ_s) and the effect of the drive voltage (through matrix Θ_d).

Positive displacement feedback gains caused a decrease in the resonant frequency rather than an increase, as would be expected. This occurs because, for the mode of interest, there is a 180^{o} phase difference between the displacement of the structure at the sensing ceramic element and the displacement of the structure at the actuation ceramic.

If the feedback control loop was disconnected so that both the sensing and actuation ceramics had open circuit boundary conditions, the voltages generated at these ceramics due to displacement of the primary mode, would be equal in magnitude but would have opposite phase. This situation is identical to connecting the feedback control

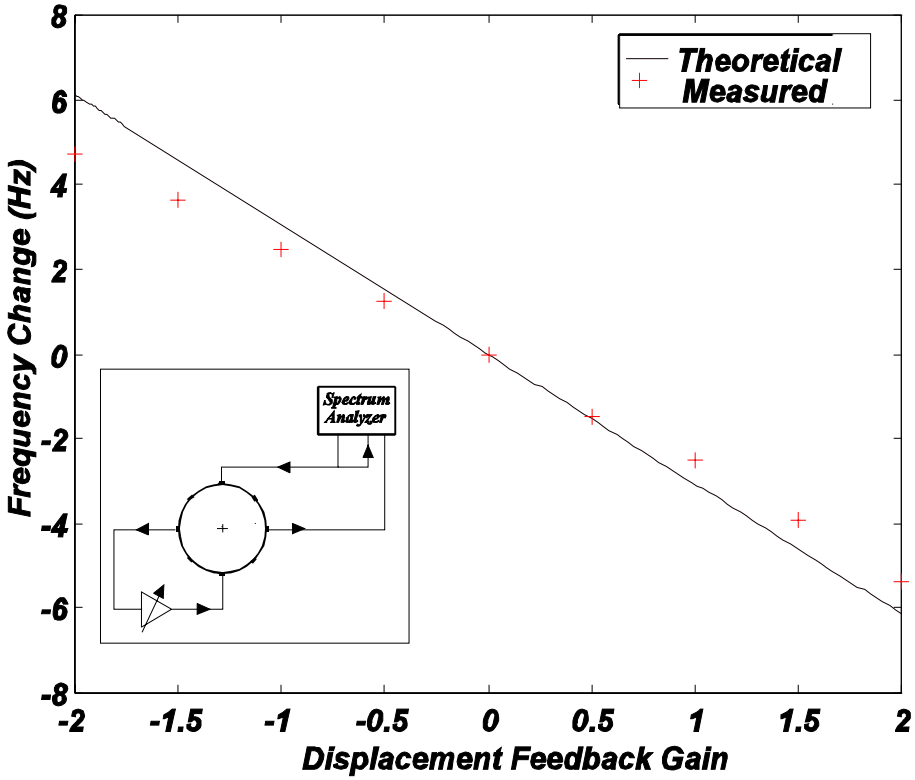

Figure 4.2 Resonant frequency change caused by displacement feedback demonstrating the concept of an “electrical spring”.

loop with a displacement feedback gain of -1, and would therefore be expected to cause the same change in resonant frequency. This experiment was performed and it was found that changing the electrical boundary condition of the actuation ceramic from closed circuit to open circuit increased the resonant frequency by 2.5 Hz. This is equal to the frequency shift that was obtained by applying a feedback with gain of -1 and is therefore a very simple method of experimentally determining the slope of this curve without performing any closed loop experiments.

The effect of velocity feedback is to modify the damping of the system. The damping of a resonator is usually quantified by the Q factor which is inversely related to the mechanical damping factor (ς) by the expression $Q = 1 / 2\varsigma$ [52]. Fig. 4.3 shows the effect of changing the velocity feedback gain on the Q factor of the resonator. The arbitrary viscous damping included in the model was adjusted to give agreement with the experimental values when no feedback was applied. Positive velocity feedback gains cause an increase in the Q factor (decrease in damping) because of the phase difference between the velocities of the sense and actuation ceramics. As the velocity feedback gain is increased, the total damping in the system tends towards zero, and the Q factor increases rapidly towards infinity. Increasing the velocity feedback gain further results in instability of the linear system. Applying a velocity feedback gain of -1 resulted in a change in Q factor from 3300 to 1500 which represents a modification in the mechanical damping factor from 0.00015 to 0.000334. Velocity feedback is commonly used to increase the bandwidth of vibratory gyroscopes and the method presented here can be used to determine the velocity feedback gain required for a particular bandwidth.

The difference between the theoretical and measured results can be almost completely eliminated by decreasing the piezoelectric coupling coefficient by a further 10 %. It appears that the method of calibrating this coefficient by using the response at 1 kHz has over-estimated this coefficient because the contribution of other vibration modes to the response at 1 kHz has not been included in the model.

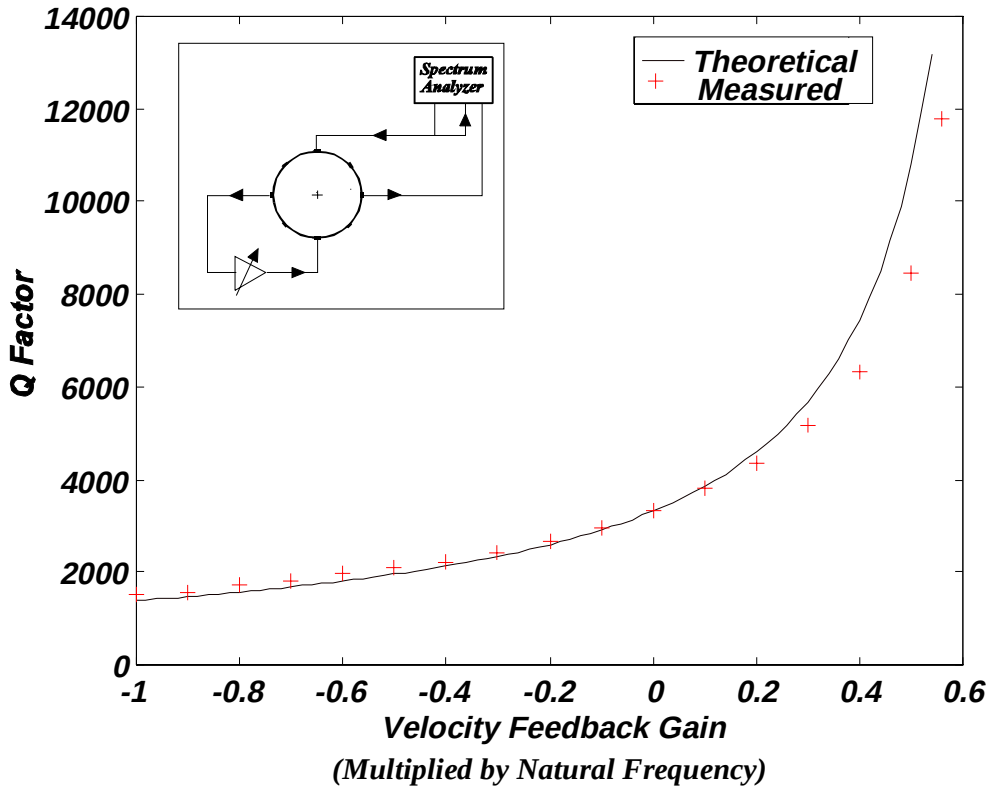

Figure 4.3 Q factor change caused by velocity feedback demonstrating the modification of the resonator damping properties.

4.5 Conclusions

A method has been presented for calculating the modification to the dynamic characteristics of a piezoelectric resonator which can be achieved by applying displacement and velocity feedback. It was shown that displacement feedback modifies the natural frequency while velocity feedback modifies the damping factor of the resonator. The method was applied to a vibrating cylinder resonator, with discrete sensing and actuation piezoelectric ceramics, and the calculated results agreed with experimental results thereby verifying the method. The cylindrical resonator considered here showed a change in resonant frequency of approximately 2.5 Hz per unit displacement feedback gain. This is sufficient for balancing of this type of resonator to be performed using displacement feedback instead of the conventional mechanical mass removal. It was also demonstrated that a simple experiment can be performed to determine the effect of displacement feedback on the natural frequency of a resonator without the use of any feedback electronics.

The “electrical spring” formed by displacement feedback could be adjusted continuously, to suppress the effects of anisoelasticity, as was done in the HRG using electrostatic “electrical springs”. This would however require the addition of a further eight piezoceramic elements positioned between the existing eight piezoceramic elements.

Chapter Five

Control System Design to Reduce The Effects of Imperfections

5.1 Introduction

In chapters 2 and 3 the resonator dynamics were considered and in chapter 4 the effects of feedback control on the resonator dynamics was analyzed. In this chapter the design and analysis of the control system for a vibratory gyroscope operating in rate sensor mode is described. Specific attention is given to the ability of the control system to reduce the effects of resonator imperfections on the gyroscope output.

The design of the control systems, for vibratory gyroscopes, has not been well documented in the literature. A good understanding of the effects of the control system on the performance of the gyroscope is required during the conceptual design of the resonator and control system.

Operation of a resonator as a rotation rate sensor generally requires that one vibration mode of the resonator is excited at resonance. When the resonator is rotated, energy is coupled from this mode into a second vibration mode. This Coriolis coupling causes a response in the second vibration mode which is used to measure the applied rotation rate. The response of this second mode is often controlled by a form of feedback control. This control is usually motivated by the need to increase the bandwidth of the gyroscope.

The performance of vibratory gyroscopes is limited by the effects of imperfections, in the resonator, which may be dependent on both time and temperature. The effects of imperfections in vibratory gyroscopes operating as rotation angle sensors were studied by Quick [3], Friedland and Hutton [28] and Loper and Lynch [14]. The effects of imperfections during operation as rotation rate sensors were investigated by Fox [29,30], Shatalov and Loveday [31] and Loveday [32]. These studies concentrated on the effects of imperfections on the resonator dynamics and did not consider the design of the control system specifically to reduce the effects of imperfections. In this chapter the ability of the

control system to suppress the effects of resonator imperfections is demonstrated.

The time averaged equations of motion for a general resonator with mass/stiffness and damping imperfections are derived in the most natural form for analysis of angular rate sensor operation. These equations are used to motivate the control functions required for operation as an angular rate sensor. The effects of imperfections may be understood qualitatively from these equations. Two control schemes are investigated theoretically and experimentally to demonstrate the ability of the control systems to reduce the effects of imperfections.

5.2 General Model of Resonator Dynamics

The model of the resonator is required to describe the dynamics of the two modes of vibration and the Coriolis coupling between them. Such a model may be derived by the Rayleigh-Ritz method as in chapter 2 or can be obtained from a finite element analysis. Because we consider only linear behavior and the resonators used are generally very lightly damped the contributions of modes other than the operating modes may be ignored. A model of the resonator with a large number of degrees of freedom can therefore be reduced to a two degree of freedom model representing only the operating modes. Such a two degree of freedom model provides a very general starting point for analysis of the control system.

The equations of motion of a “generic vibratory gyro” resonator are presented in equation 5.1. This representation is very similar to that used by Lynch [53]. Mass and stiffness imperfections cause a frequency difference between the two modes and also locate the modes. In the model, the position of the lower frequency axis is specified and it is assumed that the two mode shapes are orthogonal. The damping of the resonator is described by two time constants representing an axis of minimum damping and an axis of maximum damping. The excitation of the resonator is described by two forces which may arise from any form of actuation.

$$\begin{aligned}
&\ddot{x} - 2nk\Omega\dot{y} + (\frac{2}{\tau} + \Delta(\frac{1}{\tau})\cos 2n\theta_\tau)\dot{x} + \Delta(\frac{1}{\tau})\sin 2n\theta_\tau\dot{y} \\
&+ (\omega^2 - \omega\Delta\omega\cos 2n\theta_\omega)x - \omega\Delta\omega\sin 2n\theta_\omega y = f_x \\
&\ddot{y} + 2nk\Omega\dot{x} + \Delta(\frac{1}{\tau})\sin 2n\theta_\tau\dot{x} + (\frac{2}{\tau} - \Delta(\frac{1}{\tau})\cos 2n\theta_\tau)\dot{y} \\
&- \omega\Delta\omega\sin 2n\theta_\omega x + (\omega^2 + \omega\Delta\omega\cos 2n\theta_\omega)y = f_y
\end{aligned} \tag{5.1}$$

This equation is the same as that presented by Lynch except that the factor *n* describing the number of circumferential waves has been included while the $\dot{\Omega}$ (angular acceleration) and Ω^2 (centrifugal acceleration) terms have been omitted.

The particular case of an axisymmetric shell resonator operating in the n=2 mode is shown in Fig. 5.1.

The equations of motion can be written in terms of the elements of a damping matrix and a “natural frequency” matrix to simplify the following manipulations.

$$\begin{aligned}
&\ddot{x} - g\Omega\dot{y} + c_{11}\dot{x} + c_{12}\dot{y} + k_{11}x + k_{12}y = f_x \\
&\ddot{y} + g\Omega\dot{x} + c_{21}\dot{x} + c_{22}\dot{y} + k_{21}x + k_{22}y = f_y
\end{aligned} \tag{5.2}$$

The equations of motion for the piezoelectric resonator, derived in chapter 2, can easily be reduced to the above form.

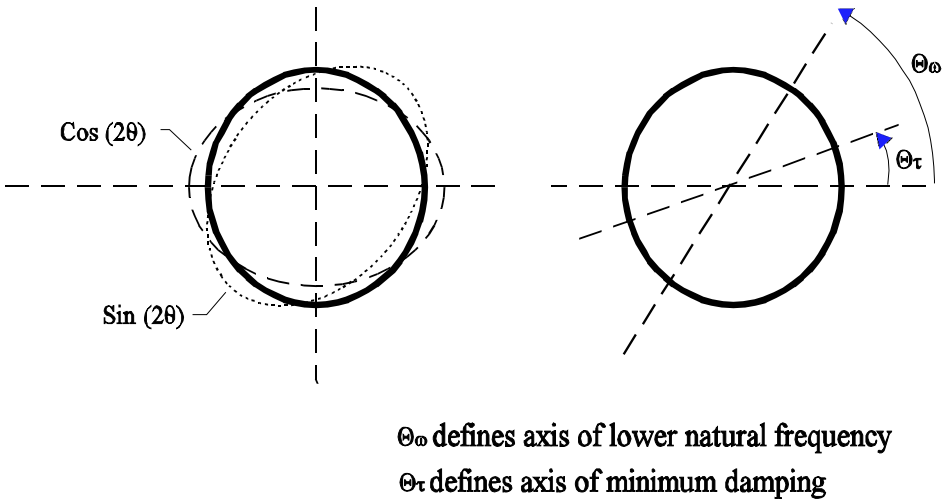

Figure 5.1 Vibration pattern representation and axis definitions used in the model.

5.3 Averaged Equations of Motion

Averaged equations of motion, describing the dynamics of a resonator including the effects of control loops, were derived by Lynch [53]. Canonical variables which are very suitable for describing the operation of the HRG as an angle sensor were used in these equations. In this section, averaged equations of motion in variables which are more suitable for the analysis of angular rate sensor operation are derived.

5.3.1 Variation of Parameters

The dynamics of the resonator may be more efficiently described by transforming the system of two second-order equations into a system of four first-order equations in slowly varying parameters. The equations of motion (equation 5.2), in the rapidly varying parameters x and y, may be transformed into equations in slowly varying parameters, X_s, X_c, Y_s and Y_c , by the following transformation:

$$\begin{aligned} x &= X_s \sin\nu t + X_c \cos\nu t \\ y &= Y_s \sin\nu t + Y_c \cos\nu t \end{aligned} \tag{5.3}$$

Differentiation of these two equations, with respect to time, yields:

$$\begin{aligned} \dot{x} &= \nu(X_s \cos\nu t - X_c \sin\nu t) + \dot{X}_s \sin\nu t + \dot{X}_c \cos\nu t \\ \dot{y} &= \nu(Y_s \cos\nu t - Y_c \sin\nu t) + \dot{Y}_s \sin\nu t + \dot{Y}_c \cos\nu t \end{aligned} \tag{5.4}$$

Because we have transformed the equations from two parameters to four parameters we can introduce two restrictions in the new parameters [54]. The following choice of restrictions is very advantageous:

$$\begin{aligned} \dot{X}_s \sin\nu t + \dot{X}_c \cos\nu t &= 0 \\ \dot{Y}_s \sin\nu t + \dot{Y}_c \cos\nu t &= 0 \end{aligned} \tag{5.5}$$

With these restrictions the velocities and accelerations become:

$$\begin{aligned} \dot{x} &= \nu(X_s \cos\nu t - X_c \sin\nu t) \\ \dot{y} &= \nu(Y_s \cos\nu t - Y_c \sin\nu t) \end{aligned} \tag{5.6}$$

$$\begin{aligned} \ddot{x} &= -\nu^2(X_s \sin\nu t + X_c \cos\nu t) + \nu(\dot{X}_s \cos\nu t - \dot{X}_c \sin\nu t) \\ \ddot{y} &= -\nu^2(Y_s \sin\nu t + Y_c \cos\nu t) + \nu(\dot{Y}_s \cos\nu t - \dot{Y}_c \sin\nu t) \end{aligned} \tag{5.7}$$

The velocities and accelerations are substituted into the equations of motion to yield:

$$\begin{aligned} &(k_{11} - \nu^2)(X_s \sin\nu t + X_c \cos\nu t) + \nu(\dot{X}_s \cos\nu t - \dot{X}_c \sin\nu t) \\ &+ (c_{12} - g\Omega)\nu(Y_s \cos\nu t - Y_c \sin\nu t) + c_{11}\nu(X_s \cos\nu t - X_c \sin\nu t) \\ &+ k_{12}(Y_s \sin\nu t + Y_c \cos\nu t) = F_{x_s} \sin\nu t + F_{x_c} \cos\nu t \\ &(k_{22} - \nu^2)(Y_s \sin\nu t + Y_c \cos\nu t) + \nu(\dot{Y}_s \cos\nu t - \dot{Y}_c \sin\nu t) \\ &+ (c_{21} + g\Omega)\nu(X_s \cos\nu t - X_c \sin\nu t) + c_{22}\nu(Y_s \cos\nu t - Y_c \sin\nu t) \\ &+ k_{21}(X_s \sin\nu t + X_c \cos\nu t) = F_{y_s} \sin\nu t + F_{y_c} \cos\nu t \end{aligned} \tag{5.8}$$

The next step is to combine these equations with the restrictions in order to obtain four equations each containing only one time derivative term. The process is illustrated for the first equation.

Multiplication of the first equation of motion (equation 5.8) by $\frac{\cos\nu t}{\nu}$ and adding the first restriction (equation 5.5) multiplied by $\sin\nu t$ yields the following equation:

$$\dot{X}_s = -\frac{(k_{11}-\nu^2)}{\nu}(X_s \sin\nu t\cos\nu t + X_c\cos^2\nu t) - (c_{12}-g\Omega)(Y_s\cos^2\nu t - Y_c\sin\nu t\cos\nu t) - c_{11}(X_s\cos^2\nu t - X_c\sin\nu t\cos\nu t) - \frac{k_{12}}{\nu}(Y_s\sin\nu t\cos\nu t + Y_c\cos^2\nu t) + \frac{F_{x_s}}{\nu}\sin\nu t\cos\nu t + \frac{F_{x_c}}{\nu}\cos^2\nu t \quad (5.9)$$

Similar combinations of equations 5.5 and 5.8 yield equations for $\dot{X}_c, \dot{Y}_s$ and $\dot{Y}_c$.

5.3.2 Averaging

Equation 5.9 shows that if the resonator is lightly damped, has small imperfections, is operating close to resonance and is subjected to small control forces (relative to the operating frequency) the rate of change of X_s $(\dot{X}_s)$ will be small. The same conclusion can be drawn for $\dot{X}_c, \dot{Y}_s$ and $\dot{Y}_c$. We can therefore assume that X_s, X_c, Y_s and Y_c are constant over one period of oscillation. This permits us to average the equations over one period of oscillation by applying the following expressions:

$$\frac{1}{T}\int_0^T \sin\nu t\cos\nu t\, dt = 0$$
$$\frac{1}{T}\int_0^T \cos^2\nu t\, dt = \frac{1}{T}\int_0^T \sin^2\nu t\, dt = \frac{1}{2} \quad (5.10)$$

The resulting averaged equation, corresponding to equation 5.9 is then,

$$\dot{X}_s = -\frac{c_{11}}{2}X_s - \frac{(k_{11}-\nu^2)}{2\nu}X_c - \frac{(c_{12}-g\Omega)}{2}Y_s - \frac{k_{12}}{2\nu}Y_c + \frac{F_{x_c}}{2\nu} \quad (5.11)$$

A further three equations can be extracted in this manner giving the system of four first-order equations, shown in equation 5.12. These equations describe the dynamics of the resonator in the slowly varying parameters.

$$
\begin{aligned}
\dot{X}_s &= -\frac{c_{11}}{2}X_s - \frac{(k_{11}-\nu^2)}{2\nu}X_c - \frac{(c_{12}-g\Omega)}{2}Y_s - \frac{k_{12}}{2\nu}Y_c + \frac{F_{x_c}}{2\nu} \\
\dot{X}_c &= \frac{(k_{11}-\nu^2)}{2\nu}X_s - \frac{c_{11}}{2}X_c + \frac{k_{12}}{2\nu}Y_s - \frac{(c_{12}-g\Omega)}{2}Y_c - \frac{F_{x_s}}{2\nu} \\
\dot{Y}_s &= -\frac{(c_{21}+g\Omega)}{2}X_s - \frac{k_{21}}{2\nu}X_c - \frac{c_{22}}{2}Y_s - \frac{(k_{22}-\nu^2)}{2\nu}Y_c + \frac{F_{y_c}}{2\nu} \\
\dot{Y}_c &= \frac{k_{21}}{2\nu}X_s - \frac{(c_{21}+g\Omega)}{2}X_c + \frac{(k_{22}-\nu^2)}{2\nu}Y_s - \frac{c_{22}}{2}Y_c - \frac{F_{y_s}}{2\nu}
\end{aligned}
\tag{5.12}
$$

The form of this system of equations appears similar to state-space equations but these equations include frequency and the frequency squared terms which are not present in a state space system. This means that state space methods of analyzing and designing control systems cannot be applied to this system.

During operation the resonator is forced to vibrate at resonance at a constant amplitude. This limit cycle can only exist in a nonlinear system which makes analysis of the control system difficult. Because the averaged equations above are in the slowly varying parameters, it is possible to use time integration to simulate the operation of the closed loop system. The averaged equations also provide useful insights into the behavior of the resonator which aid in the control system design.

5.4 Control System Functions

In this section the averaged equations of motion are used to motivate the control system functions required for the resonator to operate as an angular rate sensor. The equations of motion without imperfections are used to develop the control functions and the implementation of these functions. The effects of resonator imperfections, on the performance of the controlled system, are then analyzed in section 5.6.

The averaged equations of motion are simplified by the omission of imperfections.

$$\begin{aligned}
\dot{X}_s &= -\frac{c}{2}X_s - \frac{(k-\nu^2)}{2\nu}X_c + \frac{g\Omega}{2}Y_s + \frac{F_{x_c}}{2\nu} \\
\dot{X}_c &= \frac{(k-\nu^2)}{2\nu}X_s - \frac{c}{2}X_c + \frac{g\Omega}{2}Y_c - \frac{F_{x_s}}{2\nu} \\
\dot{Y}_s &= -\frac{g\Omega}{2}X_s - \frac{c}{2}Y_s - \frac{(k-\nu^2)}{2\nu}Y_c + \frac{F_{y_c}}{2\nu} \\
\dot{Y}_c &= -\frac{g\Omega}{2}X_c + \frac{(k-\nu^2)}{2\nu}Y_s - \frac{c}{2}Y_c - \frac{F_{y_s}}{2\nu}
\end{aligned} \tag{5.13}$$

It is evident that in the perfect resonator the *x* and *y* vibration patterns are only coupled when an angular rotation rate, Ω, is applied. We make use of this effect when we use the resonator as an angular rotation sensor or gyroscope. In the ideal case the control functions may be separated into those operating on the primary vibration pattern and those operating on the secondary vibration pattern.

5.4.1 Control of the Primary Vibration Pattern

The equations of motion for the primary vibration pattern, in the absence of applied rotation rate are,

$$\begin{aligned}
\dot{X}_s &= -\frac{c}{2}X_s - \frac{(k-\nu^2)}{2\nu}X_c + \frac{F_{x_c}}{2\nu} \\
\dot{X}_c &= \frac{(k-\nu^2)}{2\nu}X_s - \frac{c}{2}X_c - \frac{F_{x_s}}{2\nu}
\end{aligned} \tag{5.14}$$

The steady state response of the system is found by setting the time derivative terms to zero.

5.4.1.1 Frequency Control

If we apply a sinusoidal excitation $f_x = \sin\nu t$, (F_{xs}=1 and F_{xc}=0) at the frequency $\nu = \sqrt{k_{11}}$ then the coupling between X_c and X_s is zero and the response will be

$X_c = -\frac{F_{x_s}}{\nu c_{11}}$, $X_s = 0$. In other words, if we excite the structure at resonance the response will be ninety degrees out of phase with the excitation. At frequencies of excitation other than the resonant frequency the equations are coupled and there will be sine and cosine response components. The damping, *c*, determines the amplitude of response at steady state and also the speed with which this amplitude changes. Note that in the first-order approximation, the presence of damping does not effect the resonant frequency. Neglecting this second-order effect is justified because vibratory gyroscope resonators are designed to have very small damping.

The observation that there is a sine component response to a sine excitation if the excitation frequency does not coincide with the resonant frequency of the resonator suggests a method of controlling the frequency of excitation to follow the resonant frequency of the resonator. The sine component of the response (X_s) can be used as the error signal in a phase locked loop which drives the resonator at resonance. This phase locked loop includes a sine wave generator or voltage controlled oscillator (VCO) which produces a sine wave, the frequency of which is determined by the voltage applied to the VCO. The sine wave is applied to the resonator and the response of the resonator is demodulated by the excitation sine to produce the amplitudes of the components which are in-phase (X_s) and in phase quadrature (X_c) to the excitation signal. This demodulation can be achieved by a lock-in amplifier (LIA) which is a laboratory instrument specifically designed for this task. The response component X_s which is in-phase with the excitation is used as an error signal which is filtered by a proportional-integral controller before being fed back to control the frequency of the excitation signal generated by the VCO. This implementation is shown in Fig. 5.2.

5.4.1.2 Amplitude Control

The amplitude of response of the primary vibration pattern, when excited at resonance, is determined by the amplitude of the excitation and the damping in the

resonator. The Coriolis forces experienced by the secondary vibration pattern are proportional to the sum of the velocity of vibration of the primary vibration pattern and the applied rotation rate. The second function of the control system is to maintain the amplitude of the vibration of the primary mode at a constant value. Because the frequency control loop ensures that X_s is zero, the amplitude of the primary mode is given by X_c which is available from the lock-in amplifier used in the frequency control loop. The difference between the actual amplitude of vibration and a set reference value forms the error signal. Once again a proportional-integral controller can be used to ensure that the steady-state error is zero. The output from the PI controller is multiplied by the excitation signal from the VCO to control the amplitude of the signal applied to excite the resonator and thus the amplitude of the response of the resonator. The implementation of amplitude control is illustrated in Fig. 5.3.

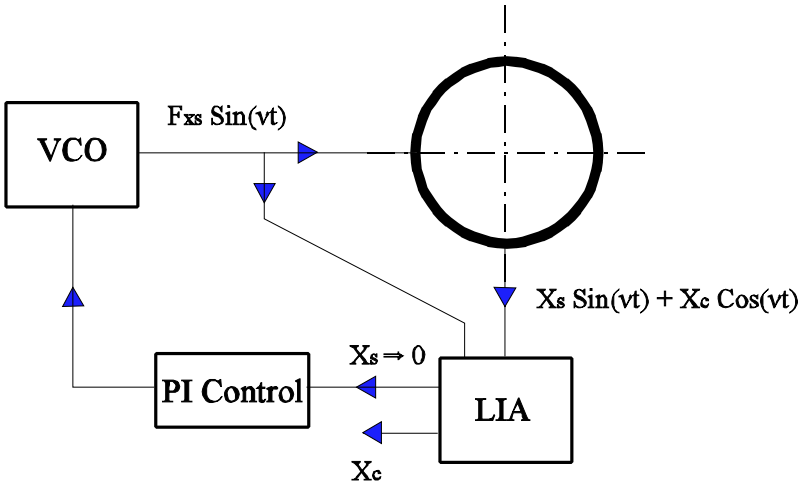

Figure 5.2 Frequency control of primary vibration pattern excitation by the phase locked loop approach.

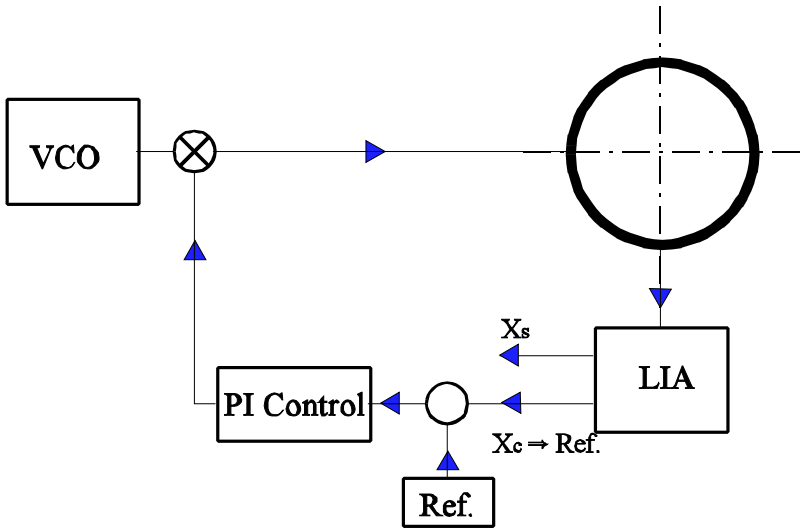

Figure 5.3 Amplitude control of primary vibration pattern.

5.4.2 Control of the Secondary Vibration Pattern

If we assume that the primary vibration pattern is excited to vibrate at resonance with constant amplitude ($X_s = 0$, $X_c = \bar{X}_c$) inspection of equation 5.13 shows that there will be a cosine response (Y_c) in the secondary vibration pattern when a constant rotation rate is applied. The response of the secondary vibration pattern to a step input angular rotation rate is easily calculated.

$$Y_{c_{step}} = -\frac{g\Omega\bar{X}_c}{c}(1-e^{-\frac{c}{2}t}) \tag{5.15}$$

This open loop response of the secondary vibration pattern gives the steady state amplitude which determines the scale factor of the gyroscope and also provides a measure of the response time. The open loop bandwidth of typical resonators is usually too small for most applications. The effective damping of the resonator (c) can be increased electronically by applying velocity feedback (see chapter 4). This option is described in the next section. It is also possible to null the response of the secondary vibration pattern by applying a suitable force F_s. The control system used to supply this force will then determine the response time or bandwidth of the gyroscope. This method of control is known as 'force to rebalance' because a force is applied which effectively balances the Coriolis force acting on the secondary vibration pattern. Force to rebalance operation is described in section 5.4.2.2.

5.4.2.1 Damping Control Loop

The averaged equations show that damping can be added to the secondary vibration pattern by applying F_{yc} proportional to $-Y_s$ and F_{ys} proportional to Y_c. This is essentially velocity feedback and is expressed mathematically as:

$$\begin{aligned} F_{y_c} &= -K_p Y_s \\ F_{y_s} &= K_p Y_c \end{aligned} \tag{5.16}$$

Velocity feedback can be implemented with a simple analogue differentiator but because the sensor and actuator are not collocated there is the possibility of higher frequency structural modes becoming unstable. Implementing the velocity feedback based on the phase-locked loop approach overcomes this problem because only signals at the operating frequency are applied to control the resonator. This implementation requires the use of a second lock-in amplifier to extract the components of the response of the secondary mode (Y_s and Y_c). These components are then multiplied by cosine and sine signals, available in the previous control loops, and fed back to the resonator. This implementation is shown schematically in Fig. 5.4.

The response to step input angular rotation (without elastic imperfections) is now:

$$Y_c = -\frac{g\Omega\bar{X}_c}{c+K_p/\nu}\left(1-e^{-\left(\frac{c}{2}+\frac{K_p}{2\nu}\right)t}\right) \tag{5.17}$$

The effect of the added damping is to increase the bandwidth of the gyroscope and to decrease the scale factor which will degrade the signal to noise ratio and decrease the resolution of the gyroscope.

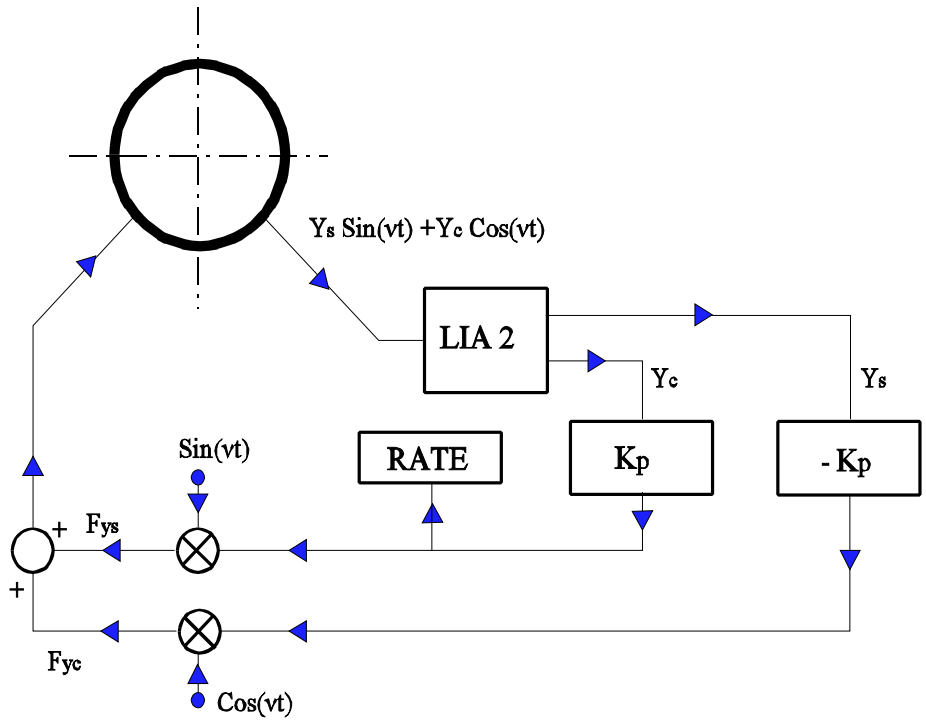

Figure 5.4 Implementation of the damping control loop under the phase locked loop approach.

5.4.2.2 Force to Rebalance (FTR) Control Loop

The response of the secondary vibration pattern Y_c, may be nulled by applying a suitable force F_{ys}. The bandwidth of the sensor is then determined by the controller used to null Y_c and the rotation rate information is stored in the signal F_{ys}, required to null the response. In this scheme the secondary mode is not allowed to respond and the Coriolis forces experienced by the secondary mode are balanced by the control force F_{ys}. This is true closed-loop operation.

When imperfections are present there will be a sine response in the secondary vibration pattern Y_s. Nulling the secondary vibration pattern requires that this component is also nulled. This case will be considered as we wish to later investigate the effects of imperfections on the gyroscope performance. The forces F_{ys} and F_{yc} required to null Y_c and Y_s respectively can be formed by two proportional-integral control systems as follows:

$$\begin{aligned} F_{y_c} &= -(K_P Y_s + K_I \int_0^t Y_s dt) \\ F_{y_s} &= K_p Y_c + K_I \int_0^t Y_c dt \end{aligned} \tag{5.18}$$

It is noted that the proportional part of the controller is exactly the same as the damping loop described earlier. Therefore this implementation of FTR is essentially a damping loop with the addition of integral control which nulls the steady state response of the secondary vibration pattern. The use of FTR means that the Coriolis forces acting on the secondary mode are balanced by the control forces and the position of the standing wave pattern is maintained fixed relative to the cylinder. The choice of feedback control coefficients determines the speed of response of the closed loop system and hence the bandwidth of the gyroscope. As there is no displacement or velocity of the secondary mode, changes in the damping factor c_{22} will also have no influence on the output. The damping anisotropy c_{12} will still have an effect on the output of the gyroscope and this will be the major source of error in the closed loop system. This implementation of a force to rebalance control system is illustrated in Fig. 5.5.

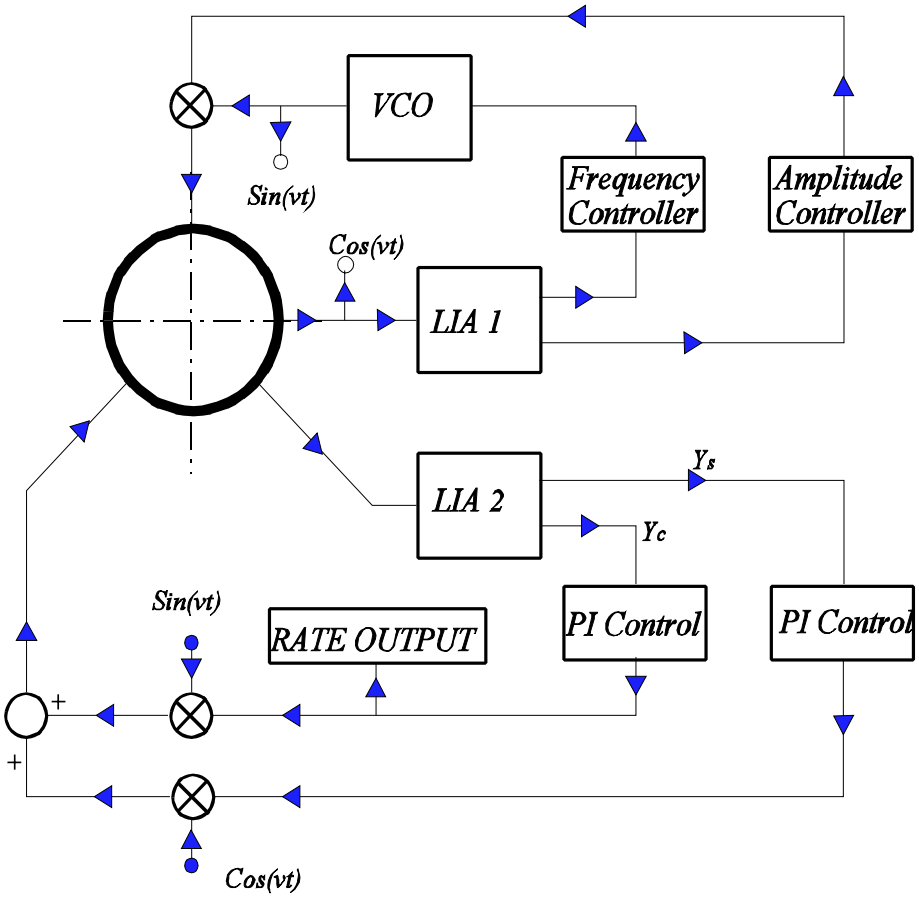

Figure 5.5 Force to rebalance control loop implementation shown with the primary mode control loops.

5.5 Closed Loop System Simulation

Simulation of the closed loop operation is necessary during the design of the control system. Predicting the transient behavior is important in applications requiring short start-up times. The following section describes how the transient response can be predicted numerically. Naturally the steady-state response can be predicted by performing the transient analysis over a long time period so that steady state operation is achieved. This, however, is inefficient and it is more informative to solve the averaged equations of motion with the constraints applied by the control system. The nonlinear equations can be solved numerically and in some cases qualitative predictions can be made. The effects of resonator imperfections on the steady-state performance are analyzed by this method in section 5.6.

5.5.1 Transient Analysis

Because the averaged equations of motion are in the slowly varying parameters, these equations and the control systems described in section 5.4 may be efficiently simulated by time integration. The gains associated with conversion of voltage to actuation force and from sensed voltage to generalized displacement must be included in the analysis. The equations of motion for the piezoelectric vibrating cylinder gyroscope, derived in chapter 2, where extended to include the effects of elastic boundaries. These equations were reduced to two degrees of freedom, averaged and simulated in Matlab Simulink. The Simulink model for the resonator operating with force to rebalance control is shown in Fig. 5.6. The voltage controlled oscillator (VCO) was assumed to have a free-running, or nominal frequency of 14.6 kHz. The frequency controller then modifies this frequency until resonance is achieved (sine component of primary mode is zero). The amplitude controller drives the cosine component of the primary mode to a fixed voltage level, in this case 1 Volt. The sine rebalance and cosine rebalance loops force the sine and cosine components, of the secondary mode, to zero. The magnitude of the signal required to force the cosine component of the secondary mode to zero provides a measure of the applied rotation rate. The start-up transient for this system, without rotation, is shown in Figs. 5.7 and 5.8. The frequency control loop is seen to settle on the resonant

frequency in approximately 0.6 s. As the frequency of excitation approaches resonance both the sine and cosine components of the response grow rapidly until the frequency is close to the resonance frequency when the sine component decreases towards zero. Once the frequency of excitation coincides with the resonant frequency the amplitude control loop has complete control over the amplitude and the desired level is achieved in approximately 1.2 s. Because there is no applied rotation and the resonator has no imperfections in this analysis, there is no response of the secondary mode. This response is not optimal in any sense, but serves to illustrate the operation and simulation of the control system in the time domain.

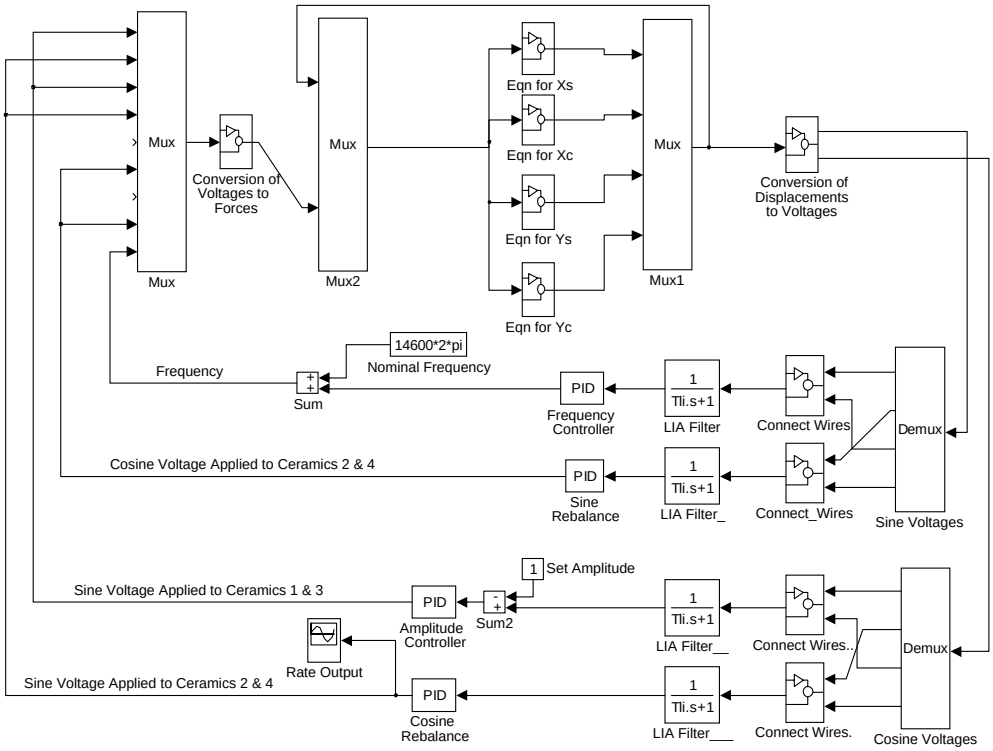

Figure 5.6 Simulink model of a resonator with FTR control.

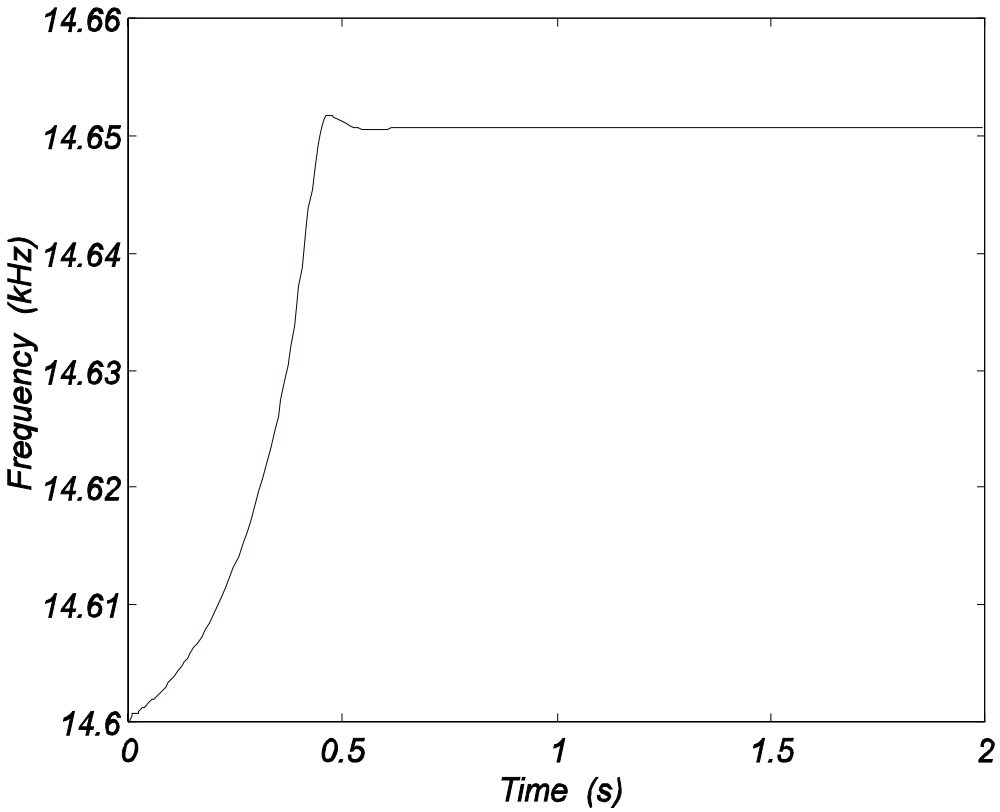

Figure 5.7 Frequency during simulated start-up transient showing the response of the frequency control loop.

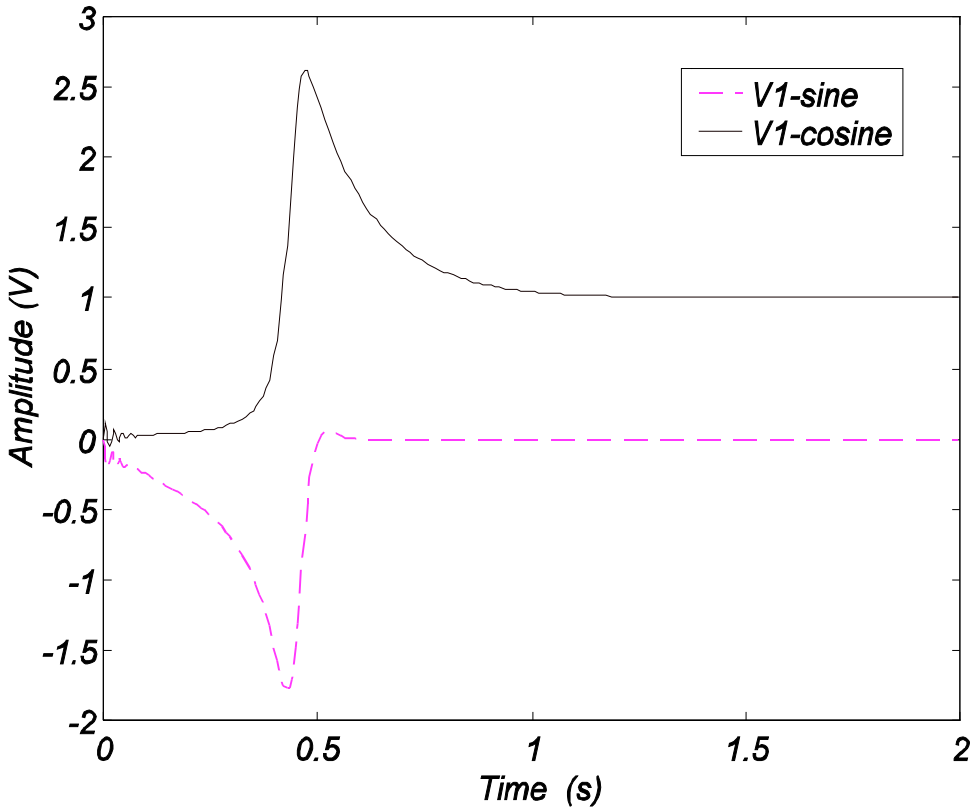

Figure 5.8 Primary mode sensed voltage during start-up transient showing the frequency control loop and then the amplitude control loop reaching steady state conditions.

5.5.2 Steady-State Analysis

In certain cases it is possible to directly calculate the steady state response of the controlled system but in general it was necessary to solve the nonlinear equations numerically. The control functions were expressed mathematically as different sets of conditions depending on the control functions being analyzed. For the primary mode this implies that $F_{x_c} = 0$; $X_s = 0$; $X_c = \overline{X_c}$ and we calculate the operating frequency ν and the required drive amplitude F_{xs}. The conditions applied to the secondary mode depend on the control loop selected. The prescribed conditions and the parameters to be calculated are summarized in table 5.1.

5.6 Analysis of the Effects of Imperfections

In section 5.4 the control system functions were described for a perfect resonator while the analysis of the closed loop operation was described in section 5.5. In this section the effects of imperfections, on the steady state performance of the gyroscope, are analyzed qualitatively, by inspection of the averaged equations of motion, and quantitatively, by numerical solution of the nonlinear equations. The effects of frequency and damping imperfections on the open loop performance are determined. The ability of the control loops to decrease this sensitivity to resonator imperfections is then considered.

Table 5.1 Conditions used during steady-state solutions.

Primary Mode Conditions		Secondary Mode Control	Secondary Mode Parameters	
Set	Calculate		Set	Calculate
$F_{x_c} = 0$ $X_s = 0$ $X_c = \overline{X_c}$	ν F_{x_s}	Open Loop	$F_{y_c} = F_{y_s} = 0$	$Y_s,\ Y_c$
		Damped	$F_{y_c} = -K_p Y_s$ $F_{y_s} = K_p Y_c$	$Y_s,\ Y_c$
		FTR	$Y_c = Y_s = 0$	$F_{y_s},\ F_{y_c}$

5.6.1 Open Loop Operation

5.6.1.1 Frequency Imperfections

The effect of frequency split (mass/stiffness anisotropy) was investigated. Elastic imperfections result in coupling between X_c and Y_s through k_{21} and then between Y_s and Y_c because $k_{22} \neq \nu^2$. The resulting response of Y_s and Y_c also couples back to the equations for X_s and X_c. Therefore elastic anisotropy results in a complex coupling between all four of the averaged equations of motion. The output of the gyroscope will therefore be sensitive to variations in the elasticity of the resonator.

A resonator with natural frequencies of 15000 Hz and 15001 Hz was simulated with the angular position of the lower frequency mode varied between 0° and 90°. The scale factor of the gyroscope was determined by introducing a rotation rate and observing the resultant Y_c. The zero-rate offset, due to the frequency imperfection, Y_c was then converted to a rotation rate in degrees/s and plotted in Fig. 5.9. It is noted that elastic imperfections do not cause a zero-rate offset if the axis of minimum natural frequency coincides with a ceramic location or is exactly between the ceramic locations.

5.6.1.2 Damping Imperfections

If we consider damping anisotropy we see that the terms $c_{12} = c_{21}$ appear with the Coriolis coupling terms. Therefore if the primary mode is excited so that X_c is constant then the term c_{21} causes a response in Y_c which appears as an applied rotation rate. This means that there will be a zero-rate offset that will be sensitive to changes in the damping distribution of the resonator. The zero-rate offset and response to a step input angular rate are now:

$$Y_c(\Omega = 0) = -\frac{c_{21}}{c_{22}} X_c$$

$$Y_{c_{step}} = -\frac{(c_{21} + g\Omega X_c)}{c_{22}}\left(1 - e^{-\frac{c_{22}}{2}t}\right) \tag{5.19}$$

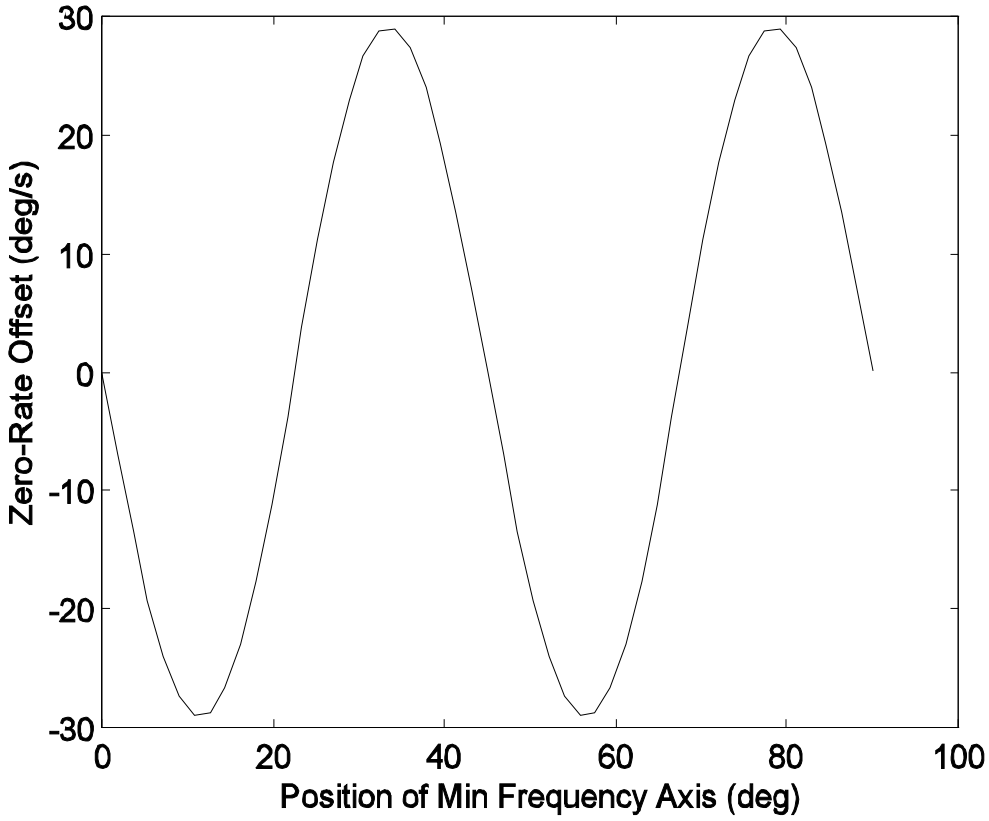

Figure 5.9 Zero-rate offset of a 15 kHz resonator with a 1 Hz frequency imperfection - open loop.

The effects of damping imperfections were investigated by introducing two typical damping time constants of 25 and 25.5 seconds. The maximum damping axis was rotated and the zero-rate offset calculated for the open loop case. The zero-rate offset is shown in Fig. 5.10. The result shows that if the axis of minimum damping coincides with either the primary or secondary mode of vibration, no zero-rate offset will result from this imperfection.

5.6.1.3 Combined Frequency and Damping Imperfections

Finally the effect of combined elastic and damping imperfections needs to be considered. The zero-rate offset, due to elastic and damping imperfections acting simultaneously, was calculated by solving the steady-state equations for different combinations of damping axis angle and frequency axis angle. This result is plotted as a surface in Fig. 5.11. The zero-rate offset obtained by adding the zero-rate offsets calculated when the imperfections act independently was calculated and was found to be a good approximation of the zero-rate offset due to the imperfections acting simultaneously. Also plotted in Fig. 5.11 is the error caused by this approximation. This error can be written symbolically as follows:

$$ERROR(\theta_\tau,\theta_\omega) = Drift(\theta_\tau,\theta_\omega) - (Drift(\theta_\tau) + Drift(\theta_\omega)) \qquad (5.20)$$

The effects of the small frequency and damping imperfections considered here are therefore almost independent of each other.

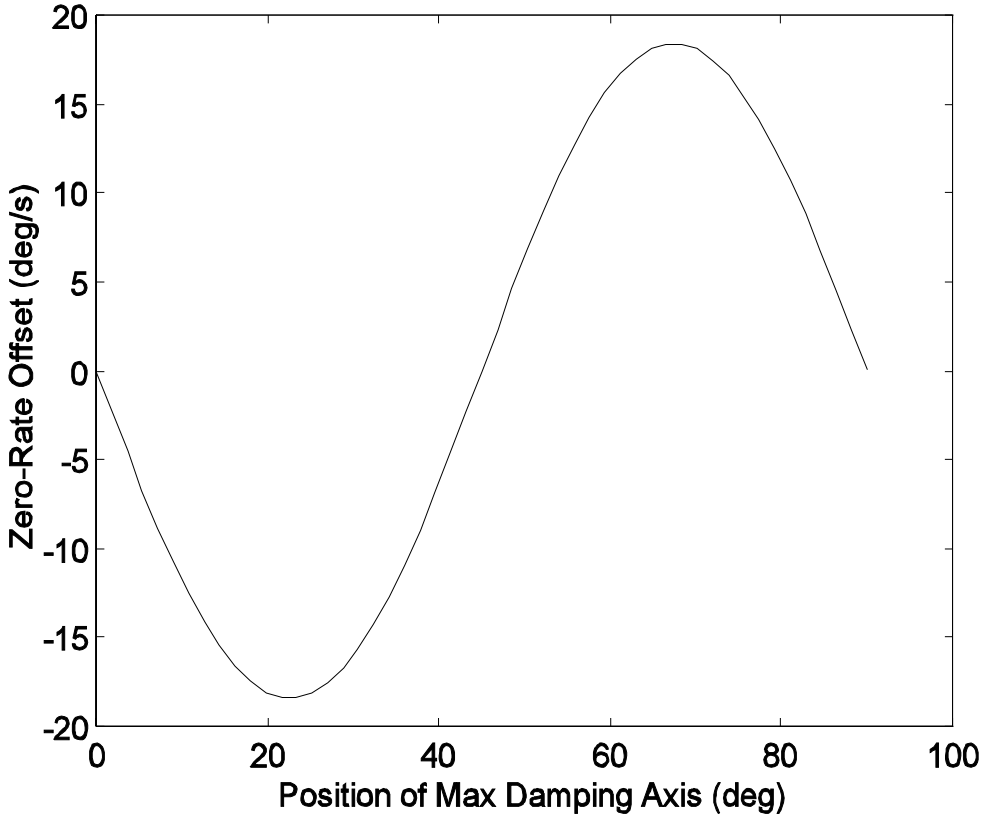

Figure 5.10 Zero-rate offset of a 15 kHz resonator with a damping imperfection defined by two time constants of 25 s and 25.5 s - open loop.

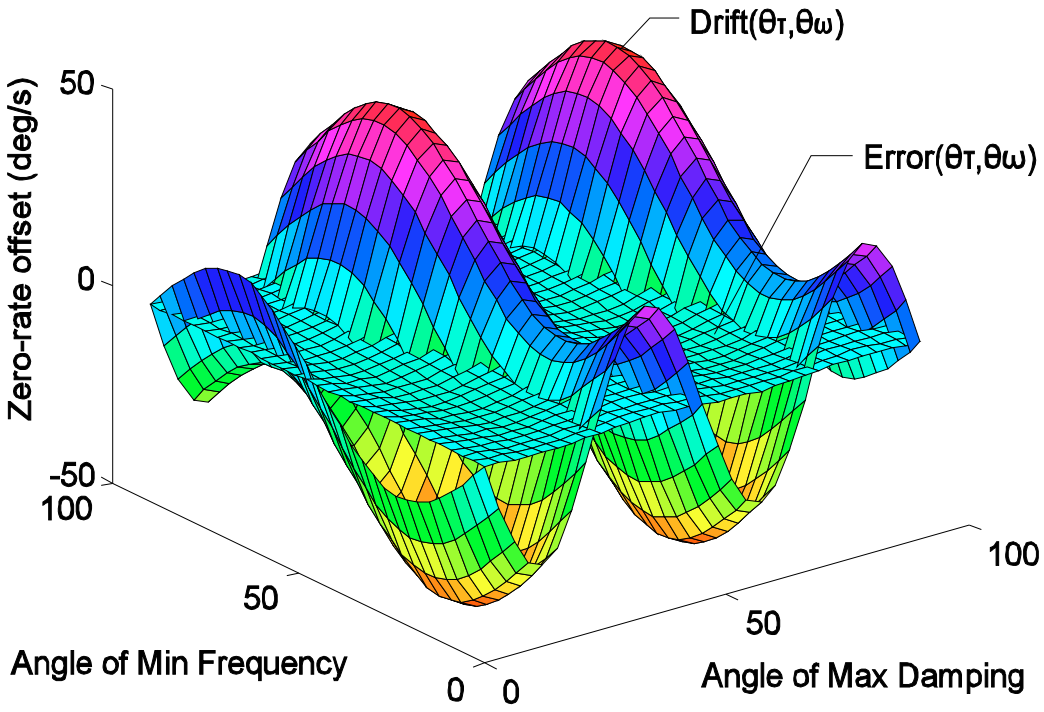

Figure 5.11 Calculated zero-rate offset due to the combined effect of frequency (15 kHz resonator with 1 Hz frequency split) and damping imperfections (time constants of 25 s and 25.5 s) - open loop.

5.6.2 Damping Loop Control

The effects of frequency and damping imperfections when damping loop control is applied, to the secondary vibration pattern, were investigated.

5.6.2.1 Frequency Imperfections

The same frequency imperfection as was considered in the open loop case was analyzed for different values of damping control. In this analysis the gain of the feedback loop is quantified by the amount of damping added to the resonator compared to the inherent damping of the resonator. The zero-rate offset (in degrees/s) was calculated for the open loop case and for three cases with increasing active damping. The results of this investigation are plotted in Fig. 5.12 and show that increasing the damping loop gain decreases the gyroscope drift from this source.

This effect can be understood qualitatively from the averaged equations of motion. If the damping of the secondary mode doubles the in-phase response (Y_s) of the secondary mode, due to the coupling of k_{12}, will be halved. The response of the quadrature component (Y_c) of the secondary mode due to the coupling $k_{22} - \nu^2$ will then be one quarter of the open loop case. The scale factor (sensitivity of Y_c to input angular rotations) will be halved by the addition of the damping therefore the zero-rate offset due to an elastic imperfection will be halved by the addition of the damping. As the damping is increased the zero-rate offset caused by elastic imperfections will decrease. This qualitative description does not consider the elastic coupling of the secondary mode response back to the primary mode which effects the frequency of operation slightly. A comparison of the qualitative description and the exact solution of the steady state equations is shown in Fig. 5.13 which shows the zero-rate offset due to a particular elastic imperfection as a function of the added damping.

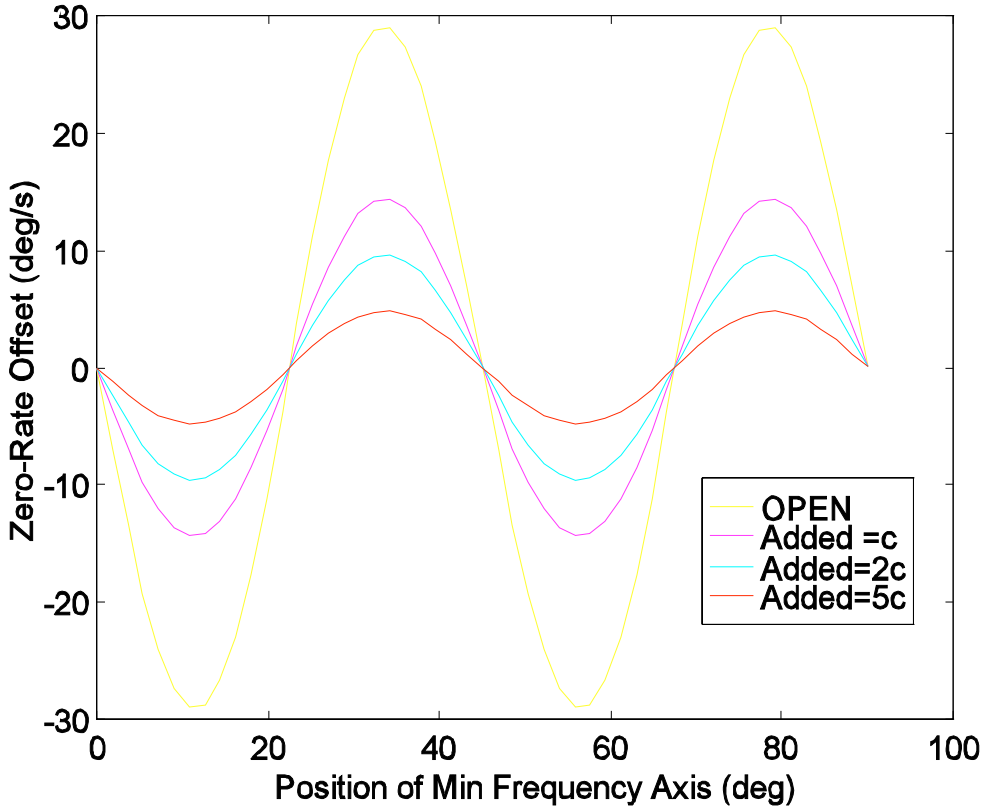

Figure 5.12 Reduction of zero-rate offset due to frequency imperfection (15 kHz resonator with 1 Hz frequency split) by damping loop control.

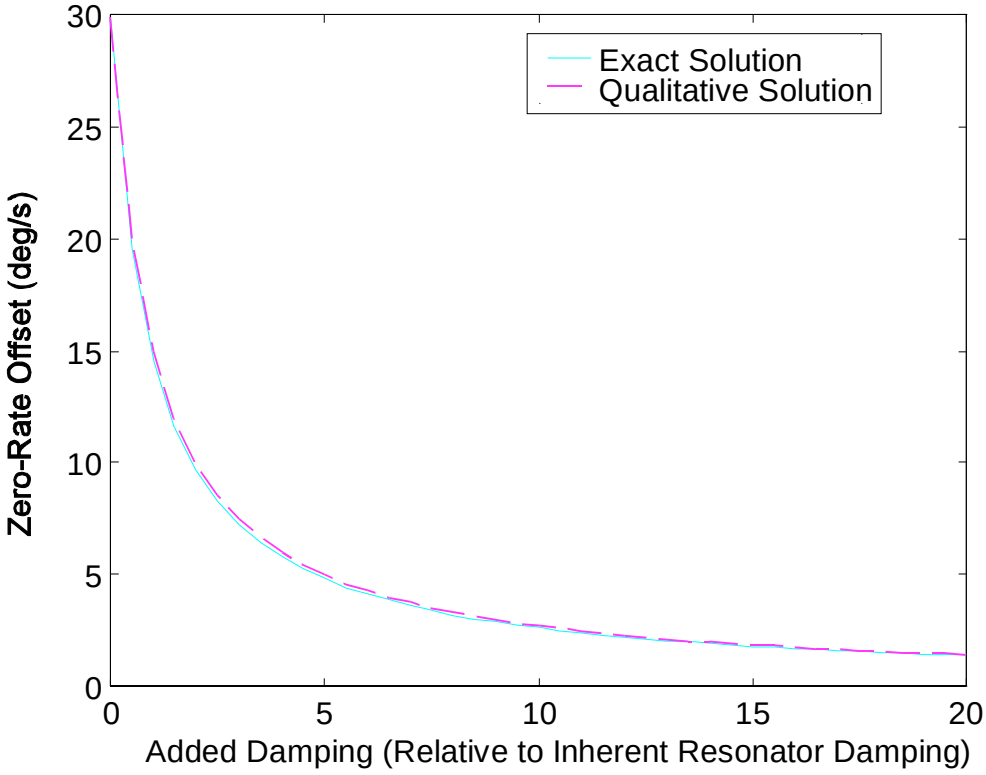

Figure 5.13 Effect of damping loop gain on zero-rate offset caused by frequency imperfections, verifying the qualitative explanation.

5.6.2.2 Damping Imperfections

The effect of damping imperfections were investigated by introducing the two damping time constants of 25 and 25.5 seconds. The maximum damping axis was rotated and the drift calculated for the open loop case and with a damping loop that adds ten times the resonator damping. The results of this analysis (Fig. 5.14) show that the drift caused by damping imperfections is not reduced by the addition of the damping control loop. The qualitative explanation of this is that the term c_{12} is not effected by the addition of damping and still appears as a equivalent rate input in equation 5.12.

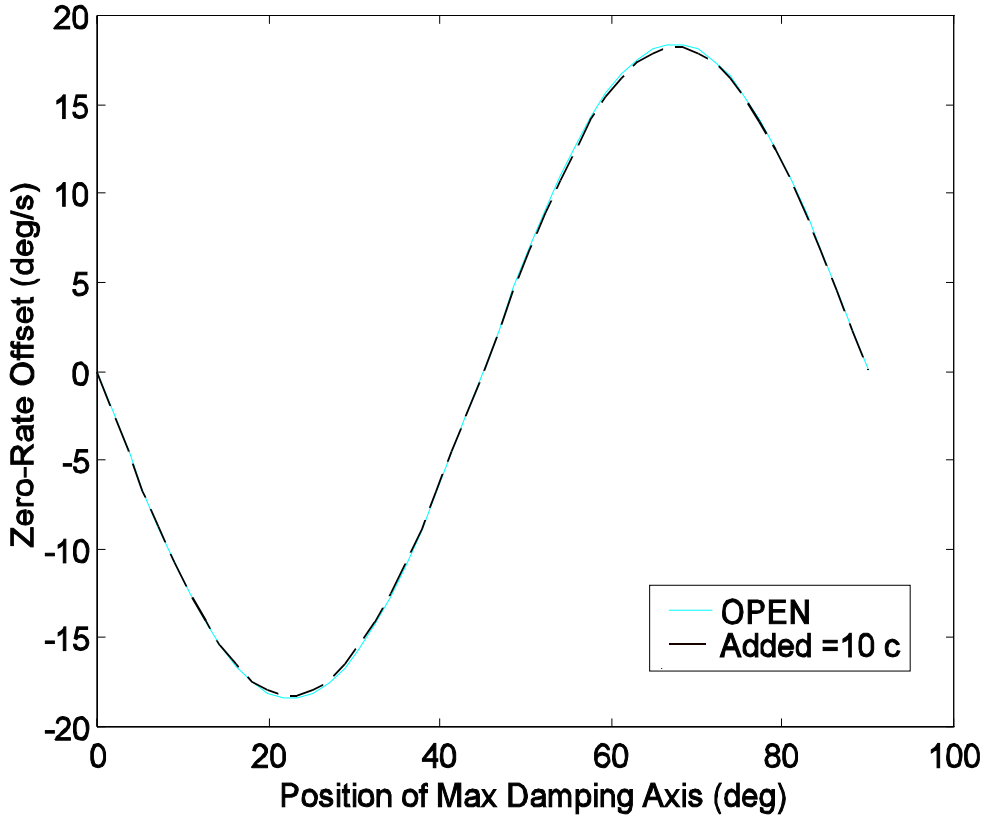

Figure 5.14 Zero-rate offset due to damping imperfections unaffected by damping loop control.

5.6.3 Force to Rebalance Control

The effect of using proportional-integral feedback to null the response of the secondary mode, when frequency and damping imperfections are present, was investigated by solving the steady-state equations. The effect of nulling the in-phase and quadrature components of the response separately and then simultaneously was considered to gain deeper insight into the effects of FTR control.

5.6.3.1 Frequency Imperfections

Inspection of the averaged equations shows that frequency imperfections affect the value of Y_c only if Y_s is non zero. Y_s is non-zero due to the term k_{21} coupling Y_s to X_c. Also, if Y_c is non zero it couples back to the equation for X_s and thus influences the frequency of operation. It is therefore advantageous to null the component Y_s to eliminate this coupling.

Figure 5.15 shows that nulling the in-phase component Y_s, eliminated the drift caused by elastic imperfections thus verifying the qualitative explanation given above. When only the quadrature component Y_c, is nulled the drift is not reduced from the open loop case. The reason for nulling the quadrature component is to increase the bandwidth of the gyroscope.

5.6.3.2 Damping Imperfections

The effect of damping imperfections was calculated in the analogous manner. Figure 5.16 shows that force to rebalance control does not reduce the drift caused by damping imperfections as represented in this analysis. Inspection of equation 5.12 shows that the damping imperfection is indistinguishable from an applied rotation.

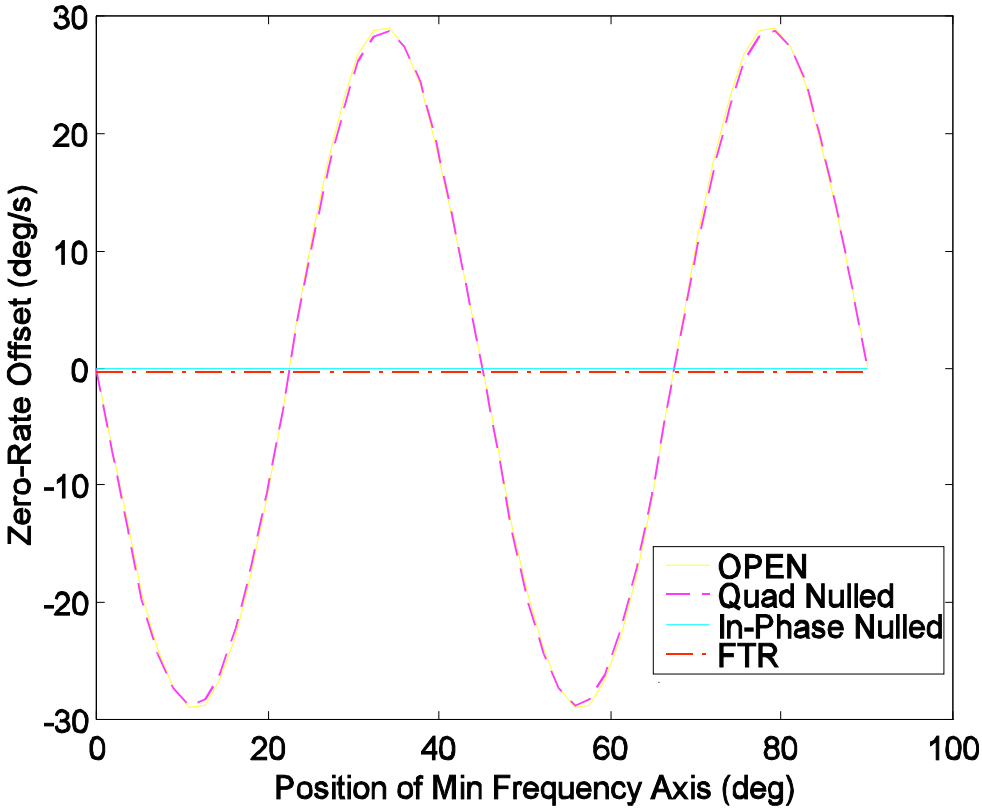

Figure 5.15 Suppression of the zero-rate offset due to frequency imperfections (15 kHz resonator with 1 Hz frequency split) by FTR control.

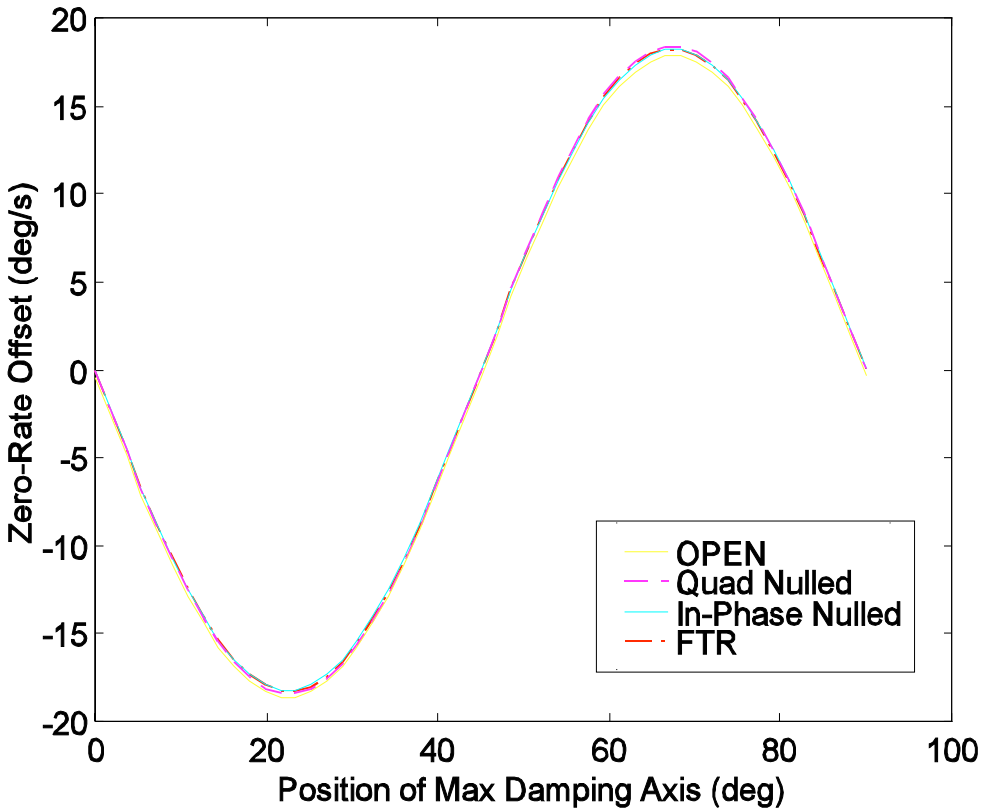

Figure 5.16 No reduction of the zero-rate offset due to damping imperfections by FTR control.

5.7 Experimental Investigation

The zero-rate offset of a vibratory gyroscope is an important performance parameter and is strongly influenced by temperature. The temperature induced variations, or drift, of this parameter, for a piezoelectrically sensed and actuated vibrating cylinder gyroscope were investigated experimentally. Damping loop and force to rebalance control were implemented and the results were compared to measurements with open loop control.

5.7.1 Experimental Setup

The resonator used in the experiments comprised a thin walled, steel cylinder, closed at one end, with eight discrete piezoelectric ceramic elements bonded near the open end as described in chapter 2. Opposite pairs of ceramic elements were electrically connected and two pairs functioned as actuators while the remaining two pairs functioned as sensors. The resonator was enclosed in an evacuated housing to reduce acoustic radiation damping.

The control systems described in section 5.4 were implemented using a combination of digital and analog circuitry. In these experiments the control system was kept at room temperature while the resonator (with pre-amplifiers) was placed in an environmental chamber on a rate table. The scale factor (mV/deg/s) of the gyroscope, with a particular control system, was measured at 20°C. The zero-rate offset of the gyroscope was then measured as a function of temperature over a range of 0 to 60°C using the temperature profile shown in Fig. 5.17. The measured voltage was then converted to an equivalent rotation rate in °/s using the measured scale factor. In this way it was possible to compare the variations in zero-rate offset of the gyroscope with different control systems. All measurements were conducted on the same resonator.

5.7.2 Experimental Results

5.7.2.1 Damping Loop Control

The amount of damping added to the resonator was measured by the reduction in scale factor that was obtained. The damping loop gain was varied from zero (open loop) to a value giving a large bandwidth. The measured zero-rate offsets are displayed, as functions of time, in Fig. 5.18 and as functions of temperature in Fig. 5.19. These zero-rate offsets were adjusted so that the minimum offset is zero in each case. This makes it easy to compare the variations of the offset over temperature. These figures clearly show the reduction in drift which results from increasing the damping of the secondary mode. In this particular resonator the drift was decreased by an order of magnitude.

The gains displayed in Figs. 5.18 and 5.19 are the ratios of the feedback voltage to the sensed voltage and not the ratio of force to displacement. The amount of added damping was estimated from the reduction in scale factor so that the maximum offset drift could be plotted against the added damping as was done in Fig. 5.13. The added damping is the damping added by the velocity feedback non-dimensionalized by dividing by the damping inherent in the resonator. This information is plotted in Fig. 5.20 and the experimental result is compared to the qualitative effect of adding damping. The theoretical curve assumes that there are no damping imperfections while the experimental results are obviously effected by damping imperfections inherent in the resonator. The correlation between the experimental and theoretical results is believed to be adequate to confirm the theoretical predictions. This result indicates that the major source of offset in the open loop operation, was the variation in frequency imperfection during the temperature cycle. Damping loop control produced an order of magnitude decrease in the temperature induced zero-rate offset drift.

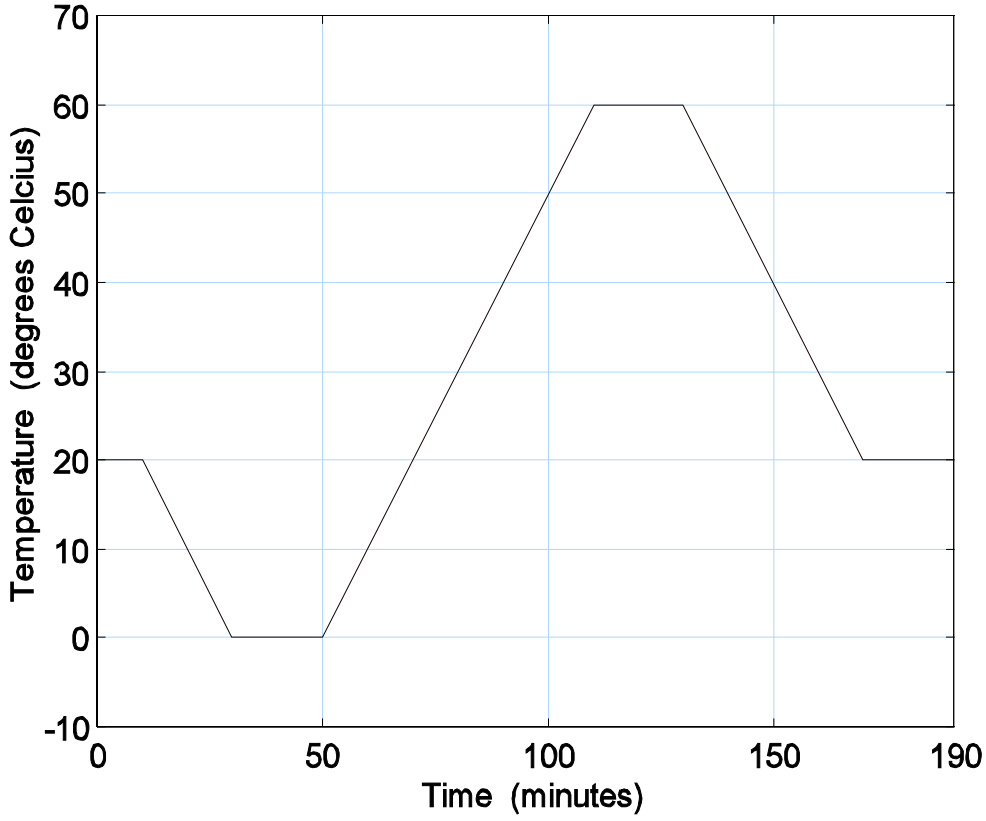

Figure 5.17 Temperature cycle applied to resonator during measurements.

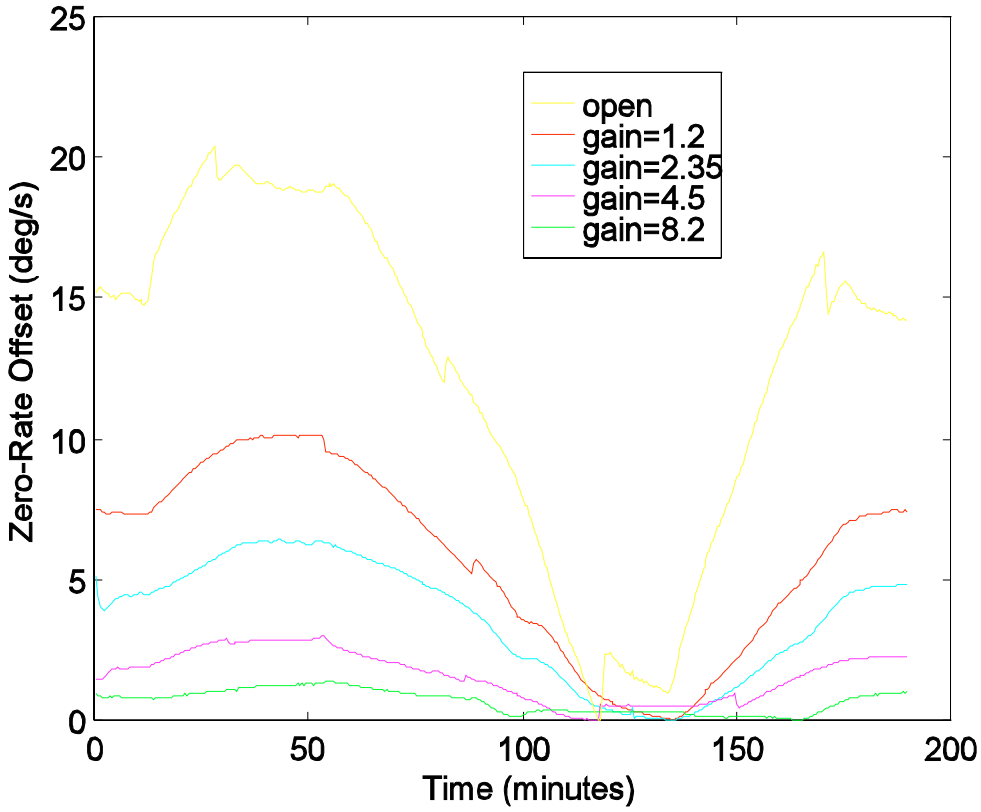

Figure 5.18 Measured reduction of temperature induced zero-rate offset drift by damping loop control (offset vs time).

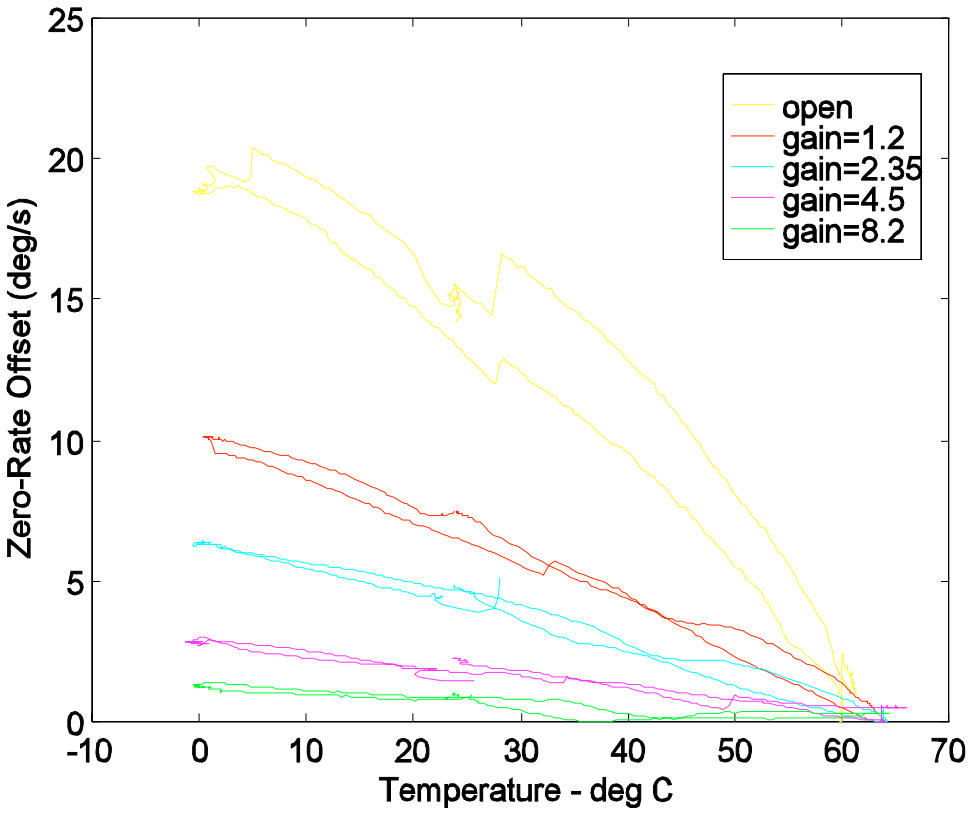

Figure 5.19 Measured reduction of temperature induced zero-rate offset drift by damping loop control (offset vs temperature).

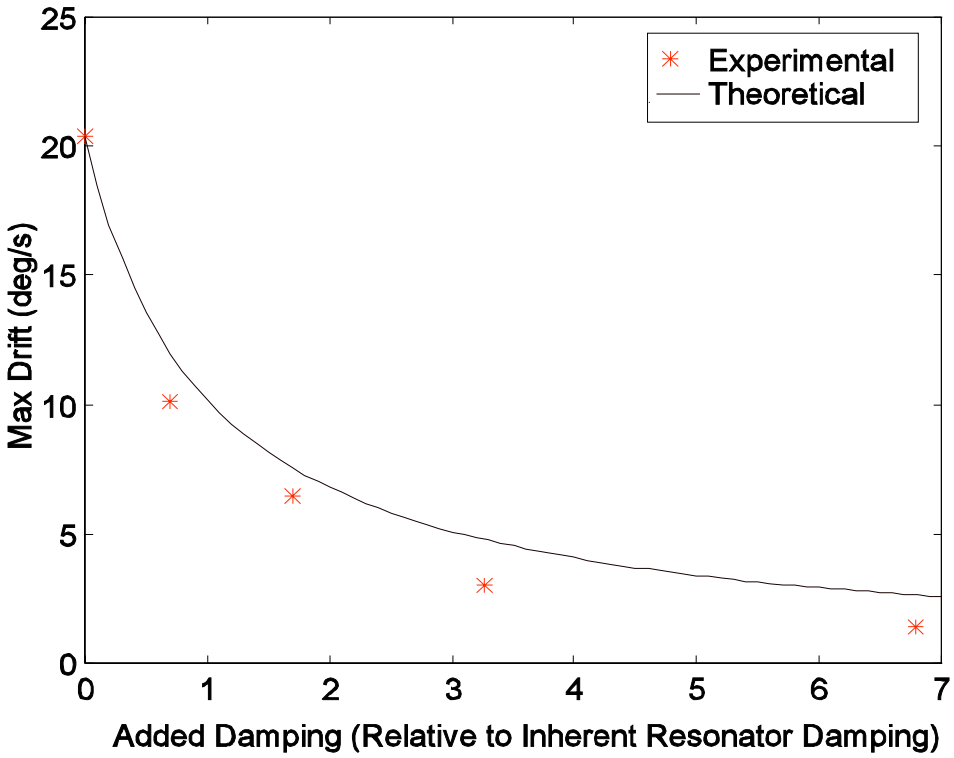

Figure 5.20 Zero-rate offset drift reduction by increasing damping loop gain.

5.7.2.2 Force to Rebalance Control

Measurements were performed to investigate the effect of force to rebalance control on the temperature induced zero-rate offset. The results of these measurements are shown in Figs. 5.21 and 5.22. Apart from the control system in which both components of the secondary mode response are nulled, control systems where only one component is nulled were also examined. The results show a dramatic decrease in the drift when the in-phase component of the secondary mode is nulled. This result is in agreement with the theory as by nulling the in-phase component the effects of elastic imperfections are suppressed. Force to rebalance control produced an order of magnitude decrease in the temperature induced zero-rate offset drift.

5.8 Conclusions

A system of averaged equations describing the dynamics of a vibratory gyroscope resonator were presented. These equations are very convenient for analysis of control systems used to operate the resonator as a rotation rate sensor. The equations prompt the form of control system required and also provide useful insight into the qualitative effects of the resonator imperfections. Two feedback control schemes were considered namely, damping loop control and force to rebalance control. The effects of frequency and damping imperfections were analyzed for open loop and closed loop operation. It was found that the control system can eliminate the first-order effects of frequency imperfections. The effect of damping anisotropy is not reduced by the control systems and this is believed to be the major source of error in the closed loop system. Experimental measurements, of a piezoelectrically actuated and sensed resonator, over a temperature range of 60 °C, showed that variation of the zero-rate offset was decreased by an order of magnitude by both damping loop control and force-to-rebalance control. The remaining drift is believed to be primarily due to damping imperfections. The experimental results verify the theoretical predictions.

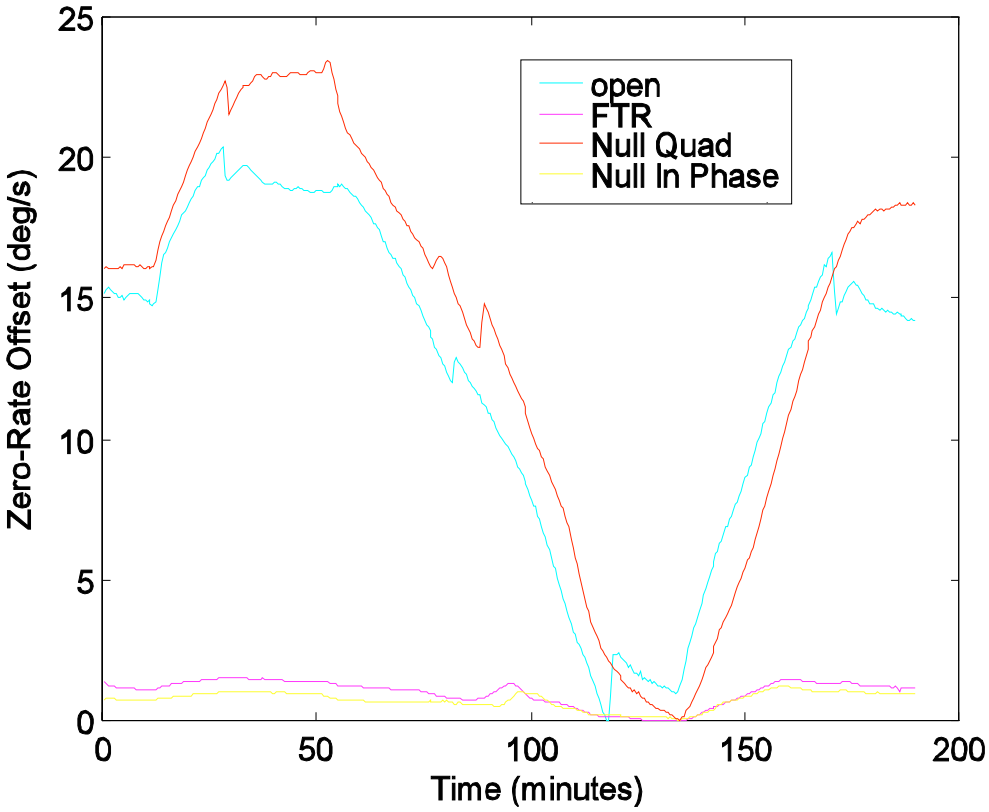

Figure 5.21 Measured reduction of temperature induced zero-rate offset drift by FTR control (offset vs time).

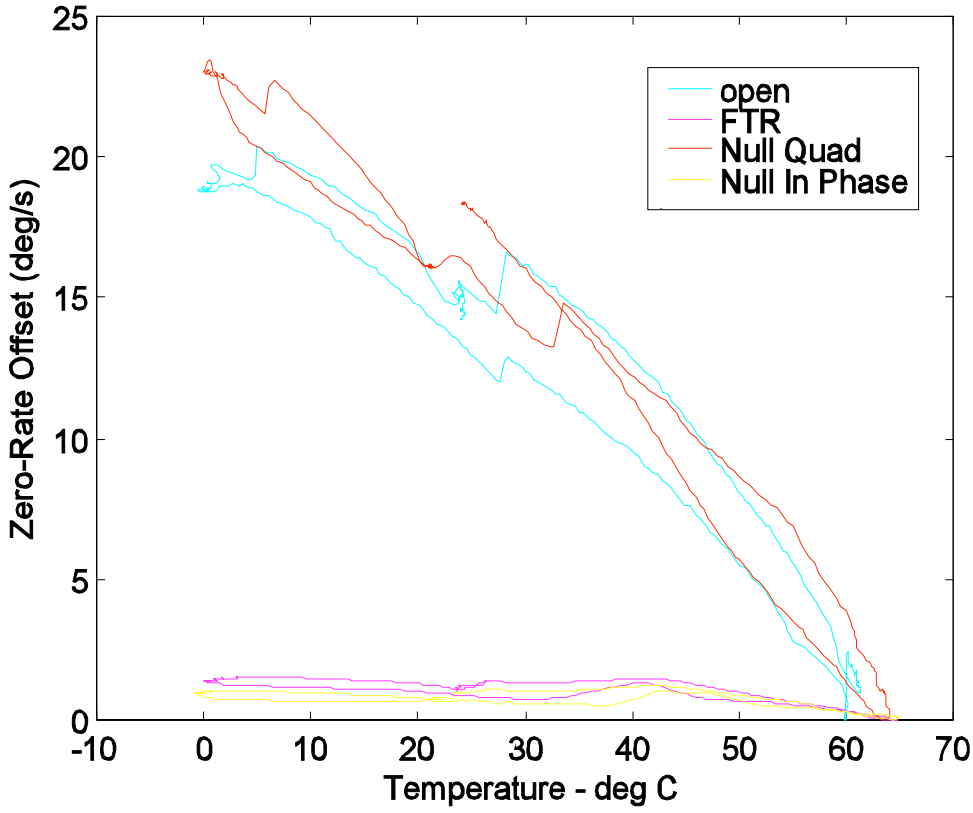

Figure 5.22 Measured reduction of temperature induced zero-rate offset drift by FTR control (offset vs temperature).

Chapter Six

Effects of Piezoelectric Material Property Variations

6.1 Introduction

Piezoelectric ceramics are commonly used to actuate and sense the vibrations of elastic bodies used as resonators in vibratory gyroscopes. It is well known that the properties of these materials vary with time and temperature. The effects of mechanical property variations (mass, stiffness and damping), of the resonator and attached piezoceramic elements, were analyzed in chapter 5. Piezoelectric and electrical property variations are considered in this chapter.

The piezoelectric gyroscope designer has to choose among the available materials from a number of different manufactures or develop a new composition which has suitable properties. The selection or specification of a material requires an understanding of which material properties influence the performance of the gyroscope. A second related decision is whether voltage of charge amplifiers should be used to measure the sensed signals. The objective of this chapter is to illustrate how the material properties effect the performance of the gyroscope and thus to present a measure which can be used either to select between available materials or to optimize the composition of a new ceramic. The control system design can also influence the sensitivity of the gyroscope to various material property variations. In the analysis presented, the gyroscope is assumed to be operating in the force to rebalance mode which was analyzed in chapter 5.

6.2 Analysis of Piezoelectric Gyroscope Operation

The analysis of the operation of a piezoelectric gyroscope begins with an electromechanical model of the resonator. This model is manipulated into a form which makes available the electrical signals used in the control electronics. The control system functions are then imposed on this model so that the effects of material property variations on the gyroscope performance, and not merely the resonator dynamics, can be established.

6.2.1 Piezoelectric Resonator Dynamics

The dynamics of a piezoelectric vibratory gyroscope resonator may be expressed by the following system of coupled electromechanical equations:

$$\begin{aligned} \boldsymbol{M}\ddot{\boldsymbol{r}}+[\boldsymbol{C}+\boldsymbol{G}(\Omega)]\dot{\boldsymbol{r}}+\boldsymbol{K}\boldsymbol{r}-\boldsymbol{\Theta}\mathbf{v} &= \boldsymbol{B}_f\boldsymbol{f} \\ \boldsymbol{\Theta}^T\boldsymbol{r}+\boldsymbol{C}_p\mathbf{v} &= \boldsymbol{B}_q\boldsymbol{q} \end{aligned} \tag{6.1}$$

These equations may be derived, for a particular resonator, by the Rayleigh-Ritz method (as was done in chapter 2) or by application of a general finite element analysis.

If we partition the electrical and electromechanical matrices to separate the elements used for sensing and actuation these equations may be written as follows:

$$\begin{aligned} \boldsymbol{M}\ddot{\boldsymbol{r}}+[\boldsymbol{C}+\boldsymbol{G}(\Omega)]\dot{\boldsymbol{r}}+\boldsymbol{K}\boldsymbol{r}-[\boldsymbol{\Theta}_s \vdots \boldsymbol{\Theta}_d]\begin{Bmatrix}\mathbf{v}_s\\ \mathbf{v}_d\end{Bmatrix} &= \boldsymbol{B}_f\boldsymbol{f} \\ [\boldsymbol{\Theta}_s \vdots \boldsymbol{\Theta}_d]^T\boldsymbol{r}+\begin{bmatrix}\boldsymbol{C}_{p_s} & \\ & \boldsymbol{C}_{p_d}\end{bmatrix}\begin{Bmatrix}\mathbf{v}_s\\ \mathbf{v}_d\end{Bmatrix} &= \boldsymbol{B}_q\begin{Bmatrix}\boldsymbol{q}_s\\ \boldsymbol{q}_d\end{Bmatrix} \end{aligned} \tag{6.2}$$

where $\mathbf{v}_s$ is the vector of sensed voltages and $\mathbf{v}_d$ is the vector of actuation or drive voltages.

If we sense with a high impedance so that the charges $\boldsymbol{q}_s$ are effectively zero the sensed voltages are given by:

$$\mathbf{v}_s = -\boldsymbol{C}_{P_S}^{-1}\boldsymbol{\theta}_s^T\boldsymbol{r} \tag{6.3}$$

As no external mechanical forces are applied to the resonator the forces $\boldsymbol{f}=\mathbf{0}$ and the above expression may be substituted into the equation of motion to yield:

$$\boldsymbol{M}\ddot{\boldsymbol{r}}+[\boldsymbol{C}+\boldsymbol{G}(\Omega)]\dot{\boldsymbol{r}}+[\boldsymbol{K}+\boldsymbol{\Theta}_s\boldsymbol{C}_{p_s}^{-1}\boldsymbol{\Theta}_s^T]\boldsymbol{r}=\boldsymbol{\Theta}_d\mathbf{v}_d \tag{6.4}$$

Generally in vibratory gyroscopes only two vibration modes are used. The mode shape vectors describing these two modes are denoted ψ_1 and ψ_2 . The mode shapes are found by an eigensolution of the problem $\boldsymbol{M}\ddot{\boldsymbol{r}}+[\boldsymbol{K}+\boldsymbol{\Theta}_s\boldsymbol{C}_{p_s}{}^{-1}\boldsymbol{\Theta}_s^T]\boldsymbol{r}=\boldsymbol{0}$ and can be used to decouple the equations of motion and reduce the problem to two generalised coordinates.

$$\boldsymbol{\Psi}^T\boldsymbol{M}\boldsymbol{\Psi}\ddot{\boldsymbol{x}}+\boldsymbol{\Psi}^T[\boldsymbol{C}+\boldsymbol{G}(\Omega)]\boldsymbol{\Psi}\dot{\boldsymbol{x}}+\boldsymbol{\Psi}^T[\boldsymbol{K}+\boldsymbol{\Theta}_s\boldsymbol{C}_{p_s}{}^{-1}\boldsymbol{\Theta}_s^T]\boldsymbol{\Psi}\boldsymbol{x}=\boldsymbol{\Psi}^T\boldsymbol{\Theta}_d\mathbf{v}_d \qquad \textbf{(6.5)}$$

where, $\boldsymbol{\Psi}=\left[\psi_1\psi_2\right]$ is the matrix containing the two operational mode shapes.

The transformation decouples the mass matrix so that $\boldsymbol{\Psi}^T\boldsymbol{M}\boldsymbol{\Psi}=\boldsymbol{m}=\begin{bmatrix} m_1 & 0 \\ 0 & m_2 \end{bmatrix}$.

In chapter 5 it was shown that damping imperfections have a greater influence than elastic imperfections, when operating in the force to rebalance mode. If we consider a resonator which is perfect except for the possibility of damping asymmetry the equations may be reduced to:

$$\ddot{\boldsymbol{x}}+[\boldsymbol{c}+\boldsymbol{g}(\Omega)]\dot{\boldsymbol{x}}+\omega_n^2\boldsymbol{x}=\boldsymbol{m}^{-1}\boldsymbol{\Psi}^T\boldsymbol{\Theta}_d\mathbf{v}_d \qquad \textbf{(6.6)}$$

where,

$\boldsymbol{c}=\boldsymbol{m}^{-1}\boldsymbol{\Psi}^T\boldsymbol{C}\boldsymbol{\Psi}$ is the reduced damping matrix which is symmetric but not necessarily diagonal.

$\boldsymbol{g}(\Omega)=\boldsymbol{m}^{-1}\boldsymbol{\Psi}^T\boldsymbol{G}(\Omega)\boldsymbol{\Psi}$ is the reduced gyroscopic matrix which is skew-symmetric.

$\omega_n^2=\boldsymbol{m}^{-1}\boldsymbol{\Psi}^T[\boldsymbol{K}+\boldsymbol{\Theta}_s\boldsymbol{C}_{p_s}{}^{-1}\boldsymbol{\Theta}_s^T]\boldsymbol{\Psi}$ is a diagonal matrix containing the two natural frequencies squared.

We can partition the electrical terms into actuation and sensing ceramics operating on the primary and secondary modes as follows:

$$\mathbf{v} = \begin{bmatrix} v_{d1} \\ v_{s1} \\ v_{d2} \\ v_{s2} \end{bmatrix} \qquad \boldsymbol{q} = \begin{bmatrix} q_{d1} \\ q_{s1} \\ q_{d2} \\ q_{s2} \end{bmatrix} \qquad \boldsymbol{\Theta} = \begin{bmatrix} \theta_{d1} \theta_{s1} \theta_{d2} \theta_{s2} \end{bmatrix} \qquad \boldsymbol{C_p} = \begin{bmatrix} C_{P_{d1}} & & & \\ & C_{P_{s1}} & & \\ & & C_{P_{d2}} & \\ & & & C_{P_{s2}} \end{bmatrix} \quad \textbf{(6.7)}$$

If we assume that the ceramics drive or sense only the primary or the secondary mode then the actuator equations can be written as follows for the two modes:

$$\begin{aligned} \ddot{x}_1 + c_{11}\dot{x}_1 + c_{12}\dot{x}_2 - g(\Omega)\dot{x}_2 + \omega_{n1}^2 x_1 &= m_1^{-1} \psi_1^T \Theta_{d1} v_{d1} \\ \ddot{x}_2 + c_{21}\dot{x}_1 + c_{22}\dot{x}_2 + g(\Omega)\dot{x}_1 + \omega_{n2}^2 x_2 &= m_2^{-1} \psi_2^T \Theta_{d2} v_{d2} \end{aligned} \quad \textbf{(6.8)}$$

The sensor equations are written for the sensing ceramics:

$$\begin{aligned} \theta_{s1}^T \psi_1 x_1 + C_{P_{s1}} v_{s1} &= 0 \\ \theta_{s2}^T \psi_2 x_2 + C_{P_{s2}} v_{s2} &= 0 \end{aligned} \quad \textbf{(6.9)}$$

These equations may be rearranged so that the sensed voltages measuring the primary and secondary vibration modes may be written explicitly.

$$\begin{aligned} v_{s1} &= -C_{P_{s1}}^{-1} \theta_{s1}^T \psi_1 x_1 \\ v_{s2} &= -C_{P_{s2}}^{-1} \theta_{s2}^T \psi_2 x_2 \end{aligned} \quad \textbf{(6.10)}$$

The assumption that the sensors and actuators only sense and actuate either the primary or secondary modes of vibration may be expressed mathematically as $\Theta_{s_1}{}^T \psi_2 = 0; \quad \Theta_{s_2}{}^T \psi_1 = 0; \quad \psi_1^T \Theta_{d_2} = 0; \quad \psi_2^T \Theta_{d_1} = 0$. This assumption is only valid in the limited case of a resonator with no errors in sensor and actuator location.

6.2.2 Control System Functions

The control functions used in force to rebalance operation may be simply described

as driving the primary mode at it's resonant frequency to a specified amplitude and nulling any response in the secondary mode. Therefore the frequency and amplitude of v_{d1} (voltage applied to drive the primary mode) is continuously adjusted to give v_{s1} (voltage sensed due to primary mode displacement) to be 90° out of phase and at a prescribed amplitude $\overline{v_{s1}}$. Because the piezoelectric properties of the sensing ceramics can change, with temperature and time, the amplitude of vibration which results in a sensed voltage $\overline{v_{s1}}$ can change. The amplitude of vibration is found from the sensing equation for the primary mode:

$$x_1 = -[C_{p_{s_1}^{-1}} \Theta_{s_1}{}^T \psi_1]^{-1} \overline{v_{s_1}} \qquad \textbf{(6.11)}$$

This equation shows that variations in the capacitance or electromechanical coupling of the sensing piezoceramics will cause variations in the amplitude of mechanical vibration.

The motion in the secondary mode, measured by v_{s2} , is suppressed by applying v_{d2} so that v_{s2} is nulled. The sensor equation for the secondary mode indicates that x_2 must be zero if v_{s2} is nulled. If x_2 is forced to zero then $\dot{x}_2$ and $\ddot{x}_2$ will also be zero and the equation of motion for the secondary mode reduces to,

$$c_{21}\dot{x}_1 + g(\Omega)\dot{x}_1 = m_2^{-1}\psi_2^T\theta_{d2}v_{d2} \qquad \textbf{(6.12)}$$

The voltage v_{d2} applied to null the motion of the secondary mode provides a measure of the inertial angular rate which is the information required from the gyroscope.

$$v_{d2} = m_2^{-1}(\psi_2^T\theta_{d2})^{-1}(c_{21}\dot{x}_1 + g(\Omega)\dot{x}_1) \qquad \textbf{(6.13)}$$

At steady state $\dot{x}_1 = -j\omega[C_{p_{s_1}}{}^{-1}\Theta_{s_1}{}^T\psi_1]^{-1}\overline{v_{s_1}}$ therefore,

$$v_{d_2} = -j\omega m_2 \frac{C_{p_{s_1}}}{\psi_2^T \Theta_{d_2}{}^{-1} \Theta_{s_1}{}^T \psi_1} \overline{v}_{s_1} (c_{21} + g(\Omega)) \qquad \textbf{(6.14)}$$

This equation expresses the zero-rate drift and also the scale factor or sensitivity to rotation rate of the gyroscope.

6.3 Piezoelectric Property Variations

At zero rotation rate there will be a voltage required to null the motion of the secondary mode due to the damping asymmetry represented by c_{21} . The stability of this zero rate offset, over time and temperature, is of great importance in many gyroscope applications. It is therefore of interest to determine how the material properties of the piezoceramic material influence this offset. In the formulation used, the capacitance matrices are linearly dependent on the material parameter ε_{33}^S while the piezoelectric coupling matrices are linearly dependent on the material parameter e_{31} . Therefore the offset is a function of $\varepsilon_{33}^S / e_{31}^2$ and it is desirable that this quantity should be as stable as possible.

The scale factor of a gyroscope relates the voltage output (proportional to v_{d2}) to the applied rotation rate. The stability of the scale factor of the gyroscope, over time and temperature, is another important performance parameter of the gyroscope. The scale factor is a function of $\varepsilon_{33}^S / e_{31}^2$ therefore it is important that this quantity remains as constant as possible over time and temperature.

The influence of the ratio $\varepsilon_{33}^S / e_{31}^2$ on zero-rate offset and scale factor make this quantity a suitable figure-of-merit that should be used to select a piezoceramic material for operation over temperature and time.

In this analysis it was assumed that in practice, the displacements of the resonator would be determined by measuring the voltages at the sensing ceramics with a high impedance circuit. A second possibility is that a charge amplifier (low impedance) is used and the measured charge is proportional to the displacements. Repeating the above analysis for this situation shows that the zero-rate offset and the scale factor are then

dependent on the ratio $1/e_{31}^2$. Therefore in this situation the figure of merit for the selection or optimization of piezoelectric materials would be $1/e_{31}^2$.

6.4 Conclusions

The effects of piezoelectric and electrical property variations of the piezoceramic material used in vibratory gyroscopes was analyzed. Force to rebalance control was assumed and damping imperfections were included in the analysis. It was shown that when high impedance sensing electronics (buffer or voltage follower) is used, the zero-rate offset and the scale factor of the piezoelectric vibratory gyroscope vary according to the ratio $\varepsilon_{33}^S/e_{31}^2$. When low impedance (charge amplifier) electronics is used the ratio $1/e_{31}^2$ describes the variation of zero-rate offset and scale factor. These two figures of merit should be evaluated when deciding on which form of electronic amplification to use and also when selecting an existing piezoceramic material or optimizing a new composition.

Chapter Seven

Conclusions and Recommendations

The effects of imperfections in vibratory gyroscopes has been studied with particular emphasis on piezoelectrically actuated and sensed resonators. The study began with considering the resonator dynamics and the effects of control on the resonator dynamics. The more general problem of the effects of imperfections in the controlled system was then analyzed. Conclusions for each part of the study are given in the individual chapters therefore only the conclusions that relate specifically to the objectives of the study are repeated here.

Piezoelectric resonators used in vibratory gyroscopes may be effectively modeled using Hamilton's principle for the electromechanical system and the Rayleigh-Ritz method. A cylindrical resonator, including imperfections, was modeled and the results agreed well with experiment. This approach also made it possible to analyze the effects of the control system on the resonator dynamics and the effects of piezoelectric material property variations in general terms. The findings of this study were published in the Journal of Intelligent Material Systems and Structures [32]. This was the first publication which included imperfections in piezoelectric vibratory gyroscopes and which presented direct comparison between theoretical and experimental results.

The effect of elastic boundaries on the dynamics of thin-walled rotating cylinders was analyzed by an exact solution of the Flügge shell theory equations of motion. It was found that the natural frequency, of the operating mode of a cylinder supported at one end only, is very sensitive to the axial stiffness of the support. A range of boundary stiffnesses in which the natural frequency and sensitivity to rotation (gyroscope scale factor) are sensitive to boundary stiffness variations was determined. It is recommended that cylinders be designed to have boundary stiffnesses outside this range as they will then be practically insensitive to boundary stiffness variations. Only axisymmetric boundaries were considered. This research was published as a general study of elastically supported

thin cylindrical shell vibrations, in the Journal of Sound and Vibration [40]. Future work on cylindrical resonator modeling could focus on the effects of non-axisymmetric boundary conditions. The effects of slight ovaling of a cylinder could also be analyzed.

The effects of displacement and velocity feedback on the resonator dynamics was analyzed. The method used is general but requires an electromechanical model of the resonator. Experimental results confirmed the accuracy of the method. It was shown that 'electrical springs' and 'electrical dampers' may be formed by displacement and velocity feedback respectively. In the case of the cylinder vibratory gyroscope it was found that the effect of displacement feedback was more than adequate to balance the effects of typical manufacturing imperfections. A simple experimental method of determining the effect of displacement feedback on the natural frequency was devised and verified. This research contribution was published in the IEEE Transactions on Ultrasonics, Ferroelectrics and Frequency Control [48].

The ability of the electronic control system to reduce the effects of resonator imperfections was investigated. Averaged equations of motion derived from a general model of a resonator were used to motivate the control system functions. This approach has the advantage that only slowly varying components need be simulated numerically or controlled electronically in practice. Excitation by a phase-locked loop was used to ensure vibration at resonance of the primary mode. Control of the secondary mode is usually motivated by a desire to increase the bandwidth of the gyroscope. Two control schemes, acting on the secondary mode, were considered and it was shown that these schemes reduce the effects of mass/stiffness imperfections leaving damping anisotropy as the major source of error. The reduction of the effects of mass/stiffness imperfections is therefore a major advantage of closed loop operation. This result is applicable to a wide range of vibratory gyroscopes including micromachined designs. Experimental results showed that both damping loop control and force to rebalance control reduced the zero-rate offset variation over temperature by an order of magnitude. The major contribution to knowledge of vibratory gyroscope control systems, was the explanation and demonstration of the ability of the control system to reduce the effects of elastic imperfections. This contribution will be published as a journal paper. Simple

implementation of the electronic control system needs to be investigated as does design for low noise.

Stability of the closed loop systems could be analyzed in future and nonlinearities in the resonator could be included requiring a higher order approximation in the method of averaging.

“Electrical springs”, formed by displacement feedback, could be used to reduce the effects of mass/stiffness imperfections in the same way as has been done with “electrical springs”, formed by electrostatic forces in the HRG. This approach would require the construction of resonators with 16 piezoceramic elements but would not offer any advantage over force to rebalance control.

The effect of piezoelectric material property variations were studied for a piezoelectric resonator operating in force to rebalance mode. The effects of variations in the piezoelectric and dielectric coefficients on the zero-rate offset and the scale factor were determined. Two simple figures-of-merit were proposed for resonators in which voltage or charge amplifiers are connected to the sensing elements. These figures of merit should be used when selecting an existing piezoceramic material or when optimizing a new composition for this application. The development of a simple, direct method of measuring these figures-of-merit would be a useful contribution. The magnitude of the damping imperfection introduced by different piezoceramic compositions needs to be quantified in future and included in the material selection process. Analysis of other types of sensing and actuation could be performed and the various methods compared to determine which is most appropriate method of sensing and actuation for particular resonator designs.

References

1. Matthews, A., and F.J. Rybak, "Comparison of hemispherical resonator gyro and optical gyros", *IEEE AES Magazine,* May 1992, pp.40-46.

2. Synge, J. L., and B. A. Griffith, *Principles of Mechanics,* 3rd edition, McGraw-Hill Book Company, Inc., New York 1959, pp.365.

3. Quick, W. H., "Theory of the vibrating string as an angular motion sensor", *Trans. ASME, J. Appl. Mech.*, Sept. 1964, pp. 523-534.

4. Fujishima, S., T. Nakamura and K. Fujimoto, "Piezoelectric vibratory gyroscope using flexural vibration of a triangular bar", *Forty-Fifth Annual Symposium on Frequency Control*, 1991, pp. 261-265.

5. Abe, H., T. Yoshida and K. Turuga, "Piezoelectric-Ceramic Cylinder Vibratory Gyroscope", *Jpn. J. Appl. Phy.*, Vol. 31(1), 1992, pp.3061-3063.

6. Hunt, G. H., and A. E. W. Hobbs, "Development of an accurate tuning-fork gyroscope", *Symposium on Gyros, Proc. Inst. Mech. Eng. (London)*, 1964-1965,Vol. 179(3E), pp.129-139.

7. Söderkvist, J., "Piezoelectric beams and vibrating angular rate sensors", *IEEE Trans. on Ultrasonics, Ferroelectrics, and Frequency Control*, Vol. 38(3), 1991, pp.271-280.

8. G. H. Bryan, "On the beats in the vibrations of a revolving cylinder or bell", *Proceedings of the Cambridge Philosophical Society, Vol. 7*, 1890, pp.101-111.

9. Emslie, A. G., UK Patent 1 288 118, 6 Sept. 1972.

10. Denis, R. E., UK Patent 1 288 449, 6 Sept. 1972.

11. Loper, E. J., and D. D. Lynch, US Patent 4 157 041, 5 June, 1979.

12. Loper, E. J., and D. D. Lynch, US Patent 4 951 508, 28 August 1990.

13. Lynch, D. D., and A. Matthews, “Dual-mode hemispherical resonator gyro operating characteristics, *Proc. 3rd St. Petersburg International Conference on Gyroscopic Technology and Navigation*, St. Petersburg, Russia, 1996, pp. 37-44.

14. Loper, E.J., and D.D. Lynch, "Projected system performance based on recent HRG test results", *Proc. IEEE/AIAA 5th Digital Avionics System Conference*, Seattle, October 1983, pp.18.1.1-18.1.6.

15. Putty, M. W., and K. Najafi, "A micromachined vibrating ring gyroscope", *Solid-State Sensor and Actuator Workshop*, Hilton Head, South Carolina, 1994, pp. 213-220.

16. Langdon, R. M., "The vibrating cylinder gyroscope", *The Marconi Review*, Fourth Quarter, 1982, pp. 231-249.

17. Reppich, A., and R. Willig, “Yaw rate sensor for vehicle dynamics control system”, *DGON Symposium Gyro Technology*, Stuttgart, 1995.

18. Burdess, J. S., "The dynamics of a thin piezoelectric cylinder gyroscope", *Proc. Inst. Mech. Engrs. (London)*, Vol. 200(C4), 1986, pp.271-280.

19. Langmaid, C., "Vibrating structure gyroscopes", *Sensor Review*, Vol. 16(1), 1996, pp. 14-17.

20. Yazdi, N., F. Ayazi and K. Najafi, "Micromachined inertial sensors", *Proceedings of the IEEE*, Vol. 86(8), 1998, pp. 1640-1659.

21. Zarabadi, S. R., P. E. Castillo-Borelly and J. D. Johnson, "An angular rate sensor interface IC", *IEEE 1996 Custom Integrated Circuits Conference*, pp. 311-314.

22. Lutz, M., W. Golderer, J. Gerstenmeier, J. Marek, B. Maihofer, S. Mahler, H. Munzel and U. Bischof, "A precision yaw rate sensor in silicon micromachining", in Tech. Dig. 9th Int. Conf. Solid-State Sensors and Actuators (Transducers '97), Chicago, IL, June 1997, pp. 847-850.

23. Tanaka, K., Y. Mochida, M. Sugimoto, K. Moriya, T. Hasegawa, K. Atsuchi and K. Ohwada, "A micromachined vibrating gyroscope", *Sensors and Actuators A*, Vol. 50, 1995, pp. 111-115.

24. Weinberg, M., J. Bernstein, S. Cho, A. T. King, A. Kourepenis, P. Ward and J. Sohn, "A micromachined comb drive tuning fork gyroscope for commercial applications", *2nd St. Petersburg International Conference on Gyroscopic Technology & Navigation*, St. Petersburg, Russia, 24-25 May 1995.

25. Ljung, P. B., "Micromachined two input axis angular rate sensor", *ASME Dynamic Systems and Control Division*, San Francisco, CA, November 1995, pp. 957-962.

26. Juneau, T., and A. P. Pisano, Micromachined dual input axis angular rate sensor", *Solid-State Sensor and Actuator Workshop*, Hilton Head, SC, June 1996.

27. Shatalov, M., J. du Pre le Roux and F. Koch, “Estimation of vibratory gyroscope parameters with data derived from the vibrating element”, *DGON Symposium Gyro Technology*, Stuttgart, 1996.

28. Friedland, B., and M. F. Hutton. 1978. “Theory and error analysis of vibrating-member gyroscope”, *IEEE Trans. Automatic Control*, Vol. AC-23, No. 4, pp.545-556.

29. Fox, C. H. J., "Vibrating cylinder rate gyro: theory of operation and error analysis", *DGON Symposium Gyro Technology*, Stuttgart, 1988.

30. Fox, C. H. J., "Analysis and control of imperfection effects in vibratory gyros", *DGON Symposium Gyro Technology*, Stuttgart. 1994.

31. Shatalov, M. Y., and P. W. Loveday, “A theory of errors in vibratory gyroscopes”, *DGON Symposium Gyro Technology*, Stuttgart, 1995.

32. Loveday, P. W., “A coupled electromechanical model of an imperfect piezoelectric vibrating cylinder gyroscope”, *Journal of Intelligent Material Systems and Structures*, Vol. 7(1), 1996, pp. 44-53.

33. Hagood, N. W., W. Chung and A. von Flotow, "Modeling of piezoelectric actuator dynamics for active structural control", *Journal of Intelligent Material Systems and Structures*, Vol. 1(3), 1990, pp.327-354.

34. Hagood, N. W., and E. H. Anderson, "Simultaneous sensing and actuation using piezoelectric materials", *SPIE Vol. 1543 Active and Adaptive Optical Components*, 1991, pp. 409-421.

35. Leissa, A.W., *Vibration of Shells*, NASA SP-288, 1973.

36. Warburton, G. B., *The Dynamical Behaviour of Structures*, Pergamon Press Ltd., Second Edition, 1976.

37. Bishop, R. E. D., and D. C. Johnson, *The Mechanics of Vibration*, Cambridge University Press, 1960.

38. van Randeraat, J., and R. E. Setterington. *Piezoelectric Ceramics*, Mullard Ltd., Second Edition, 1974.

39. Stiles, J. C., "Vibrating ring gyro", U.S. Patent 3,926,475, 1975.

40. Loveday P. W., and C. A. Rogers, "Free vibration of elastically supported thin cylinders including gyroscopic effects", *Journal of Sound and Vibration*, Vol. 217(3), 1998, pp. 547-562.

41. Blevins, R. D., *Formulas for Natural Frequency and Mode Shape*, Van Nostrand Reinhold, New York, 1979.

42. Aremenàkas, A. E., D. Gazis and G. Herrmann, *Free Vibrations of Circular Cylindrical Shells*, Pergamon Press, Oxford, 1969.

43. Forsberg, K., "Influence of boundary conditions on modal characteristics of cylindrical shells", *American Institute of Aeronautics and Astronautics Journal*, Vol. 2, 1964, pp.182-189.

44. Warburton, G. B., "Vibration of thin cylindrical shells", *Institution of Mechanical Engineers Journal of Mechanical Engineering Science*, Vol. 7(4),1965, pp.399-407.

45. Warburton, G. B., and J. Higgs, “Natural frequencies of thin cantilever cylindrical shells”, *Journal of Sound and Vibration,* Vol. 11(3), 1970, pp.335-338.

46. Vronay, D. F., and B. L. Smith, “Free vibration of circular cylindrical shell of finite length”, *American Institute of Aeronautics and Astronautics Journal,* Vol. 8(3), 1970, pp.601-603.

47. Egarmin, N.E., "Precession of vibrational standing waves of a rotating axisymmetric shell", *Izv. AN SSSR. Mekhanika Tverdogo Tela*, Vol. 21(1), 1986, pp.142-148.

48. Loveday P. W., and C. A. Rogers, “Modification of piezoelectric vibratory gyroscope resonator parameters by feedback control”, *IEEE Transactions on Ultrasonics, Ferroelectrics and Frequency Control*, Vol. 45(5), 1998, pp.1211-1215.

49. Putty, M. W., “*A micromachined vibrating ring gyroscope*”, PhD Dissertation, University of Michigan, 1995.

50. Tzou, H. S., “ *Piezoelectric Shells - Distributed Sensing and Control of Continua*”, Kluwer Academic Publishers, 1993.

51. Alghamdi, A. A., and A. Dasgupta, “Experimental and analytical study of adaptive structures using eigenstrain techniques”, *SPIE* , Vol. 2442, 1995, pp. 122-132.

52. Newland, D. E., “*Mechanical Vibration Analysis and Computation*”, Longman Scientific & Technical, 1989.

53. Lynch, D. D., “Vibratory gyro analysis by the method of averaging”, *Proc. 2nd St. Petersburg International Conference on Gyroscopic Technology and Navigation*, St. Petersburg, Russia, 1995, pp. 26-34.

54. Nayfeh, A. H., *Introduction to Perturbation Techniques*, John Wiley & Sons, Inc., 1981.

APPENDIX A: Derivation of Matrix Terms Used in Resonator Modeling

A.1 Mass Matrix and Gyroscopic Matrix

Simulation of the rotating vibrating cylinder requires that we derive the gyroscopic matrix. Both the mass matrix and the gyroscopic matrix are derived from the kinetic energy so both can be derived simultaneously.

The velocity of a point on the mid surface of a cylinder which is rotating at angular rotation rate Ω about its axis is:

$$Vel = \begin{Bmatrix} \dot{u} \\ \dot{v} - \Omega(a+w) \\ \dot{w} + \Omega v \end{Bmatrix} \tag{A.1}$$

The kinetic energy of the cylinder is found by integrating over the volume of the cylinder,

$$\begin{aligned} T = \frac{1}{2}\rho\int_V [&\dot{u}^2 + \dot{v}^2 + \dot{w}^2 - 2\Omega\dot{v}(a+w) + 2\Omega\dot{w}v \\ &+ \Omega^2(a^2 + 2aw + w^2) + v^2\Omega^2]\,dV \end{aligned} \tag{A.2}$$

The kinetic energy of the piezoceramics has the same form with the integration being performed over the volume of the piezoceramics. If we consider slowly rotating cylinders, we can omit the terms of order Ω^2. Substitution of the assumed displacement distributions (equation 2.15) yields,

$$\begin{aligned} T = \frac{1}{2}\rho\int_V [&\dot{U}_1^2 H(x)^2\cos^2(2\theta) + \dot{U}_2^2 H(x)^2\sin^2(2\theta) + 2\dot{U}_1\dot{U}_2 H(x)^2\cos(2\theta)\sin(2\theta) \\ &+ \dot{V}_1^2 F(x)^2\sin^2(2\theta) + \dot{V}_2^2 F(x)^2\cos^2(2\theta) + 2\dot{V}_1\dot{V}_2 F(x)^2\cos(2\theta)\sin(2\theta) \\ &+ \dot{W}_1^2 F(x)^2\cos^2(2\theta) + \dot{W}_2^2 F(x)^2\sin^2(2\theta) + 2\dot{W}_1\dot{W}_2 F(x)^2\cos(2\theta)\sin(2\theta) \\ &+ 2\Omega(\dot{V}_1 F(x)\,a\sin(2\theta) + \dot{V}_1 W_1 F(x)^2\cos(2\theta)\sin(2\theta) + \dot{V}_1 W_1 F(x)^2\sin^2(2\theta) \\ &+ \dot{V}_2 F(x)\,a\cos(2\theta) + \dot{V}_2 W_1 F(x)^2\cos^2(2\theta) + \dot{V}_2 W_2 F(x)^2\cos(2\theta)\sin(2\theta)) \\ &+ 2\Omega(\dot{W}_1\dot{V}_1 F(x)^2\cos(2\theta)\sin(2\theta) + \dot{W}_1 V_2 F(x)^2\cos^2(2\theta) \\ &+ \dot{W}_2 V_1 F(x)^2\sin^2(2\theta) + \dot{W}_2 V_2 F(x)^2\cos(2\theta)\sin(2\theta))]\,dV \end{aligned} \tag{A.3}$$

After taking variations, integrating by parts and collecting terms in the first and second derivative of the generalized coordinates the following mass and gyroscopic matrices are found:

$$\boldsymbol{M}_s = \rho \int_V \begin{bmatrix} H(x)^2\cos^2(2\theta) & 0 & 0 & H(x)^2\cos(2\theta)\sin(2\theta) & 0 & 0 \\ 0 & F(x)^2\sin^2(2\theta) & 0 & 0 & F(x)^2\cos(2\theta)\sin(2\theta) & 0 \\ 0 & 0 & F(x)^2\cos^2(2\theta) & 0 & 0 & F(x)^2\cos(2\theta)\sin(2\theta)0 \\ H(x)^2\cos(2\theta)\sin(2\theta) & 0 & 0 & H(x)^2\sin^2(2\theta) & 0 & 0 \\ 0 & F(x)^2\cos(2\theta)\sin(2\theta) & 0 & 0 & F(x)^2\cos^2(2\theta) & 0 \\ 0 & 0 & F(x)^2\cos(2\theta)\sin(2\theta) & 0 & 0 & F(x)^2\sin^2(2\theta) \end{bmatrix} dV \qquad (A.4)$$

$$\boldsymbol{G}_s = \rho\Omega \int_V \begin{bmatrix} 0 & 0 & 0 & 0 & 0 & 0 \\ 0 & 0 & -2F(x)^2\cos(2\theta)\sin(2\theta) & 0 & 0 & -2F(x)^2\sin^2(2\theta) \\ 0 & 2F(x)^2\cos(2\theta)\sin(2\theta) & 0 & 0 & F(x)^2\cos^2(2\theta) & 0 \\ 0 & 0 & 0 & 0 & 0 & 0 \\ 0 & 0 & -2F(x)^2\cos^2(2\theta) & 0 & 0 & -2F(x)^2\cos(2\theta)\sin(2\theta) \\ 0 & 2F(x)^2\sin^2(2\theta) & 0 & 0 & F(x)^2\cos(2\theta)\sin(2\theta) & 0 \end{bmatrix} dV \qquad (A.5)$$

Note that the mass matrix derived here is the same as is obtained by substituting the assumed displacement distributions into equation 2.8.

A.2 Stiffness Matrix

The derivation of the stiffness matrix is rather lengthy. To illustrate the derivation of this matrix only one of the terms in the piezoceramic stiffness matrix for the first assumed mode (K_{P1}) is derived here.

The assumed displacement distributions for the first mode may be written in the form of equation 2.4a.

$$\begin{aligned}\boldsymbol{u}(x,\theta,t) &= \boldsymbol{\psi}_{\boldsymbol{r}_1}(x,\theta)\boldsymbol{r}_1(t) \\ &= \begin{bmatrix} H(x)\cos(2\theta) & & \\ & F(x)\sin(2\theta) & \\ & & F(x)\cos(2\theta) \end{bmatrix} \begin{bmatrix} U_1 \\ V_1 \\ W_1 \end{bmatrix}\end{aligned} \tag{A.6}$$

The matrix $\boldsymbol{N}_{\boldsymbol{r}}(x)$, in equation 2.6, for this mode is:

$$\boldsymbol{N}_{\boldsymbol{r}_1}(x,\theta) = \begin{bmatrix} \frac{\partial H(x)}{\partial x}\cos(2\theta) & 0 & -z\,\frac{\partial^2 F}{\partial^2 x}\cos(2\theta) \\ 0 & 2(\frac{1}{a}+\frac{z}{a^2})F(x)\cos(2\theta) & (\frac{1}{a}+4\frac{z}{a^2})F(x)\cos(2\theta) \\ 0 & 0 & 0 \\ 0 & 0 & 0 \\ 0 & 0 & 0 \\ -\frac{2}{a}H(x)\sin(2\theta) & (1+2\frac{z}{a})\frac{\partial F(x)}{\partial x}\sin(2\theta) & 4\frac{z}{a}\frac{\partial F(x)}{\partial x}\sin(2\theta) \end{bmatrix} \tag{A.8}$$

The piezoceramic elements used in this application were polarized in the radial direction so the rotation matrix in equation 2.9 may be omitted and the expression for the piezoceramic stiffness matrix for the first assumed mode simplifies to:

$$\boldsymbol{K}_{\boldsymbol{P}_1} = \int_{V_P} \boldsymbol{N}_{\boldsymbol{r}_1}{}^{\boldsymbol{T}}\boldsymbol{c}^{\boldsymbol{E}}\boldsymbol{N}_{\boldsymbol{r}_1} dV \tag{A.9}$$

The first element in this matrix is:

$$K_{P_1}(1,1) = \int_{V_P} c_{11}(\frac{\partial H(x)}{\partial x})^2\cos^2(2\theta) + c_{66}\frac{4}{a^2}H(x)^2\sin^2(2\theta)\; dV \tag{A.10}$$

where the integration is performed over the volume of all the ceramic elements.

APPENDIX B: Calculation of Amplitude Ratios

Equation 3.6 can be used to write the ratios of the axial and tangential displacements to the radial displacements. In the following equations the small terms containing β^2 have been neglected and ν is assumed to be 0.3.

$$\frac{U_0}{W_0} = \frac{\begin{array}{c}\alpha n\beta[0.65(\alpha^2-n^2)^2+1.405\alpha^2-0.95n^2+0.65-\Delta\frac{\Omega}{\omega}(0.7n+2\frac{\alpha^2}{n})] \\ +0.35\alpha n+0.65\alpha n\Delta+0.6\frac{\Omega}{\omega}\Delta\alpha\end{array}}{\begin{array}{c}n\beta[-0.7\alpha^4+0.7\alpha^2n^2-0.35n^2-1.35\alpha^2\Delta+0.7\frac{\Omega}{\omega}\Delta n] \\ -0.35n^3+0.805n\alpha^2+n\Delta+\frac{\Omega}{\omega}\Delta[0.7n^2-2(\alpha^2+\Delta^2)]\end{array}} \qquad \textbf{(B.1)}$$

$$\frac{V_0}{W_0} = \frac{\begin{array}{c}n\beta[0.65(\alpha^2-n^2)^2+1.405\alpha^2-0.95n^2+0.65+\Delta\frac{\Omega}{\omega}(0.7n+2\frac{\alpha^2}{n})] \\ +0.35n+0.65n\Delta-0.6\frac{\Omega}{\omega}\Delta\end{array}}{\begin{array}{c}\beta[0.35\alpha^4-0.35n^4+\alpha^2\Delta-0.35\alpha^2+0.35n^2\Delta] \\ -0.35n^2-0.105\alpha^2+1.3n\frac{\Omega}{\omega}\Delta-0.3\Delta\end{array}} \qquad \textbf{(B.2)}$$

The amplitude ratios are then calculated by substituting the roots ($\pm\alpha_1,\ \pm i\gamma_2,\ \pm(p\pm iq)$) in equations (B.1) and (B.2), for α, as follows:

$A_1 = (V_0 / W_0)$ with $\alpha = \alpha_1$

$A_2 = (U_0 / W_0)$ with $\alpha = \alpha_1$

$A_3 = (V_0 / W_0)$ with $\alpha = i\gamma_2$

$iA_4 = (U_0 / W_0)$ with $\alpha = i\gamma_2$

$A_5 + iA_6 = (V_0 / W_0)$ with $\alpha = p + iq$

$A_7 + iA_8 = (U_0 / W_0)$ with $\alpha = p + iq$

VITA

Philip Wayne Loveday was born in Napier, New Zealand on April 25, 1967. He obtained a B.Sc. in Mechanical Engineering and a M.Sc in Engineering from the University of the Witwatersrand, Johannesburg, South Africa in 1988 and 1990 respectively. The title of his masters dissertation was "Structural Dynamic Modification using Experimentally Improved Finite Element Models". He was awarded the Thomas Price Award by the South African Institute of Mechanical Engineers for a journal paper on this work. In 1991 he was employed by the CSIR, South Africa as a member of the Sensor Systems Program where he was responsible for the design and analysis of various piezoelectric sensors and actuators including piezoelectric vibratory gyroscopes. These activities lead to an interest in the field of Smart Material Systems and Structures. In August 1995, he began his Ph.D. studies at the Center for Intelligent Material Systems and Structures, at Virginia Polytechnic Institute and State University. From July 1996 to November 1998 he conducted his research at the CSIR in South Africa. He obtained a Ph.D. degree in Mechanical Engineering from Virginia Tech in 1999.